A review of nuclear batteries

Article *in* Progress in Nuclear Energy · August 2014

DOI: 10.1016/j.pnucene.2014.04.007

CITATIONS
92

READS
31,568

6 authors, including:

Mark Prelas
University of Missouri
521 PUBLICATIONS **2,206** CITATIONS
SEE PROFILE

Eric Lukosi
University of Tennessee
78 PUBLICATIONS **299** CITATIONS
SEE PROFILE

Denis Wisniewski
University of Missouri
17 PUBLICATIONS **164** CITATIONS
SEE PROFILE

A Review of Nuclear Batteries

Mark. A. Prelas[1], Charles J. Weaver[1,2], Matthew Watterman[1], Eric Lukosi[3], Robert Schott[1], and Denis Wisniewski[1]

1. Nuclear Science and Engineering Institute, University of Missouri. Columbia, MO
2. Sidney Kimmel Institute for Nuclear Renaissance, University of Missouri. Columbia, MO
3. Nuclear Engineering, University of Tennessee, Knoxville, TN

Abstract

This paper reviews recent efforts in the literature to miniaturize nuclear battery systems. The potential of a nuclear battery for longer shelf-life and higher energy density when compared with other modes of energy storage make them an attractive alternative to investigate. The performance of nuclear batteries are a function of the radioisotope(s), radiation transport properties and energy conversion transducers. The energy conversion mechanisms vary significantly between different nuclear battery types, where the radioisotope thermoelectric generator, or RTG, is typically considered a performance standard for all nuclear battery types. The energy conversion efficiency of non-thermal-type nuclear batteries requires that the two governing scale lengths of the system, the range of ionizing radiation and the size of the transducer, be well-matched. Natural mismatches between these two properties have been the limiting factor in the energy conversion efficiency of small-scale nuclear batteries. Power density is also a critical performance factor and is determined by the interface of the radioisotope to the transducer. Solid radioisotopes are typically coated on the transducer, forcing the cell power density to scale with the surface area (limiting power density). Methods which embed isotopes within the transducer allow the power density to scale with cell volume (maximizing power density). Other issues that are examined include the limitations of shelf-life due to radiation damage in the transducers and the supply of radioisotopes to sustain a commercial enterprise. This review of recent theoretical and experimental literature indicates that the physics of nuclear batteries do not currently support the objectives of miniaturization, high efficiency and high power density. Instead, the physics imply that nuclear batteries will be of moderate size and limited power density. The supply of radioisotopes is limited and cannot support large scale commercialization. Niche applications for nuclear batteries exist, and advances in materials science may enable the development of high-efficiency solid-state nuclear batteries in the near term.

1 Introduction

Nuclear batteries have attracted the interest of researchers since the early 1900's [1] and continue to do so because of one factor: the potential for a long battery lifetime. There are many competing types of nuclear batteries: thermoelectric, thermophotoelectric, direct charge collection, thermionic, scintillation intermediate, and direction energy conversion alphavoltaics and betavoltaics. For the past forty years the dominant nuclear battery technology has been the

radioisotope thermoelectric generator, or RTG, which converts the decay heat of radioisotopes into electricity through the Seebeck effect [2-4]. RTGs have been deployed in numerous deep space missions [5] and their demonstrated success makes the RTG the benchmark against which other nuclear battery technologies are measured. However, two important characteristics make them incompatible with the downscaling trend of new electrical systems; they are about 6% efficient and they are large. Their efficiency yields a large mass, or lower power density, and the mode of operation yields a large footprint, where the multi-mission RTG, with a mass of 45 kg, length of 0.66 m and diameter of 0.63 m. To adapt the advantages of nuclear battery technology for use in the ever-smaller devices which are in development, recent efforts have attempted to both miniaturize nuclear batteries and improve their total energy conversion efficiency. This has produced a variety of new miniature nuclear battery systems. Many of them use energy conversion mechanisms different from the RTG.

All nuclear battery systems share many of the same design considerations, but the additional goals of increased efficiency and smaller size introduce additional caveats to the design process. The performance of any nuclear battery technology is ultimately determined by the physics of radioisotope(s), radiation transport, and energy conversion transducers. The specific energy density (J/kg) of radioisotopes is intrinsically higher than chemical energy sources by many orders of magnitude, due to the energetics of nuclear decay, but the appropriateness of a radioisotope source for a given battery power application also depends on the specific power density (W/kg). Within a certain radioactive decay type (alpha, beta, fission, etc.) the energy density varies inversely with the half-life of the isotope; the shorter the half-life, the higher the power density. This fundamental principle causes the two properties desired of a nuclear battery, long shelf-life and high power density, to be opposed because of the fundamental properties of nuclear decay.

Another design consideration specific to miniature nuclear batteries not of the thermal type is that the scale lengths of the system are ‘well-matched’. Within the context of this paper, the range of a given particle in a specific material is referred to as the transport scale length of the radiation (λ_{RadTr}); the relevant physical dimension of the energy conversion volume in the transducer is referred to as the scale length of the transducer (L_{trans}). These two scale lengths, λ_{RadTr} and L_{trans}, should be approximately equal. This fundamental property is the primary factor that dominates the efficiency of a nuclear battery; ‘well-matched’ systems have a higher maximum theoretical efficiency, while systems which are not ‘well-matched’ have a lower maximum theoretical efficiency. Achieving ‘well-matched’ scale lengths is one of the primary challenges encountered by miniature systems in the literature because of the respective parameters which determine each scale length.

Variables that influence λ_{RadTr} include: the mass, charge, angular distribution and energy distribution of the source particles; the atomic number, density, and ionization potential of the target material; and the mechanisms through which the particle interacts with the target. These collectively cause λ_{RadTr} to vary greatly among radioisotopes even for the same target material. The factors which determine L_{trans} include the energy conversion mechanism of the battery, the mechanical and electrical properties of the target material, and the effect of radiation damage on the target. The final factor is of essential importance to miniature nuclear batteries in the literature, as new designs demonstrate persistent problems with radiation damage.

In contrast, the RTG design is not concerned with scale-length matching; the sheer size of the RTG ensures that all of the radioisotope energy is deposited within the transducer and converted to heat. However, all of the aforementioned concerns must also be accounted for in a RTG-type miniature nuclear battery design as well. Each one of these factors represents a challenge in matching the range of the radiation to the scale length of potential transducers. In order to better define these challenges, this paper will first look at the characteristics of the various types of radiation sources, focusing on those relevant for small batteries. Then the characteristics of various transducers which are appropriate for energy conversion will be discussed. The principles for integrating radiation sources into transducers will then be examined. Sources of radioisotopes and availability will be discussed. Finally, published systems will be reviewed and critiqued.

2 Conversion of Radiation into Energy

2.1 Characteristics of Radiation Sources

Ionizing radiation is a broad term which refers to the fact that different types of radiation will create ion pairs in matter. Ionizing radiation includes ions (e.g., fission fragments and alpha particles), beta particles, gamma rays, x-rays, and neutrons. Each type of ionizing radiation source has a characteristic range. Consider a material in the solid phase, for example. Swift heavy ions such as fission fragments and alpha particles will deposit their energy within a solid over a distance of micrometers. Electrons deposit their energy over a range of millimeters. Particles which possess high energy and either no rest mass or no net charge, such as gamma rays and neutrons, deposit their energy over a range of meters.

Ionizing radiation ultimately produces heat and ionization through its interaction with matter. Direct energy conversion systems generally use the ion pairs generated in the material to produce current. If no mechanism puts the ionization to use, the energy from the ions will also end up as heat. In typical interactions of ionizing radiation with matter, about 40% to 50% of the energy goes into ionization and the remainder is directly converted to heat. If the mode of energy transduction does not utilize the heat produced by the radiation interactions, the maximum theoretical efficiency for ion pair production will be limited to between 40 and 50%. The maximum theoretical efficiency of each conversion mechanism will be further limited by process inefficiencies specific to the system.

As shown in Figure 1, there are a variety of end-uses for the ionization produced when solids, liquids, and gases are exposed to ionizing radiation. The radiation source, shown as a circle, interacts with matter and branches into heat production and ion pair production. The ions can be used with different transducers to produce a variety of useful products, such as electricity, laser light, or chemicals [6]. In Branch 1, the ions are allowed to recombine and produce heat, which is then combined with the heat initially produced by the interactions between the radiation source and the material. This heat is then used to drive a secondary system to produce electricity. Branch 1 is typical of heat-based nuclear battery concepts such as the RTG [5], thermionic energy conversion [7], thermophotovoltaic [8] or the Alkali Metal Thermal to Electric Converter (AMTEC) [9]. It is also used in the steam cycle for commercial nuclear power plants. Branch 2

utilizes only the energy from the ion pairs and is typical of alphavoltaics [10], betavoltaics [11], reciprocating cantilever [12], etc. Branch 3 utilizes only the energy from the ion pairs for driving a solid state nuclear-pumped laser [13]. Branch 4 utilizes the energy from ion pairs for a solid-state Photon Intermediate Direct Energy Conversion (PIDEC) system [14]. Branch 5 utilizes the energy from the ion pairs for a gaseous PIDEC system [14, 15]. Branch 6 utilizes the energy from the ion pairs to drive a gaseous nuclear-pumped laser [6]. Branch 7 utilizes the energy from the ion pairs for chemical production through radiolysis [6]. The branches which only utilize the energy from ion pair production will inherently be limited to a maximum theoretical efficiency of 40 to 50% since the heat produced in the interaction of radiation with matter is wasted. As will be discussed, process inefficiencies for systems represented by each of these branches will further limit the theoretical maximum efficiency.

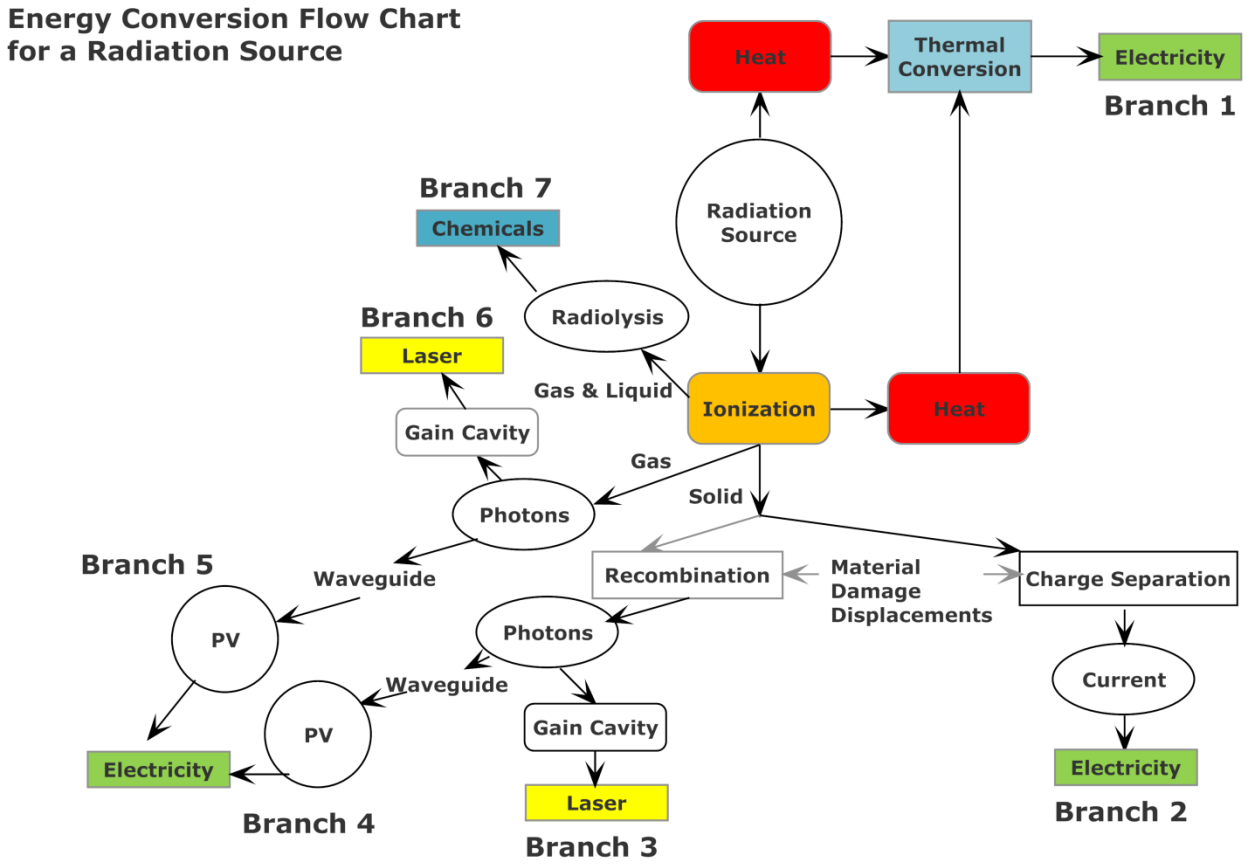

Figure 1. Energy conversion flow chart for radiation sources. Branch 1 uses radiation for heat production. Branch 2 uses the production of charged species in a solid to generate a current flow. Branch 3 uses the production of charged species in a solid to produce laser photons. Branch 4 uses the production of charged species in a solid to produce photons which are used to produce electricity from photovoltaic (PV) cells. Branch 5 uses the production of charged species in a gas to produce photons which then interaction with photovoltaic (PV) cells to produce electricity.

Branch 6 uses the production of charged species in a gas to produce laser photons. Branch 7 uses the production of charged species in a gas or liquid to produce chemicals through radiolysis.

In this section the various types of ionizing radiation will be examined in order of increasing range, beginning with fission fragments. All forms of ionizing radiation are discussed because nuclear battery technologies can be large (like an RTG), but the main focus of this paper will be on swift heavy ions and electrons due to their relatively short ranges, which allows for their use in small-scale nuclear battery configurations. Penetrating radiation like gamma rays or neutrons could theoretically be used, but would require large-scale nuclear battery configurations. These concepts are briefly discussed for completeness.

2.2 Fission Fragments

The shortest transport scale lengths are for ions, and the most massive ions are the fragments produced by fission. Fission commonly occurs through spontaneous decay of a heavy atom like californium-252, which releases fast neutron energy and fission fragments; the neutron energy and fission yield spectra are shown in Figure 2 and Figure 3, respectively. The products of a spontaneous fission event are shown in Equation 1, where ff_l is the light fission fragment, ff_h is the heavy fission fragment, ν is the statistical average number of prompt fission neutrons, n_{fast}, released during fission and are emitted with a typical fast neutron distribution [16, 17]. Fission can also be stimulated by neutron capture, whereby a nucleus absorbs an incident neutron, becomes unstable, and breaks apart. An example of fission initiated through the interaction of thermal neutrons with a fissile material, such as uranium-235, is shown in Equation 2, where n_{th} is a thermal neutron with energy on the order of 25 meV. Thermal fission also releases fast neutrons and fission fragments; the neutron energy distribution and bimodal fission yield distribution of U-235 are shown in Figure 4 and Figure 5, respectively. The average energy produced by particles released in the fission of U-235, including neutrons, gamma rays, beta particles and neutrinos, is shown in Table 1.

$$^{252}_{98}\mathrm{Cf} \rightarrow \mathrm{ff_l} + \mathrm{ff_h} + \nu \cdot \mathrm{n_{fast}} \qquad \text{Equation 1}$$

$$^{235}_{92}\mathrm{U} + \mathrm{n_{th}} \rightarrow {}^{236}_{92}\mathrm{U} \rightarrow \mathrm{ff_l} + \mathrm{ff_h} + \nu \cdot \mathrm{n_{fast}} \qquad \text{Equation 2}$$

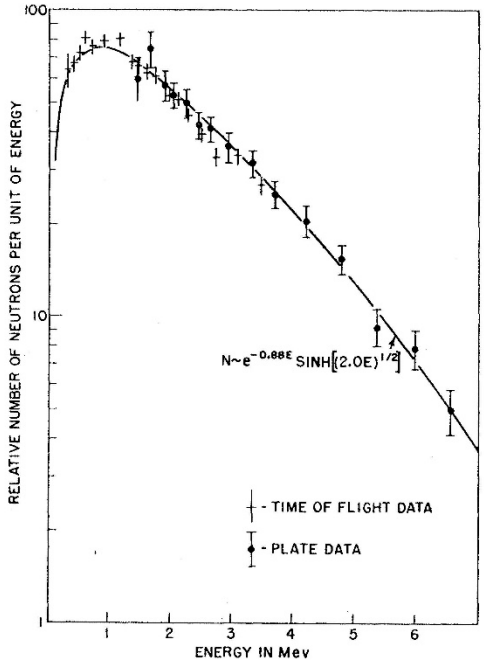

Figure 2. Energy spectrum of neutrons produced by the spontaneous fission of Cf-252 [16].

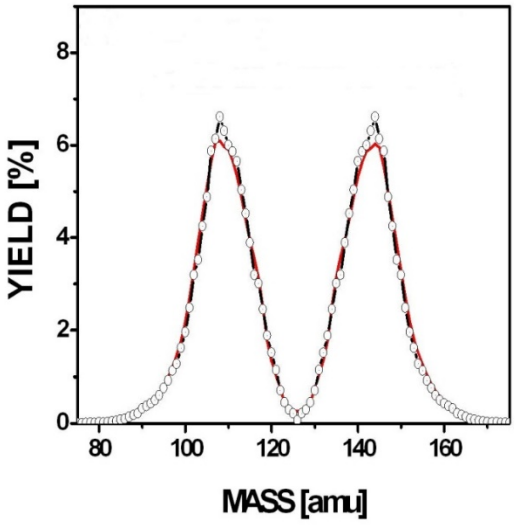

Figure 3. Spontaneous fission yields of Cf-252 [18].

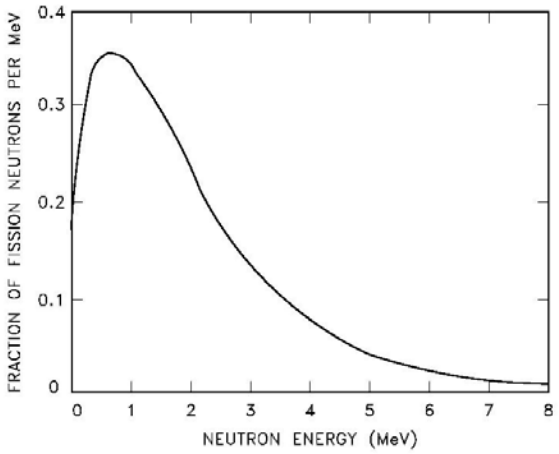

Figure 4. Neutrons energy spectrum produced by the thermal fission of U-235 [19].

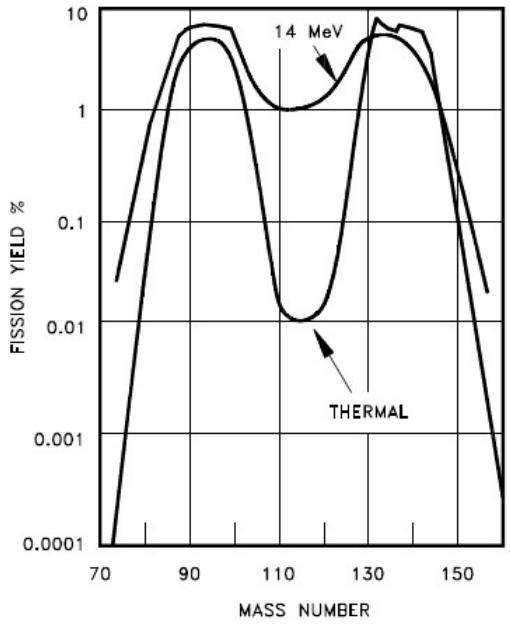

Figure 5. U-235 fission yields for high- and low-energy (thermal) incident neutrons [19].

Table 1: Statistical distribution of energy released in the fission of U-235 [19]

Radiation	Energy in MeV
Kinetic Energy of Fission Fragments	167
Fission Neutrons	5
Prompt Gamma Rays	5

Delayed Gamma Rays from Fission Fragments	6
Capture Gamma Ray Energy	10
Beta Particles from Fission Fragments	7
Neutrinos	10
Total Energy	210

The kinetic energy of each fission fragments depends on the mass of the fragments as shown in Equation 3 and Equation 4, where KE_{ff_l} is the kinetic energy of the light fission fragment, KE_{ff_h} is the kinetic energy of the heavy fission fragment, KE_{ff} is the total kinetic energy of both fission fragments, m_h is the mass of the heavy fission fragment and m_l is the mass of the light fission fragment. The linear energy transfer of fission fragments and other swift heavy ions can be calculated using the Bethe-Bloch formula.

$$KE_{ff_l} = \frac{m_h}{m_h + m_l} KE_{ff} \qquad \text{Equation 3}$$

$$KE_{ff_h} = \frac{m_l}{m_h + m_l} KE_{ff} \qquad \text{Equation 4}$$

For example, consider the specific fission reaction of U-235 shown in Equation 5 that produces La-147 and Br-87. The kinetic energies of the fission fragments are calculated in Equation 6 and Equation 7, respectively, and the energy from the fission reaction products are shown in Table 2. As stated earlier, the ranges of fission fragments in matter are very short due to their mass and charge; the ranges of the two fission fragments used in this example are pictured in Figure 6 and Figure 7. The bromine-87 atom in has a range of 6.29 micrometers (μm) in uranium metal. The spatial energy distributions of both fission fragments within the material are shown in Figure 8 and Figure 9, respectively.

$$^{235}_{92}\mathrm{U} + \mathrm{n_{th}} \rightarrow {}^{147}_{57}\mathrm{La} + {}^{87}_{35}\mathrm{Br} + 2\mathrm{n_{fast}} + \mathrm{Q\ (195\ MeV)} \qquad \text{Equation 5}$$

$$\mathrm{KE_{La-147}} = \frac{87}{147 + 87} 162 = 60.23\ \mathrm{MeV} \qquad \text{Equation 6}$$

$$\mathrm{KE_{Br-87}} = \frac{147}{147 + 87} 162 = 101.77\ \mathrm{MeV} \qquad \text{Equation 7}$$

Table 2. Distribution of energy released during the fission of U-235 which yields the specific fission fragments La-147 and Br-87 [20]. Table 1 is an overall statistical yield for fission while this table is specific to a single fission reaction.

Radiation	Energy in MeV
Kinetic Energy of Fission Fragments	162
Fission Neutrons	6
Prompt Gamma Rays	6
Delayed Gamma Rays from Fission Fragments	5

Beta Particles from Fission Fragments	5
Neutrinos	11
Total Energy	195

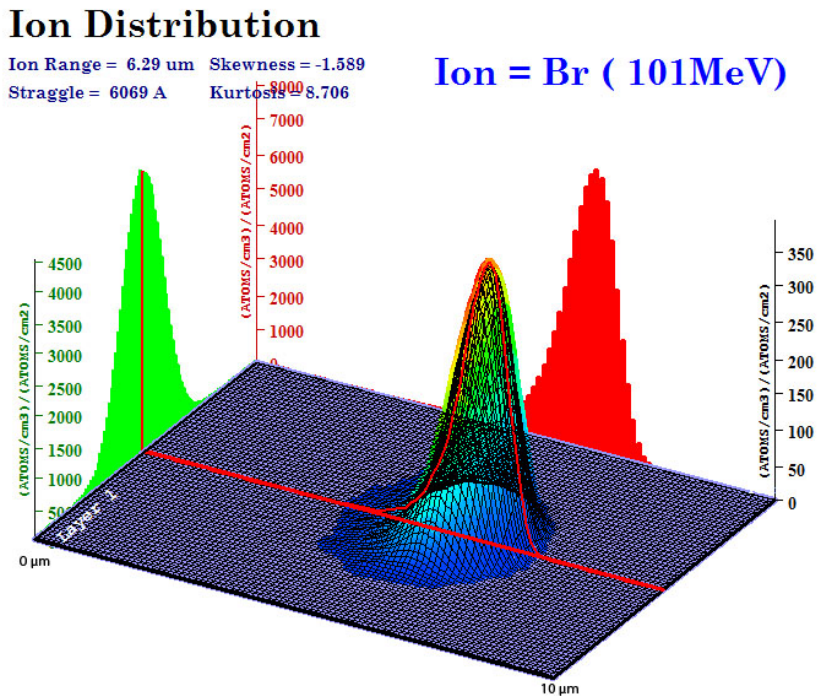

Figure 6. SRIM2011 model showing ion distribution in uranium of 101 MeV bromine-87 ions slowing down [21]. The plot ordinate has units (Atoms/cm^3)/(Atoms/cm^2). By multiplying with ion dose (units of Atoms/cm^2 of bromine-87), the ordinate converts to a density distribution of Br-87 with units of (Atoms/cm^3). The ion source originates from the left side so the two dimensional plane indicates the depth and width of the ion distribution.

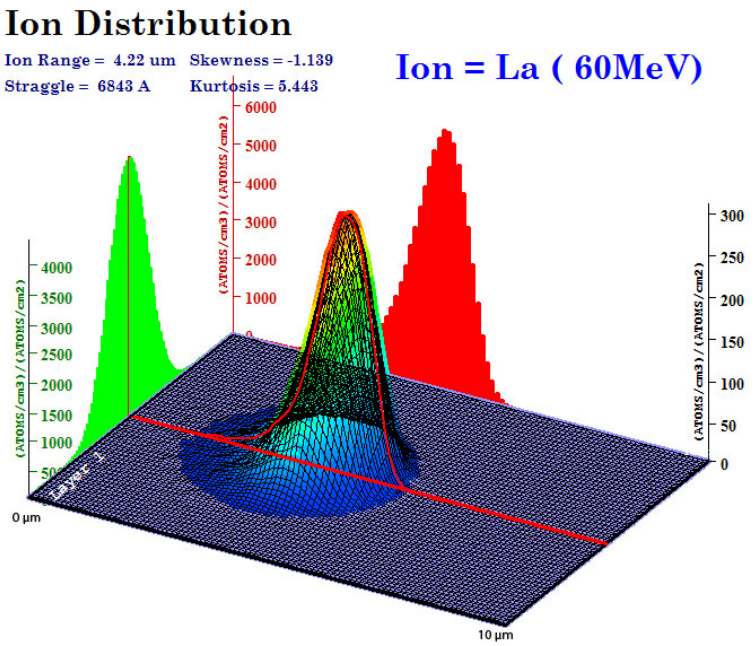

Figure 7. SRIM2011 model showing final ion distribution of 60 MeV lanthanum-147 ions transported through uranium metal[21]. The plot ordinate has units (Atoms/cm^3)/(Atoms/cm^2). By multiplying with ion dose (units of Atoms/cm^2 of La-147), the ordinate converts to a density distribution of La-147 with units of (Atoms/cm^3). The ion source originates from the left side so the two dimensional plane indicates the depth and width of the ion distribution.

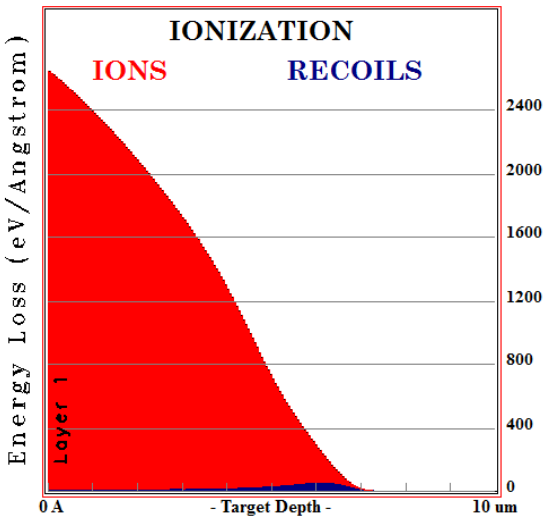

Figure 8. SRIM2011 model showing target ionization in uranium metal by 101 MeV bromine-87 ions[21]. The left ordinate is energy loss (eV/Angstrom), the right ordinate is the number of recoil atoms.

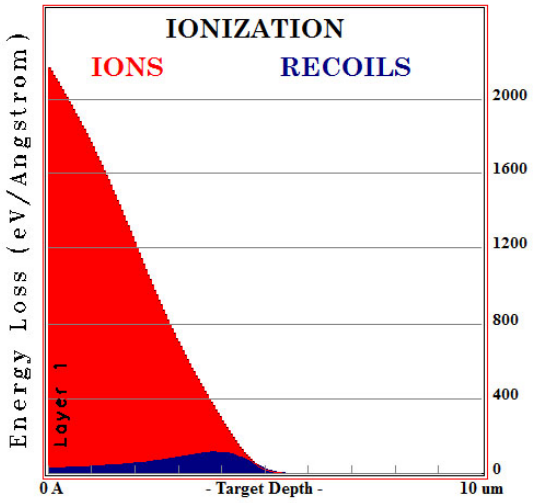

Figure 9. SRIM2011 model of target ionization in uranium metal by 60 MeV lanthanum-147 ion[21]. The left ordinate is energy loss (eV/Angstrom), the right ordinate is the number of recoil atoms.

The fission reaction shown in Equation 8 is the consequence of the interaction of a fast neutron (energy greater than 1 MeV) and U-238. Fast fission of U-238, for example, provides a large part of the explosive yield in a thermonuclear weapon. The energy distribution of the fast fission products is similar to that of products in thermal fission.

$$^{238}_{92}\mathrm{U} + \mathrm{n}_{\mathrm{fast}} \rightarrow {}^{239}_{92}\mathrm{U} \rightarrow \mathrm{ff}_{\mathrm{h}} + \mathrm{ff}_{\mathrm{l}} + \nu \cdot \mathrm{n}_{\mathrm{fast}} \qquad \text{Equation 8}$$

2.3 Alpha Particles

Alpha-emitting radioisotopes which are appropriate for use in a nuclear battery are described in Table 3. Polonium-210 is used an example here (Eq. 9).

$$^{210}_{84}\mathrm{Po}_{126} \xrightarrow{t_{1/2}=138.376\ \mathrm{d}} {}^{206}_{82}\mathrm{Pb}_{124} + {}^{4}_{2}\mathrm{He}^{2+}(5.305\ \mathrm{MeV}) \qquad \text{Equation 9}$$

Alpha particles are swift heavy ions whose interactions with matter are governed by the Bethe-Bloch stopping power equation. The range of an alpha particle (as shown in Figure 10 is 9.32 micrometers in uranium) will be greater than the range of a fission fragment in uranium metal (4.22 micrometers for a heavy fission fragment and 6.29 micrometers for a light fission fragment) due to its lower charge and mass. The ionization produced by an alpha particle along its path in a solid will follow a classical Bragg curve with a Bragg peak (see Figure 11), whereas

a fission fragment has no Bragg peak (see Figures 8 and 9), due to the highly changing linear energy transfer of fission fragments as it picks up electrons during the slowing down process. Further, the range of any charged particle is a function of the electron density of the stopping material, such that less dense materials provide a lower stopping power than higher density materials. For example, the range of 5 MeV alpha particles in air is 40.6 mm (as compared to 9.32 micrometers in uranium metal).Therefore, it is often instructive to talk about ranges in terms of areal density, which is the linear range divided by the density of the material. The areal density is independent of density changes of the absorbing materials and is similar for similar-Z materials (see the next section for more discussion on this concept).

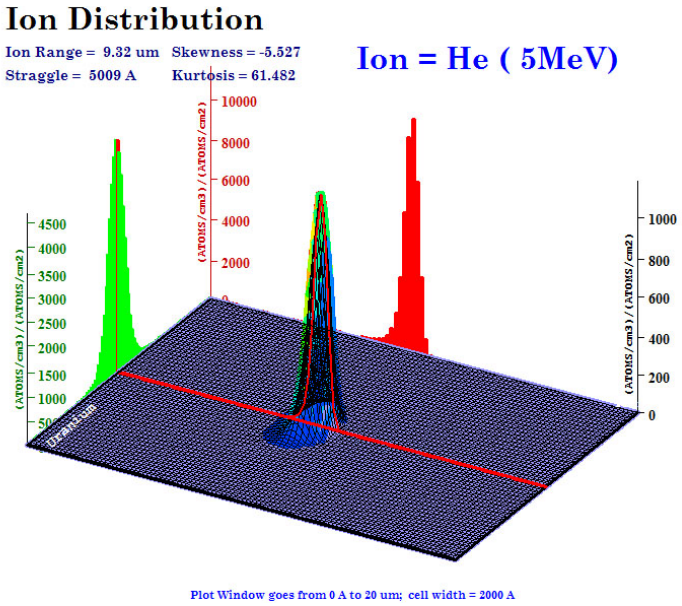

Figure 10. SRIM2011 model showing final ion distribution of 5.3 MeV alpha particles in uranium metal [21]. The plot ordinate has units (Atoms/cm^3)/(Atoms/cm^2). By multiplying with ion dose (units of Atoms/cm^2 of He-4), the ordinate converts to a density distribution of He-4 with units of (Atoms/cm^3). The ion source originates from the left side so the two dimensional plane indicates the depth and width of the ion distribution.

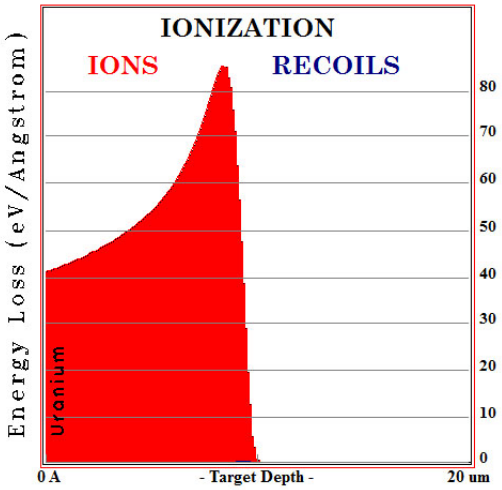

Figure 11. SRIM2011 model showing target ionization produced in uranium metal by 5.3 MeV alpha particles [21]. The left ordinate is energy loss (eV/Angstrom), the right ordinate is the number of recoil atoms.

Table 3: Potential α sources for nuclear batteries. The criteria used in identifying these isotopes is based on a half-life between 0.379 years and 100 years. Other emissions are shown such as gamma emission (for which additional shielding would be needed).

Nuclide	Z	N	Decay Energy (MeV)	Half life (Years)	Other emissions (MeV, %)	Production Reactions
Gd-148	64	84	3.182	74.6	N/A	Sm-147(α,3n) Eu-151(p,4n)
Po-208	84	124	5.216	2.8979	β^+: 0.3783 (0.00223%)	Bi-209(d, 3n) Bi-209(p,2n)
Po-210	84	126	5.305	0.379	γ: 0.803 (0.0011%)	Natural source
Th-228	90	138	5.52	1.9131	α: 5.340 (27.2%) 5.423 (72.2%) γ: 0.216 (0.25%)	Natural source
U-232	92	140	5.414	68.9	α: 5.263 (31.55%) 5.32 (68.15%) γ: 0.1 - 0.3 (low %)	Pa-232(β) Th-232(α, 4n)
Pu-236	94	142	5.867	2.857	α: 5.721 (30.56%) 5.768 (69.26%)	Np-236(β) U-235(α, 3n)
Pu-238	94	144	5.593	87.74	α: 5.456 (28.98%) 5.499 (70.91%)	Np-238(β) Np-237(n, γ)
Am-241	95	146	5.638	432.2	α: 5.442 (13%) 5.485 (84.5%)	Pu-241(β)

					γ: 0.05954 (35.9%)	
Cm-243	96	147	6.168	29.1	α: 5.742 (11.5%) 5.785 (72.9%) 5.992 (5.7%) 6.058 (4.7%) γ: 0.2 – 0.3 (20%)	Multiple-n capture U-238, Pu-239
Cm-244	96	148	5.902	18.1	α: 5.762 (23.6%) 5.805 (76.4%) γ: low percentage	Multiple-n capture U-238, Pu-239, Am-243
Bk-248	97	151	5.793	9		Cm-246(α,pn)
Cf-250	98	152	6.128	13.07	α: 6.0304 (84.6%) 5.989 (15.1%) γ: 0.04285 (0.014%)	Multiple-n capture U-238, Pu-239, Cm-244
Cf-252	98	154	6.217	2.645	SF: FF (3.092%) α: 6.0758 (15.7%) 6.118 (84.2%) γ: 0.043 - 0.155 (0.015%)	Multiple n capture U-238, Pu-239, Cm-244
Es-252	99	153	6.739	1.292	α: 6.5762 (13.6%) 6.632 (80.2%) γ: 0.043 - 0.924 (25%)	Bk-249(α,n) Cf-252(d,2n)

2.4 Beta particles and positrons

An isotope which produces an electron and antineutrino is a β^- emitter, while an isotope which produces a positron and neutrino is a β^+ emitter. Energetic electrons transfer energy to the electrons of the target material via Coulomb scattering and Bremsstrahlung emission as calculated by the modified Bethe formula. Beta-emitting radioisotopes which have suitable half lives are shown in Table 4.

Table 4: Potential β^- sources for nuclear batteries. The criteria used in identifying these isotopes is based on a half-life between 1 year and 269 years. Other emissions are shown such as gamma emission (for which additional shielding would be needed).

Nuclide	Z	N	Decay Energy (MeV)	Half life (Years)	β_{max} (MeV)	Other emissions (Units in MeV)	Production Method
H-3	1	2	0.019	12.33	0.019	N/A	Li-6(n, α)
Ar-39	18	21	0.565	269	0.565	N/A	Ar-38(n, γ) KCl(n, γ)

Ar-42	18	24	0.6	32.9	0.6	N/A	Ar-40(n, γ) Ar-41(n, γ)
Co-60	27	33	2.824	5.2713	0.318	γ: 1.17 (99%) 1.33 (0.12%)	Co-59(n, γ)
Kr-85	36	49	0.67	10.755	0.67 (99.6%) 0.15 (0.4%)	γ: 0.514 (0.4%)	Fission product
Sr-90	38	52	0.546	28.77	0.546	2.281 (Y-90, daughter)	Fission product
Ru-106	44	62	0.039	1.0234	0.039	N/A	Fission product
Cd-113m	48	65	0.58	14.1	0.58	N/A	Cd-112(n, γ) Cd-113(n, n')
Sb-125	51	74	0.767	2.73	0.7667	γ: 0.5 (5 - 20%)	Sn-124(n, γ)
Cs-134	55	79	2.058	2.061	0.662 (71%) 0.089 (28%)	γ: 0.6 - 0.8 (97%)	Cs-133(n, γ)
Cs-137	55	82	1.175	30.1	1.176 (6.5%) 0.514 (93.5)	γ: 0.6617 (93.5%)	Fission Product
Pm-146	61	85	1.542	5.52	0.795	γ: 0.747 (33%)	Nd-146(p,n) Nd-148(p,3n)
Pm-147	61	86	0.225	2.624	0.225	N/A	Nd-146(n, γ)
Sm-151	62	89	0.076	90	0.076	N/A	Fission product
Eu-152	63	89	1.822	13.54	1.818	γ: 0.1 - 0.3	Eu-151(n, γ)
Eu-154	63	91	1.969	8.592	1.845 (10%) 0.571 (36.3%) 0.249 (28.59%)	γ: 0.123 (38%), 0.248 (7%), 0.593 (6%), 0.724 (21%), 0.759 (5%), 0.876 (12%), 1.0 (31%), 1.278 (37%)	Eu-153(n, γ)
Eu-155	63	92	0.253	4.67	0.147 (47.5%) 0.166 (25%) 0.192 (8%) 0.253 (17.6%)	γ: 0.086 (30%) 0.105 (21%)	Sm-154(n, γ)
Tm-171	69	102	0.096	1.92	0.0964 (98%) 0.0297 (2%)	γ: 0.0667 (0.14%)	Er-170(n, γ)

Os-194	76	118	0.097	6	0.0143 (0.12%) 0.0535 (76%) 0.0966 (24%)	γ: 0.01 - 0.08	Os-192(n, γ) Os-193(n, γ)
Tl-204	81	123	0.763	3.78	0.763	N/A	Tl-203(n, γ)
Pb-210	82	128	0.063	22.29	0.0169 (84%) 0.0635 (16%)	γ: 0.046 (4%)	Natural source
Ra-228	88	140	0.046	5.75	0.0128 (30%) 0.0257 (20%) 0.0392 (40%) 0.0396 (10%)	γ: low E (low %)	Natural source
Ac-227	89	138	0.044	21.773	0.02 (10%) 0.0355 (35%) 0.0448 (54%)	α: 4.953 (47.7%) 4.940 (39.6%) γ: 0.1 to 0.24 γ	Ra-226(n, γ)
Pu-241	94	147	0.021	14.35	0.02082	α: 4.853 (12.2%) 4.896 (83.2%)	Multiple-n capture U-238, Pu-239

If an isotope instead emits a positron, the β^+ will encounter some electron in orbit around an atom. The two will then mutually annihilate to produce two energetic gamma rays. These gamma rays then interact with matter using mechanisms which are very different from those of electrons or other charged particles; these interactions are covered in §2.6.

Compared to swift heavy ions, the path of an electron in matter is complicated. Because the incident electron has a mass equal to that of the electrons in the target, the electron undergoes significant scattering and follows the random walk-like path shown in Figure 12 and Figure 13. The range *R* of electrons can be estimated using rules of thumb, for example Equation 10 and 11 can be used to estimate the range of electrons in air. On the whole, rules of thumb such as these are useful for radiation protection considerations but, as discussed below, the usefulness of any rule of thumb quickly breaks down when applied to nuclear battery systems.

$$\mathrm{R_{air}(ft)} \approx 12\ \mathrm{ft/MeV} \qquad \text{Equation 10}$$

$$\mathrm{R\ (kg/m^2)} = \mathrm{R(m)} \cdot \rho\mathrm{(kg/m^3)} \qquad \text{Equation 11}$$

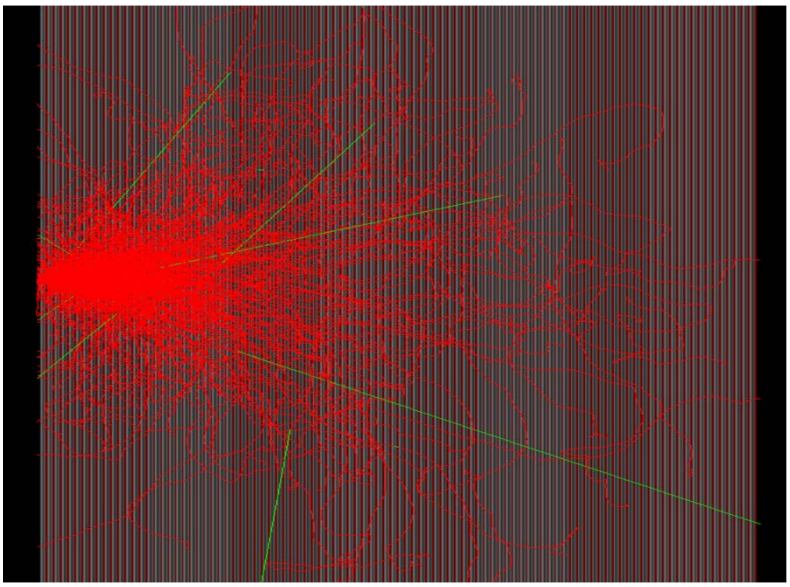

Figure 12. GEANT4 simulation of Sr-90 Beta Decay into SiC of Slab, showing beta particle tracks (random walk path) and bremsstrahlung photons (straight lines)**[22]**.

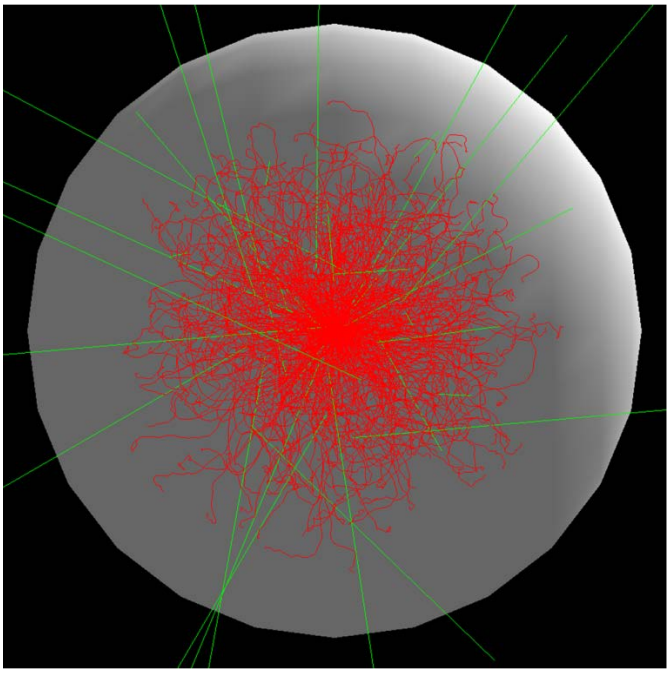

Figure 13. GEANT4 simulation of Sr-90 Beta Decay into SiC of Spherical Model, showing beta particle tracks (random walk path) and bremsstrahlung photons (straight lines)[22]

An ion pair which is produced from the interaction of beta particles with matter includes an electron which is kicked out of orbit during the Coulomb interaction; this electron is referred to as a secondary electron. Secondary electrons typically have kinetic energies in the keV range [23]. The secondary electrons create tertiary electrons through ionization and the tertiary electrons can interact to create quaternary, quinary, or higher-order electrons. Because of their equal mass and charge, electrons can transfer their full energy to a target electron through Coulomb interactions. Nonetheless, the electron energy distribution in an electron beam excited plasma [24] is very similar to the spectra created by light ion bombardment (Figure 14).

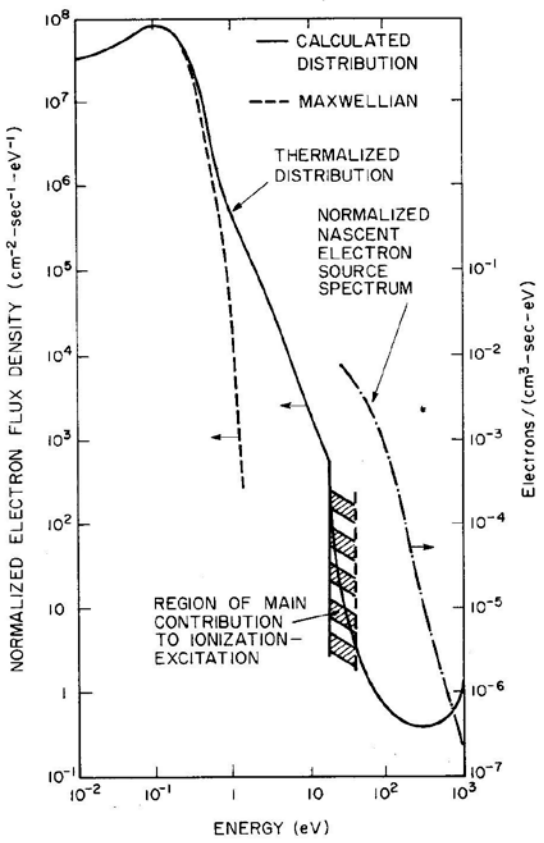

Figure 14. Nascent and asymptotic electron energy distributions for 1-MeV alpha particle bombardment of helium [23].

For example, the maximum energy of the beta particle produced by the decay of phosphorus-32 (^{32}P) is 1.71 MeV. According to Equation 10 the range of the beta particle in air is $1.71 \times 12 = 20.5$ ft ≈ 21 ft. For health physics professionals, this number would be used as an estimate for a safe distance from the source.

There are also similar conservative calculations used by professionals to estimate shielding thicknesses. The concept of areal density is the basis of one such method. It can also be used to conservatively estimate the range of a beta particle in a target material. The areal density is the

density of a target material per square centimeter. The areal density is related to the electron density of a given material which is dependent upon the atomic density and atomic number of that material. Since beta particles interact with the electrons which make up the atom, it also can be used to estimate the amount of energy lost by the beta particle as a function of distance (μm^{-1}). Materials with higher electron density have more electrons for the beta particle to interact with and thus will stop the electron in a shorter distance. So is the areal density is calculated for a specific material using Equation 11 where ρ is the mass density of the material in g/cm^3. In many texts, the areal density is also referred to as 'the range' and given the symbol *R*. The reader must sort out how the term 'range' is used in each reference. There are rules of thumb for areal density which are shown in Equation 12 - Equation 16, where E_{max} is the maximum beta energy in MeV, and areal density is given in g/cm^2 (and uses the symbol *R*).

$$E_{max} \approx 2 \cdot R(g/cm^2) \quad \text{for } 1 \leq E_{max} \leq 4 \text{ MeV} \quad \text{Equation 12}$$

$$E_{max} \approx 1.92 \cdot R^{0.725} \quad \text{for } R \leq 0.3 \text{ g/cm}^2 \quad \text{Equation 13}$$

$$R(g/cm^2) \approx 0.407 \cdot (E_{max})^{1.38} \quad \text{for } E_{max} \leq 0.8 \text{ MeV} \quad \text{Equation 14}$$

$$E_{max} \approx 1.85 \cdot R + 0.245 \quad \text{for } R \geq 0.3 \text{ g/cm2} \quad \text{Equation 15}$$

$$R(g/cm^2) \approx 0.542 \cdot E_{max} - 0.133 \quad \text{for } E_{max} \geq 0.8 \text{ MeV} \quad \text{Equation 16}$$

Models which calculate energy deposition using rules of thumb to find areal density, and therefore particle ranges, will introduce significant errors if used in nuclear battery calculations. The rules of thumb presented above overestimate particle range in order to ensure adequate radiation protection. For example, consider the beta emissions of sulfur-35 ($^{35}_{16}S$), strontium-90 ($^{90}_{38}Sr$), and yttrium-90 ($^{90}_{39}Y$). The maximum energy of the beta particle emitted by ^{35}S is 0.167 MeV, which results in a required areal density of $0.407(0.167)^{1.38} \approx 0.034$ (g/cm^2) by Equation 14. For a silicon carbide target with density ρ = 3.210 g/cm^3, the estimated range would be *R*(cm) $\approx R(g/cm^2)/\rho \approx 0.034/3.210 \approx 0.0106$ cm. The maximum energy of a beta particle emitted by ^{90}Sr is 0.546 MeV, which has an estimated areal density of $0.407\ (0.546)^{1.38} \approx 0.177$ (g/cm^2), and the estimated range is *R*(cm) $\approx R(g/cm^2)/\rho \approx 0.177 / 3.210 \approx 0.0551$ cm. The 2.28 MeV maximum energy of the beta particle emitted by ^{90}Y is considerably higher than the two previous examples. Equation 16 has an areal density of $2.28/2 \approx 1.14$ (g/cm^2) to stop the particles, which equates a range in silicon carbide of *R*(cm) $\approx R(g/cm^2)/\rho \approx 1.14/3.21 \approx 0.355$ cm.

When two rules of thumb cover the same energy space, the significant errors between them are obvious. For example, Equation 16 covers beta energies greater than 0.8 MeV and equation 12 covers beta energies between 1 and 4 MeV. If Equation 16 is used to estimate the range for a Sr-90 beta, it yields $0.546x2.280\text{-}0.133 \approx 1.103$ (g/cm^2) and a consequent range in cm of approximately equal to *R*(m) $\approx R(g/cm2)/\rho \approx 1.103/3.210 \approx 0.344$ cm. The difference between the two rules of thumb (Equations 12 and 16) is about 11 μm, an order of magnitude larger than the transducer scale length of some microscale nuclear battery designs. Rules of thumb should never be used to design a nuclear battery.

It should also be noted that most alpha and beta emitters considered in nuclear battery technology do not emit gamma rays due to potential shielding concerns. For instance, if Co-60 is utilized in a beta-based nuclear battery, then for 1 mW of power, assuming a 100% conversion efficiency and complete escape of the high energy gamma rays, would require 1.76 Ci. The associated high energy gamma ray radiation from this large activity limits its suitability in many situations where radiation effects to surrounding materials (e.g. electronics) and personnel is of importance. This is particularly true for microscale nuclear batteries, where the shielding required to reduce the gamma-ray flux to acceptable levels oftentimes severely reduces the overall energy density (W_e/kg) of the battery, which also increases the battery footprint as a consequence.

In addition to the rules of thumb above, there are other simplifications that may misrepresent energy deposition and, therefore, device efficiency. One common, but incorrect, assumption is that all beta particles are emitted with an energy of 1/3 β_{max} [25]. This simplifies the calculation of energy deposition vs. depth curve for the device, but at the cost of verisimilitude. The ionization profile produced by a true spectrum of beta particles is significantly different from the results of either the simple rules of thumb described above or the 1/3 β_{max} assumption would indicate. A second fatal simplification arises when it is assumed that the ionizing particles are not emitted isotropically. The lack of accurate transport models creates shifts in the energy deposition profile within the energy transducer, so a higher fraction of the incident energy is deposited deeper within the device, which is not the case [26]. Realistic modeling of these sources is essential to accurately represent energy deposition within the nuclear battery. Three relevant beta-decay reactions with low-, medium- and high-energy are shown in Equations 17 to 19.

$$^{35}_{16}\mathrm{S} \rightarrow {}^{35}_{17}\mathrm{Cl} + \beta^{-} + \bar{\nu} + 167.47\ \mathrm{keV} \qquad \text{Equation 17}$$

$$^{90}_{38}\mathrm{Sr} \rightarrow {}^{90}_{39}\mathrm{Y} + \beta + \bar{\nu} + 546\ \mathrm{keV} \qquad \text{Equation 18}$$

$$^{90}_{39}\mathrm{Y} \rightarrow {}^{90}_{40}\mathrm{Zr} + \beta + \bar{\nu} + 2.28\ \mathrm{MeV} \qquad \text{Equation 19}$$

Table 5 shows pertinent data for the three beta emitters, including half-life, the average beta energy according to the commonly-used rule of thumb (1/3 β_{max}), and the average beta energy calculated using the beta spectrum. As can be seen in Figure 15, the sulfur-35 beta spectrum intensity continuously increases as energy decreases, the beta spectrum intensity of the medium-energy strontium-90 emitter tends to flatten out at low energies, and the high energy yttrium-90 beta spectrum intensity has a distinct maxima and then drops as energy decreases. As can be seen in Table 5, the differences between the average energy calculated by the 1/3 β_{max} rule and the average energy calculated directly from the spectrum differs significantly as the maximum energy of the beta particle increases. If the average beta energy is calculated using the 1/3 β_{max} rule, the error inherent in using the 1/3 β_{max} rule is propagated through the rest of the system calculations. These incorrect average energies will then be used to calculate incorrect estimates of particle range and stopping power. The 1/3 β_{max} rule should not be used for design calculations and modeling of nuclear batteries.

Table 5. Characteristics of common beta-emitting radioisotopes. The average energy is calculated using the 1/3 β_{max} rule and using a full spectrum analysis. The differences in the average energy are substantial for high energy beta sources.

Isotope	Half-Life	Max Energy	Average Energy		% Difference	Daughter Isotope
			1/3 βmax rule	spectrum		
S-35	87.51 days	167.47 keV	55.8 keV	53.1 keV	+5	Cl-35
Sr-90	28.8 years	546 keV	182 keV	167 keV	+9	Y-90
Y-90	2.67 days	2.28 MeV	760 keV	945 keV	-20	Zr-90

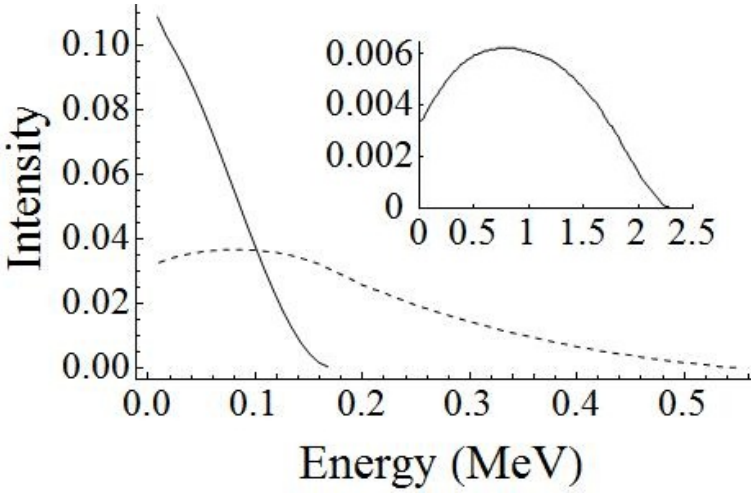

Figure 15. Beta emission energy spectra for S-35 (solid), Sr-90 (dashed), and Y-90 (inset) [22]

Accurate range calculations are essential when designing a nuclear battery in order to match the active region of the transducer (L_{trans}) in the optimum position to harvest the energy from the beta particle (λ_{RadTr}). To calculate the range of a beta particle in matter, the full beta energy spectrum should be used in the model (Figure 15). Calculations which use the complete beta spectrum lead to the best possible estimation of energy deposition profiles. This is clearly shown in the following example. The actual range of beta particles from S-35, Sr-90 and Y-90 decay have been calculated for a beam of beta particles hitting a slab and for a point source in the center of a sphere [22]. These results are significantly different from results that use the average beta energy calculated from the beta spectrum. This further reinforces the premise that unacceptable inaccuracies come from the use of any rules of thumb (Equations 13-16) when designing a nuclear battery. Results from the rules of thumb are several orders of magnitude

larger than calculations based on the average beta energy (using the average based on the beta spectrum) or the full beta spectrum. It is interesting that there is about a factor of 4 difference between the range calculated from average beta energy and the range calculated with the full beta spectrum, where the range for the full beta spectrum is greater.

Figure 16 and Figure 17 represent the energy deposition as a function of distance for a calculation based on the average beta energy and a calculation based on the full beta spectrum, respectively. In the slab geometry, the beta particles were simulated as monodirectional, normal to the stopping material, whereas the point source in the sphere was modeled as isotropic. The results are notably different and again reinforce why designs based on average beta energy have significant errors. Looking at Figure 15, the beta spectrum from each of the isotopes that are represented in this discussion, it is apparent that there is a significant distribution of low energy beta particles which are emitted. By definition, the average beta energy is at the point where the number of beta particles greater than the average energy equal to the number of beta particles less than the average energy. For S-35, the low energy beta population continually increases as the energy approaches zero. For Sr-90, there is a slight peak at 0.08 MeV, but generally the population is flat at lower energies. For Y-90, there is a well-defined maximum in the spectrum at 0.8 MeV. The differences between Figures 16 and 17 are not so surprising when the low energy betas in a full spectrum are taken into account.

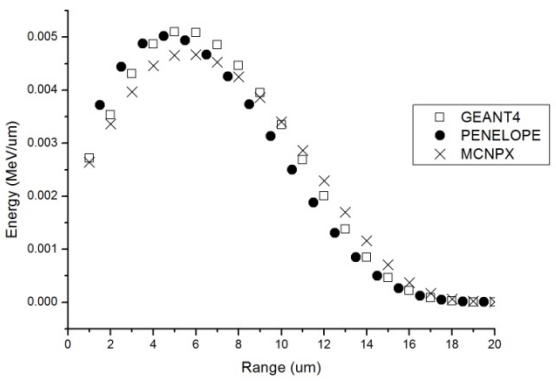
Energy (MeV/um)
Range (um)
GEANT4
PENELOPE
MCNPX

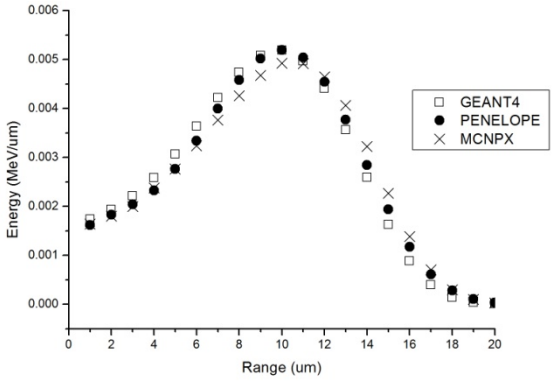
Energy (MeV/um)
Range (um)
GEANT4
PENELOPE
MCNPX

(a)

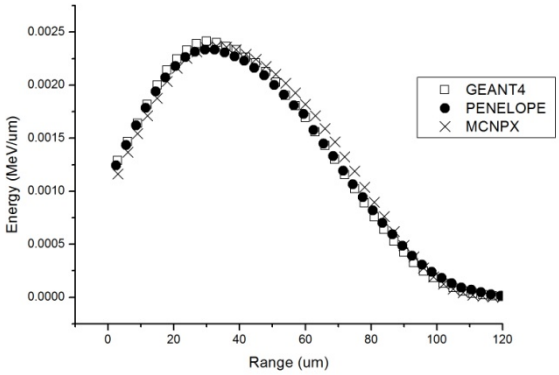
Energy (MeV/um)
Range (um)
GEANT4
PENELOPE
MCNPX

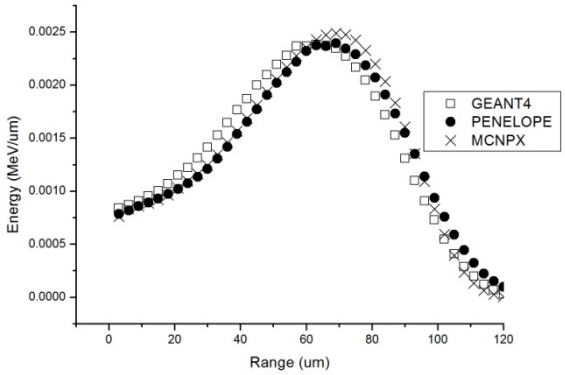
Energy (MeV/um)
Range (um)
GEANT4
PENELOPE
MCNPX

(b)

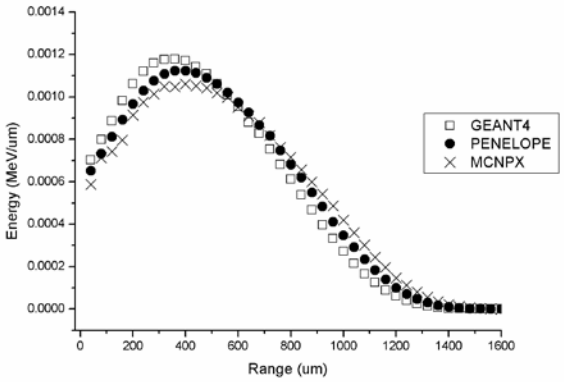
Energy (MeV/um)
Range (um)
GEANT4
PENELOPE
MCNPX

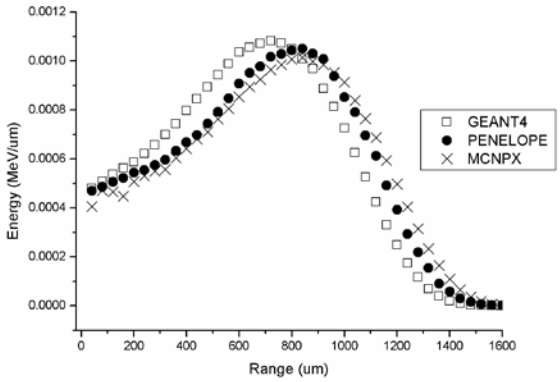
Energy (MeV/um)
Range (um)
GEANT4
PENELOPE
MCNPX

(c)

Figure 16. Simulated energy deposition based on the average beta energy versus distance in both the monodirectional beta source incident on a slab (left) and an isotropic source at the center of a spherical (right) geometries using GEANT4, PENELOPE, and MCNPX codes for (a) S-35, (b) Sr-90, (c) Y-90. [22]

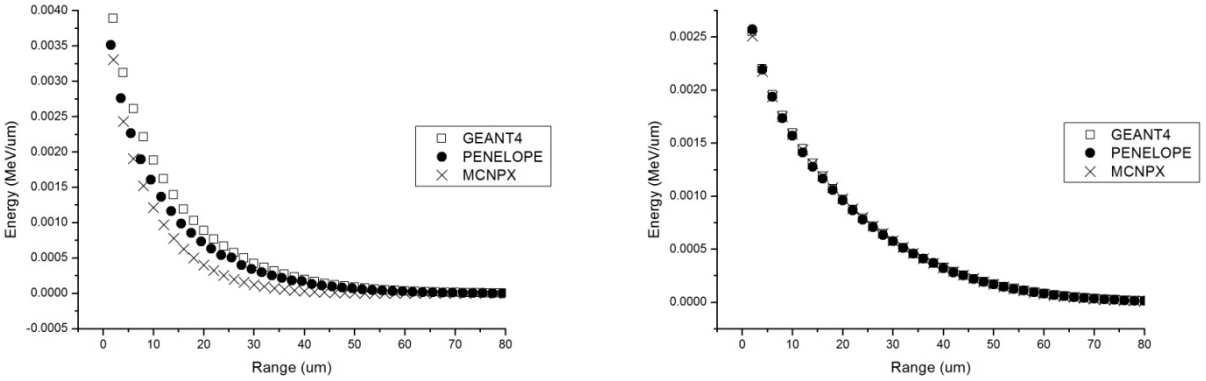

(a)

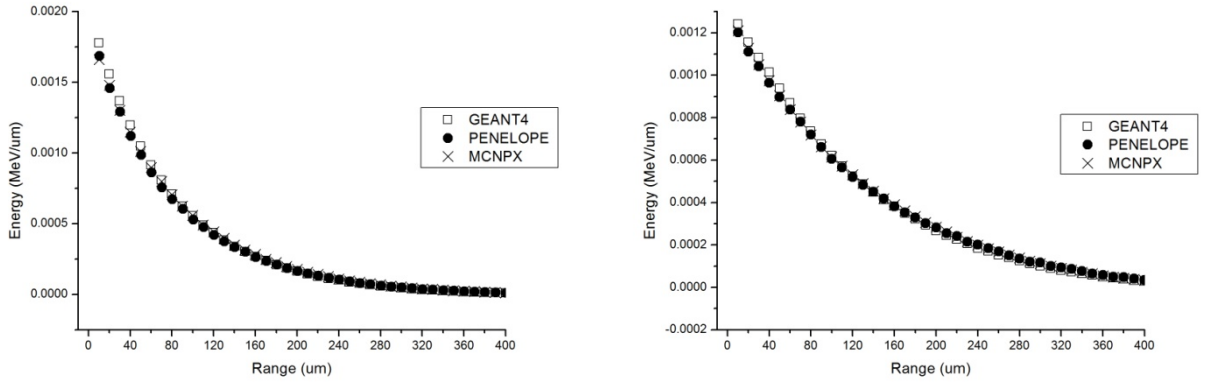

(b)

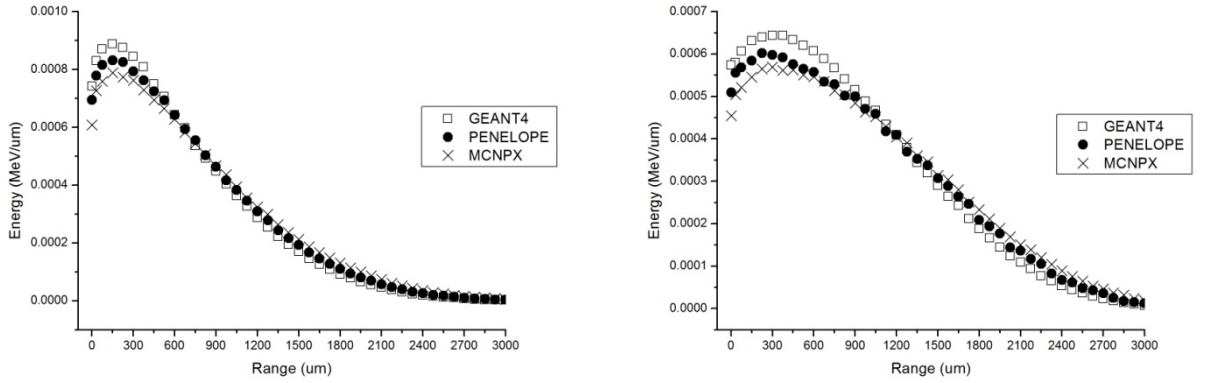

(c)

Figure 17 Simulated energy deposition based on the full beta energy spectrum versus distance for the monodirectional beta source incident on a slab (left) and an isotropic source at the center of a spherical (right) models using GEANT4, PENELOPE, and MCNPX codes for (a) S-35, (b) Sr-90, (c) Y-90.

In the calculations based on average beta energy shown in Figure 16, there are distinct peaks for both the slab and spherical geometries for S-35, Sr-90 and Y-90. For S-35, the peaks occur at 6 μm for the slab geometry and at 10 μm for the spherical geometry. For Sr-90, the peaks occur at 35 μm for the slab geometry and at 65 μm for the spherical geometry. For Y-90, the peaks occur at 400 μm for the slab geometry and at 600 μm for the spherical geometry. In contrast, Figure 17 shows that low energy betas from the spectrum dominate where the energy is deposited. Low energy betas will have a shorter range in the material than high energy beta particles. So, the energy deposited per unit depth into the stopping material for both S-35 and Sr-90 is highest near the surface of the stopping material and decays exponentially with depth. For the high energy Y-90 beta particles there is a distance where energy deposition peaks. For the slab case it peaks at 150 μm and for the spherical case it peaks at about 300 μm. Another interesting observation is that the maximum amount of energy that is deposited is substantially different (about a factor of two lower) for the full spectrum calculation as opposed to the average energy calculation.

The implications of the observations above are significant. First of all, in using average beta energy to calculate the location of maximum energy deposition, and therefore the location of the transducer, there will be substantial errors in placement of the depletion layer within the cell. A betavoltaic cell is a p-n junction in which the p type material and n-type material form a junction through compensation. This region in the cell is called the depletion zone. As will be discussed, by adjusting the density of p type impurities and n-type impurities, the depletion layer width will change. Typically, the depletion layer width in a well-designed cell will be about 1 μm thick. If the betavoltaic cell is viewed as a box, then it is possible to locate the depletion zone within the boundaries of the box. The challenge is to deposit as much of the energy from the source's beta particles into the 1 μm thick depletion layer as possible. Realizing that the slab model is idealized in that a monodirectional beta particle beam strikes the cell normal to the surface and that the spherical model is idealized by placing a point source at the center of the sphere where the beta source is equidistant from a shell within the sphere, both models vastly over predict the beta energy being deposited in any given layer. In a realistic device the beta source will be isotropic, thus creating a much greater challenge for depositing the energy of the beta particles in the thin depletion layer. In summary, by using average beta energies in design calculations, significant errors are made in locating the optimum position for the depletion layer. There is also a significant error in calculating the energy transfer rate to the depletion layer.

Table 6. Range of beta particles in SiC based on the rules of thumb from Equation 13 - Equation 16 compared to results in Figure 16 and Figure 17. The results from the beta spectrum are exact and this table shows the magnitude of expected errors in calculations which use rules of thumb or average beta energy.

Radioisotope	Range in millimeters		
	Rule of Thumb	Average Beta	Beta Spectrum
S-35	10.6	0.02	0.08
Sr-90	55.1	0.12	0.40
Y-90	344.0	1.6	3.00

2.5 Neutrons

Neutrons are released during fission (neutron capture induced or spontaneous), fusion, and nuclear reactions between high energy particles and a target material. Neutrons produced in nuclear reactors through the fission reaction, such as Equation 2, are born at energies above 1 MeV (see Figure 4). Neutrons may also be created through spontaneous fission such as in Cf-252 (Figure 18) or released in fusion reactions. Fusion requires that the fusing nuclei in the reaction have sufficient energy in the center of mass frame to overcome the Coulomb barrier. The required energies are generated by fusion reactors (which create high temperature plasmas) or by accelerators. Typical fusion reactions are,

$$D + D \rightarrow \begin{cases} T + p + 4.03\ \text{MeV}\ (50\%) \\ He^3 + n_{fast} + 3.27\ \text{MeV}\ (50\%) \end{cases} \qquad \text{Equation 20}$$

$$D + T \rightarrow He^4 + n_{fast} + 17.6\ \text{MeV} \qquad \text{Equation 21}$$

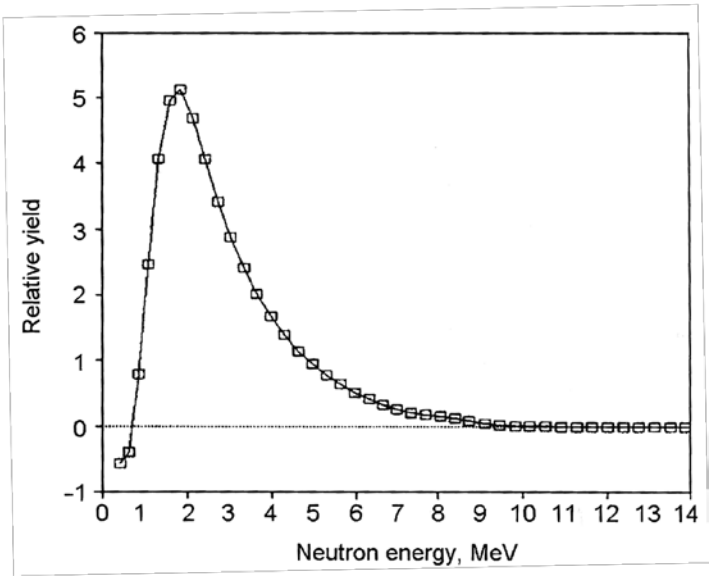

Figure 18. Neutron spectra from the spontaneous fission of Cf-252 [27].

The neutron energies from fusion reactions have a very narrow energy spectrum. In the case of the D-D reaction, the neutron energy is 2.45 MeV. In the case of D-T, the neutron energy is 14.1 MeV. Neutrons are not charged and thus will have no electromagnetic interactions with the cloud of electrons in an atom. Neutrons will only collide with a nucleus and will only lose energy through these collisions. Even with solids the volume taken up by nuclei is very small, so the probability of a collision between a neutron and a target nucleus will be low. The amount of energy that a neutron will give up when colliding with a nucleus is based on the principles of an elastic collision governed by conservation of momentum and conservation of energy. If the mass of the target nucleus is comparable to the mass of the neutron that collides with it, the neutron will bounce off giving up some of its energy. If the mass of a target nucleus is significantly heavier than the neutron, then the collision does not reduce the energy of the neutron very much. Neutrons will lose more energy if the target atoms are light. The rate of energy loss will be greatest if the target material has a high density of light nuclei. That is why neutron shields are made up of materials with a high density of hydrogen atoms.

Table 7. The half thickness (the thickness where a beam of neutrons will lose half of its intensity) of a plate made of a given material that is exposed to a Po-Be neutron source [28].

Material	Half Thickness (cm)
Paraffin	6.6
Water	5.4
12% Borax in Water	5.3
Brass	4.9
Steel (Cold Rolled)	4.9
Lead	6.8
Aluminum	7.8

The effective range of neutrons in matter is a function of the mass of the target atoms and the density of the material. Neutrons most effectively interact with atoms with low atomic mass like hydrogen, helium, beryllium and carbon. High density, low atomic number materials are most effective for neutrons losing energy by elastic scattering. The range of neutrons in a gas, even at high pressures, is very long. For example, the range of 2.45 MeV neutrons in 200 atmospheres of helium is on the order of 30 meters. Even in solids with a high atomic density of hydrogen, like paraffin (Table 7), the range is on the order of a half meter (it takes about 6 half thicknesses to achieve 99% energy loss). In terms of nuclear batteries, any fission or fusion processes considered for energy production appear to be poor candidates. Isotopes such as Cf-252 spontaneously fission but the large range of neutrons in matter would yield large nuclear battery systems with a very low power density. With regard to fusion, the only possible reactions on a small scale reported in the literature are those based on “Cold Fusion”. This is a controversial area of research which appears to produce heat at levels beyond the capability of chemical reactions. The type of particles that may be created in such hypothetical nuclear reactions have not yet been identified.

2.6 Gamma Rays

Gamma rays are electromagnetic radiation (photons) and possess no charge or rest mass. There are three processes by which gamma rays interact with matter: the photoelectric effect; Compton scattering; and pair production. In the photoelectric effect, the photon, which is incident on the atom, loses all of its energy to an orbital electron. The photon is absorbed by the electron and the electron is ejected from the atom leaving behind a positive ion. The probability of the photoelectric effect is highest when the photon energy is low and if the material is made up of high Z atoms. Compton scattering occurs when the photon interacts with an electron orbiting an atom, which ejects the electron and scatters the photon to lower energies. This interaction conserves momentum and energy as shown in Equation 22 where E_e is the energy transferred to the electron and E_s is the energy of the photon after the scattering event.

$$h\nu = E_e + E_s \text{ (conservation of energy)} \quad \text{(Equation 22)}$$

In addition, momentum is conserved and there is an angular distribution. At a low energy, most of the initial energy is scattered (E_s > 80% ($h\nu$) when $h\nu$ <1 keV). When the charge of the atom (Z_e) increases, the probability of interaction also increases. Compton scattering is practically independent of Z because the probability of interaction decreases as the photon energy increases. Pair production occurs when a photon spontaneously transforms into an electron and positron in the presence of an intense electrical field near a nucleus. The photon energy has to be greater than 1.022 MeV, the rest mass energy of the electron-positron pair. The mass attenuation coefficient for gamma rays is illustrated in Figure 19 [25].

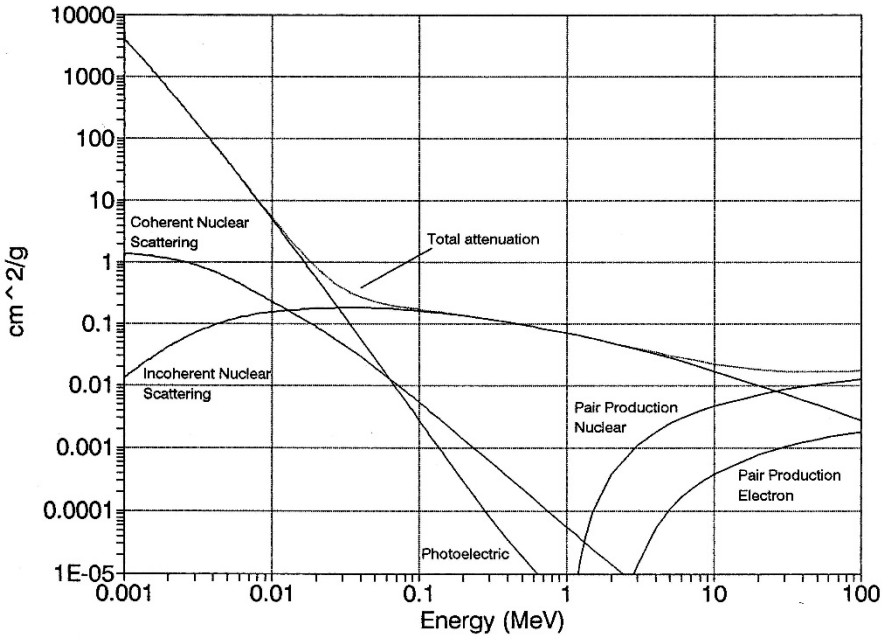

a) Water

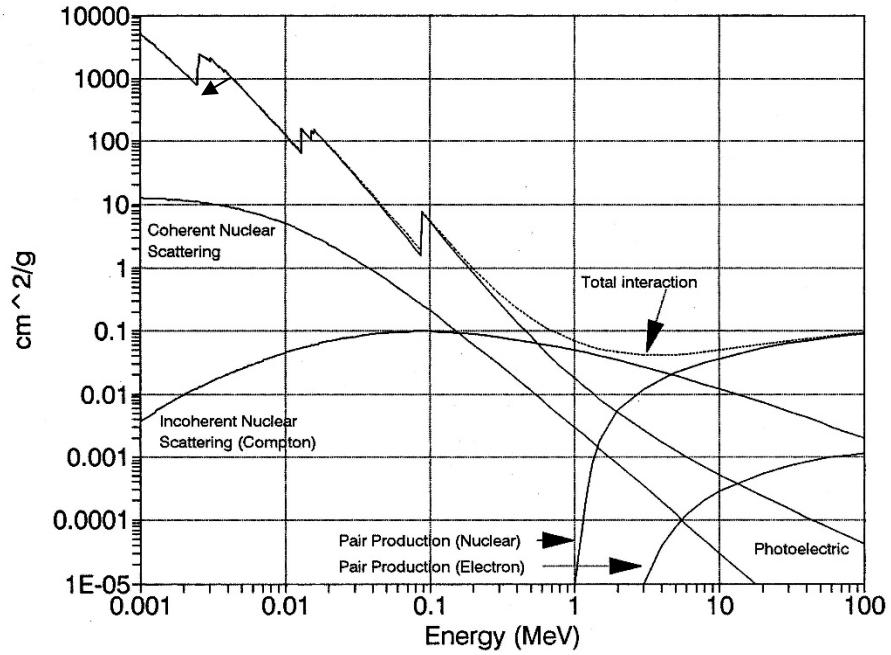

b) Lead

Figure 19. The mass attenuation coefficients for gamma rays of various energies are shown in a) water and b) lead. Note that at low energies the photoelectric effect dominates. At energies near 0.1 MeV, Compton scattering dominates and at very high energies pair production dominates [25].

The effective range of gamma rays in matter can be calculated using Equation 23, where I is the intensity or exposure rate, I_0 is the original radiation intensity or exposure rate, μ is the linear attenuation coefficient (cm^{-1}), μ/ρ is the mass attenuation coefficient (cm^2/gm), ρ is the absorber density (gm/cm^3), and x is the absorber thickness (cm).

$$I = I_0 e^{-\mu x} = I_o e^{-\left(\mu/\rho\right)\rho x} \quad \text{Equation 23}$$

If we choose water as the medium and a gamma ray with 0.6 MeV energy, the mass attenuation coefficient, μ/ρ, is 0.1 cm^2/gm (Figure 19a). Assuming that the range can be approximated as the point where the intensity of the beam drops to 1%, you can estimate the effective range using Equation 23. The range for a 0.6 MeV gamma ray in water is ~46.1 cm. For 100 atm of Ar, the mass is 0.1664 gm/cm^3 so the effective range of a 0.6 MeV gamma ray in 100 atm Ar is ~277.4 meters. Therefore, although there are many radioisotopes that emit gamma rays readily, the long range in matter makes their use in nuclear battery technology non-ideal because the systems would be large and would have very low power density.

2.7 Scale Length Matching

As discussed in prior sections, each type of radiation has a characteristic transport scale length in matter (i.e., the range). In designing a microscale energy conversion system based on radiation, the transport scale length of the radiation must be matched to the scale length of the transducer, specifically the region in the transducer where energy deposition contributes to usable energy production. Scale length matching directly impacts the efficiency of the energy conversion system. In larger systems this is not considered; for example, a nuclear power plant stops fission fragments, beta particles, gamma rays and neutrons within the core to produce heat. RTGs use a solid material to stop the ionizing radiation produced by the alpha decay of Pu-238 and generate heat for a thermoelectric energy conversion system. The alphas completely stop in the solid and the energy released turns into heat.

One class of miniature nuclear batteries in the literature operates by creating electron-hole pairs (Branch 2, 4 & 5 of Figure 1). To take advantage of the deposited energy, the range of the specific radiation used in the battery (alpha and beta) should equal the scale length of the transducer, but there are several issues that complicate this. Radiation is emitted isotropically (of equal probability at any angle) as seen in Figure 20. When an isotropic source is interfaced to a transducer which is geometrically incompatible with the isotropic emitter, then the efficiency of battery will be diminished. For a radiation point source on a planar transducer surface, half of the radiation is emitted in the wrong direction. Furthermore, the angles at which the radiation particle trajectories intersect with the plane varies widely. Thus, the distance that each particle has to travel before intersecting the energy conversion region of the transducer varies widely.

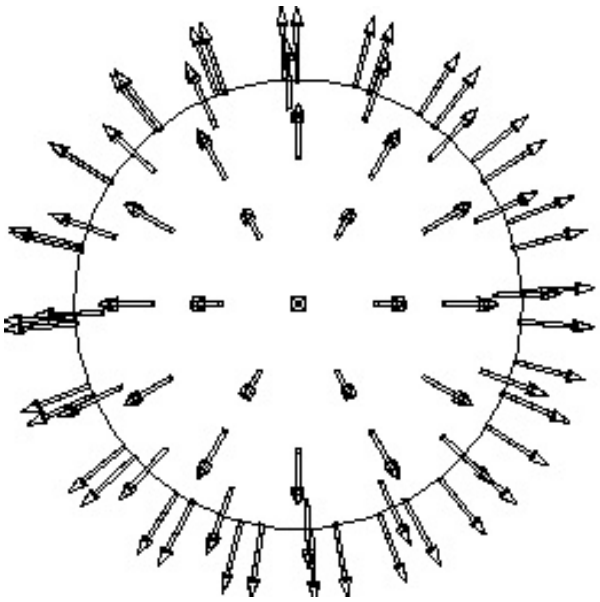

Figure 20. Illustration of a radiation source. The emission is isotropic.

Depending on the type of radiation source, the interactions are complex. If the radiation source is an alpha particle, then the alpha interacts with the electron cloud in the matter through Coulomb interactions. The alpha particle kicks an energetic electron from its bound state and the energetic electron goes on to create further ionization and excitation (Figure 21). The range of the secondary electron defines how far from the track of the alpha particle ionization can take place. The range of the electron created in the secondary reaction further enhances ionization beyond the alpha particle track as does the electron from the tertiary electron and higher order reactions (Figure 22). As discussed in detail in section 1.3, ionization occurs beyond the line of trajectory of the alpha particle as illustrated in Figure 22. So, there will a zone around the path of the alpha particle in which ion pairs are formed. In high density materials such as a solid or a high pressure gas, the effective radius (R_{eff}) of this zone will be small.

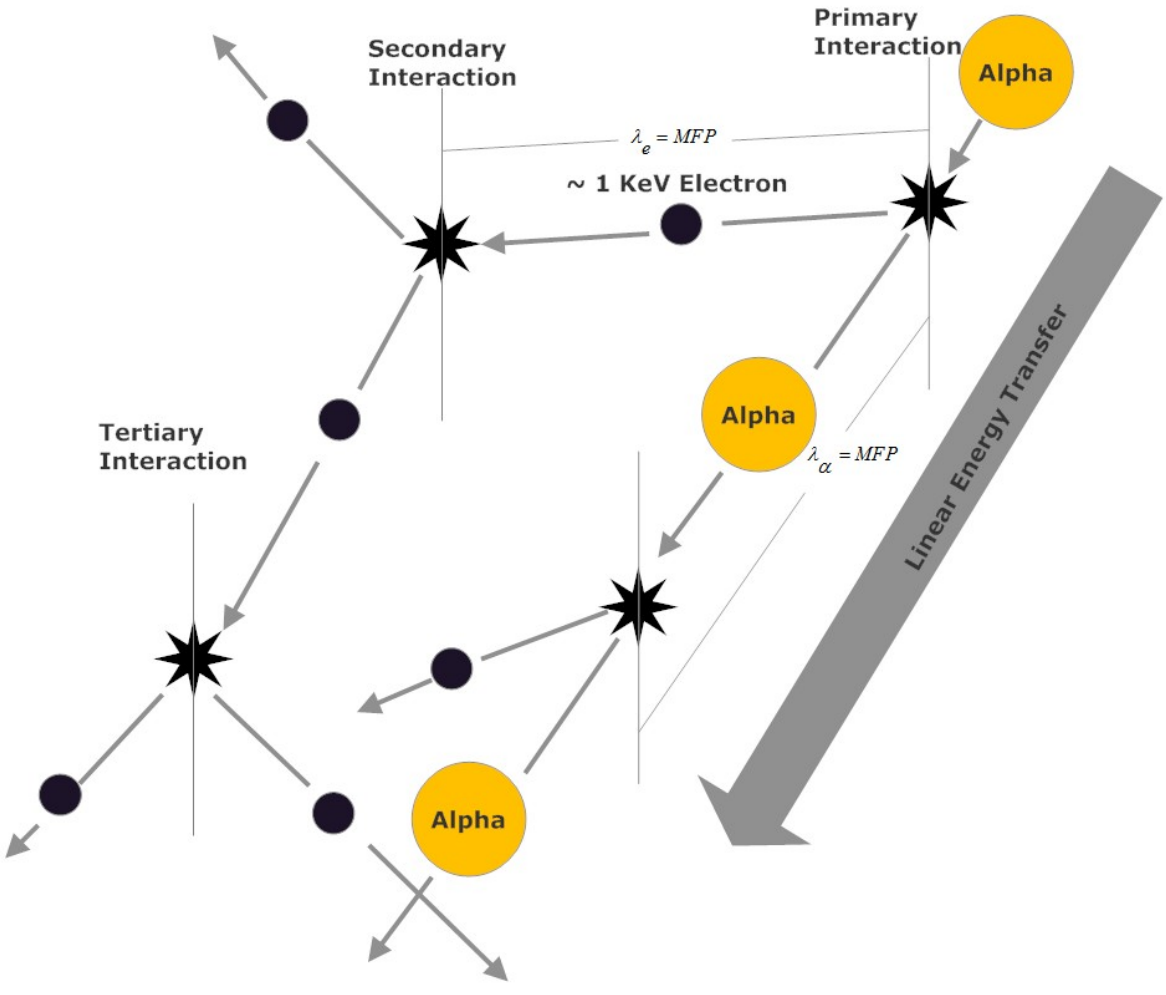

Figure 21. Illustration of an alpha particle interacting with matter. The alpha particle has a linear trajectory through matter and loses energy through Coulomb collisions with electrons in the

cloud. These electrons are energetic and can undergo secondary, tertiary and high order interactions as they lose energy.

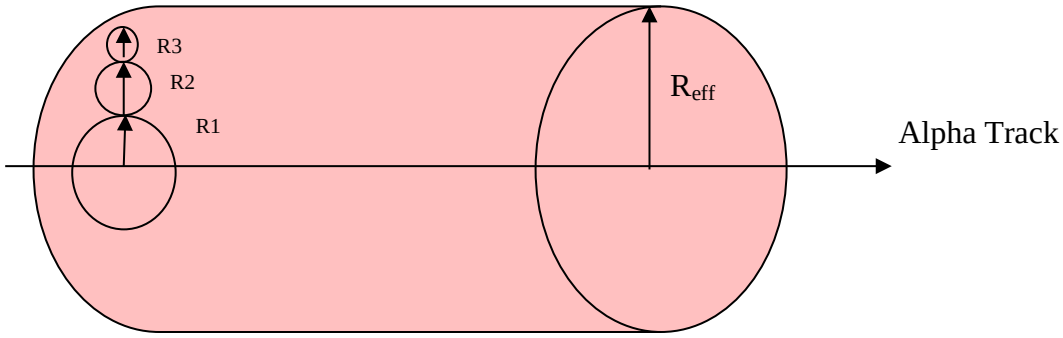

Figure 22. Energy deposition along and radially from the track of an alpha particle is illustrated. The energy of the primary electron is higher than that of the secondary which is higher than that of the tertiary, etc., thus R1>R2>R3>R4 etc. Ionization takes place in a cylinder surrounding the alpha particle path with an effective radius of R_{eff}.

Energetic electrons also interact by Coulomb interactions with the electron cloud of the matter that it passes through as previously discussed in section 2.4. Thus electrons will undergo primary interactions that kick out an electron from the electron cloud (Figure 23). The incoming electron can lose part or all of its energy to the target electron because they have equal mass. The primary electron will in turn travel about one mean free path and then interact with the electron cloud to kick out secondary electrons and so forth.

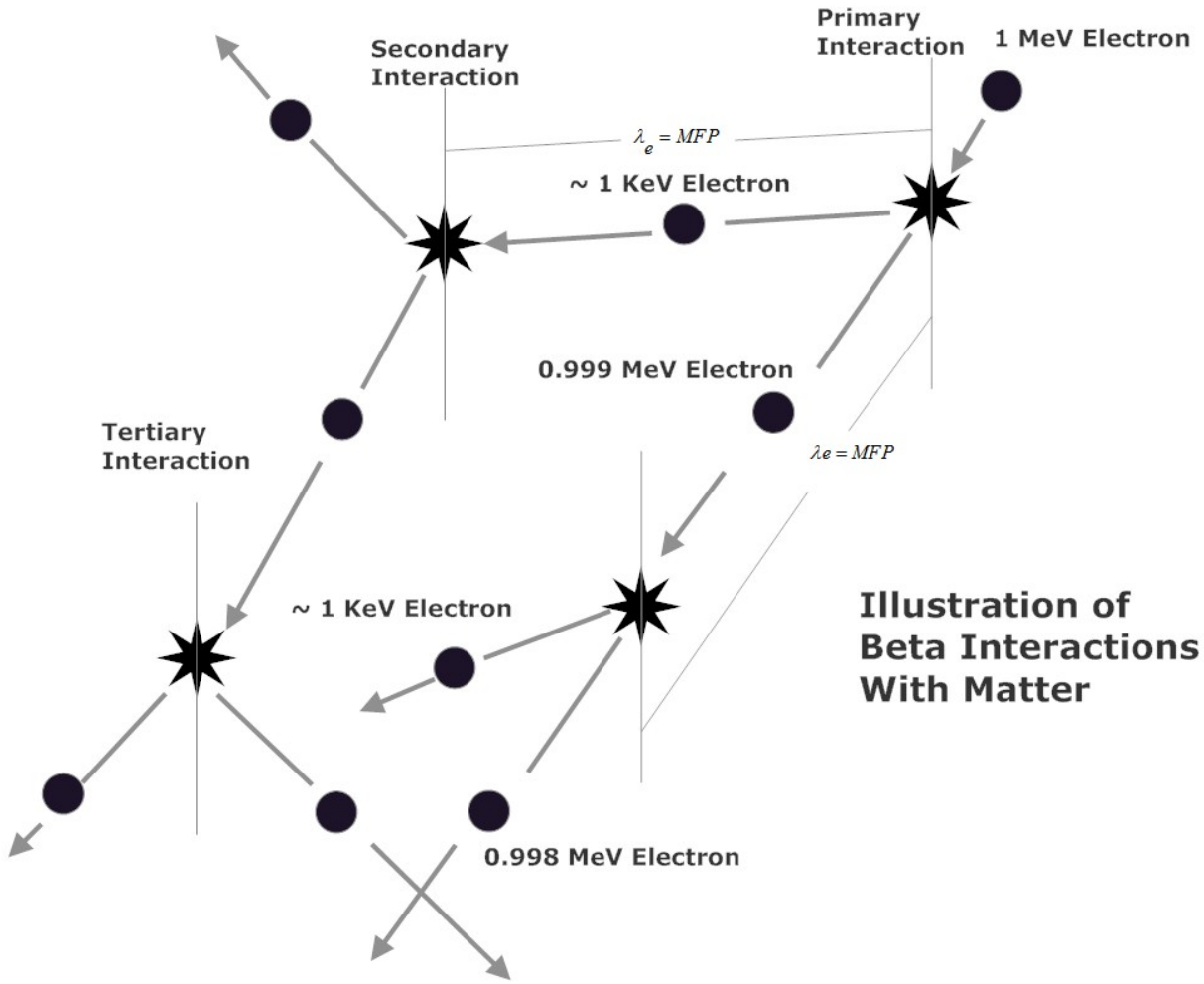

Figure 23. Illustration of a beta particle interacting with matter. The beta particle primarily loses energy through Coulombic collisions with electrons in the cloud. These electrons are energetic and can undergo secondary, tertiary and high order interactions as they lose energy.

As discussed in § 2.6, gamma rays will interact with the material via the photoelectric effect, Compton scattering, or pair production to eject electrons from the electron cloud (Figure 24) and this electron in turn will create secondary electrons which then create tertiary reactions and so forth.

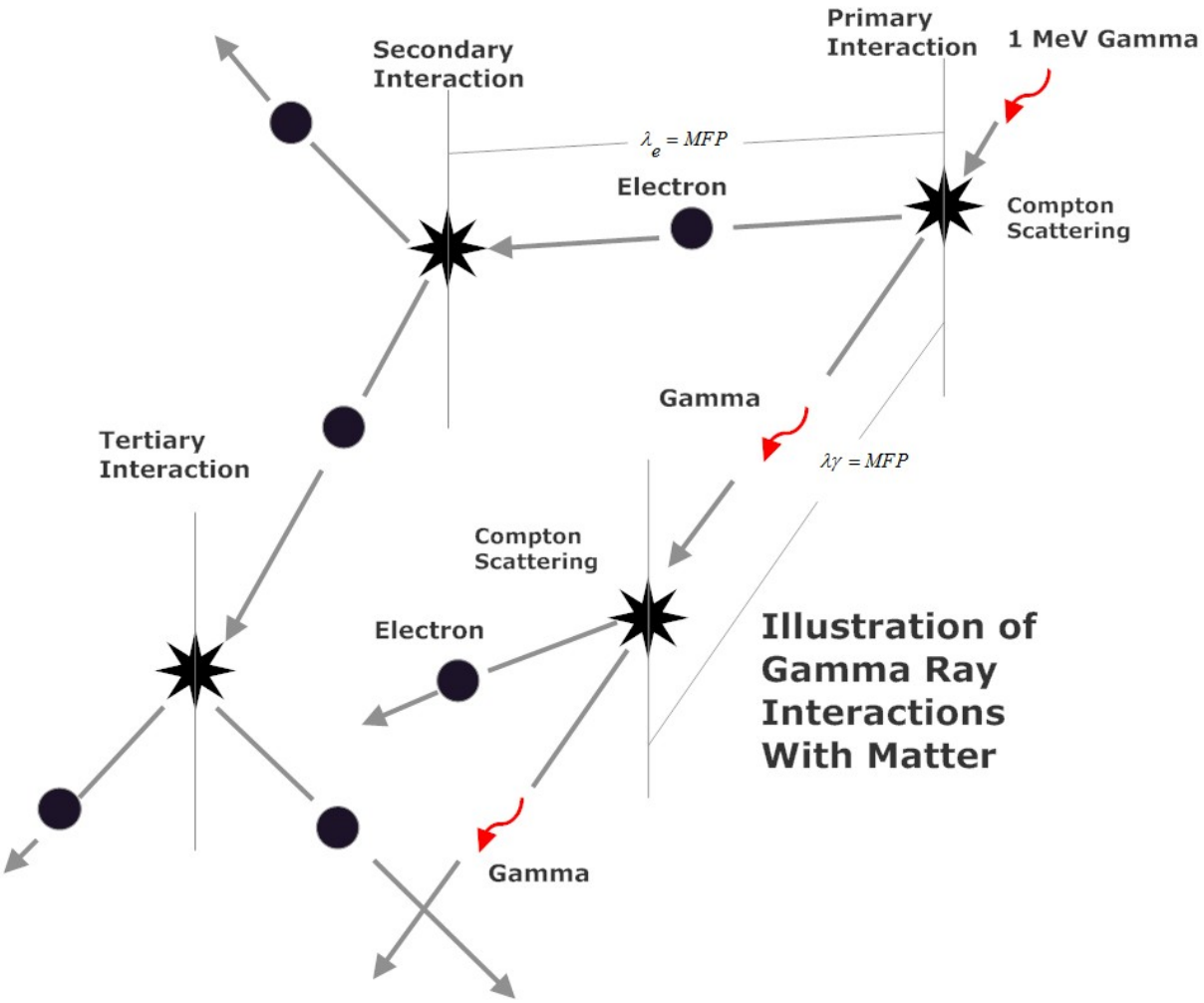

Figure 24. Illustration of a gamma ray interacting with matter. The gamma ray primarily loses energy through the Lorentz force with electrons in the cloud. These electrons are energetic and can undergo secondary, tertiary and higher order interactions as they lose energy.

Fast neutrons which create ionization through recoil reactions, also create primary, secondary, tertiary and higher order electrons (Figure 25) as discussed in section 2.5. The interaction commonalities between the various types of ionizing radiation leads to an interesting phenomena, the W values (the energy, measured in electron volts, required to produce one ion pair) for each type of ionizing radiation with a specific form of matter is similar but the interaction scale lengths differ.

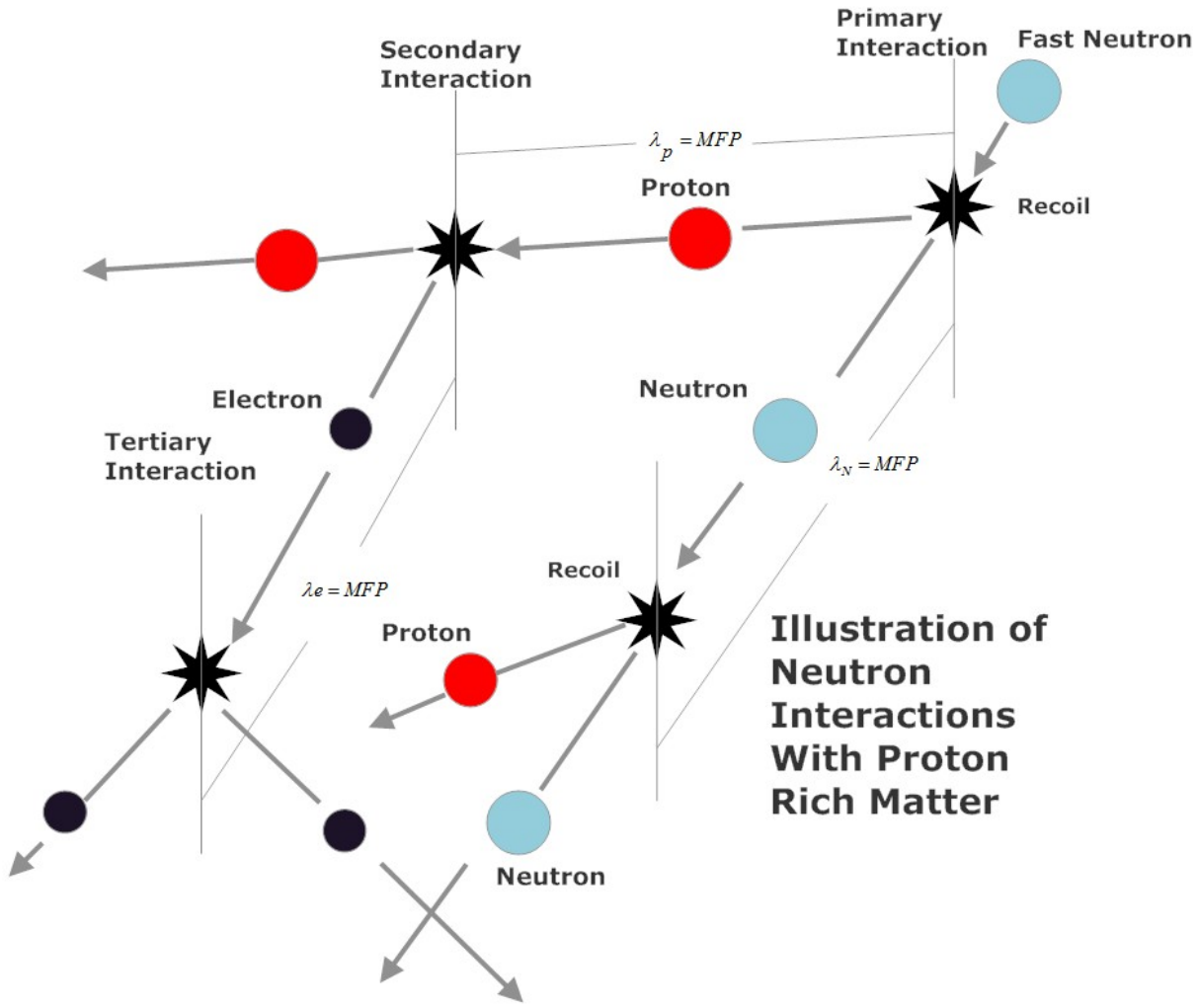

Figure 25. Illustration of fast neutron interactions with a proton rich form of matter. The neutron undergoes an elastic collision with a proton in the target material. The proton recoils and then interacts with the electron cloud, much like the reaction between an alpha particle and matter (Figure 18). The scattered neutron proceeds onward and may have enough energy remaining to undergo another elastic scattering collision with a proton in the material and so forth. On average, a fast neutron will undergo 19 collisions in water before it is thermalized.

The scale length (λ_{Radtr}) varies with the form of the ionizing radiation, the material that it interacts with, and the phase of the matter (Table 8). From Table 8, it is clear that the depletion layer of semiconductor transducers which use a p-n junction are a poor match for the scale length of alpha, beta, gamma, and neutron transport in solids. Further discussion on p-n junction based systems can be found in § 4.1.1.2.1.

Table 8. Scale length of the radiation source (λ_{Radtr}) in various forms of matter.

Radiation	Material	λ_{RadTr} (cm)	Scale-Length of Depletion Layer in SiC p-n junction (cm)
Alpha (5.4 MeV)	1 Atm. Air	4.6	
	SiC	2.0×10^{-3}	$1x10^{-4}$
Beta (2.2 MeV)	1 Atm. Air	834	
	SiC	3.0×10^{-1}	$1x10^{-4}$
Gamma (0.6 MeV)	100 Atm. Ar	2.77×10^{5}	
	SiC	~21.52	$1x10^{-4}$
Neutron (2.45 MeV)	100 Atm. Helium	3×10^{4}	
	Paraffin	~50	$1x10^{-4}$

2.8 Energy Deposition

The formation of secondary, tertiary, quaternary, etc. electrons from the primary event drives the process of ion pair production in radiation interaction with matter [23]. These higher order interactions makes it extremely difficult to model electron-hole pair or ion pair production using available transport codes like MCNP, GEANT4, etc. These transport models are capable of producing results on the energy deposited in a material as the photon, electron or ion passes through the material. With the knowledge of energy deposition, it is possible to rely on the use of the W value to find the number of electron-hole pairs or ion pairs produced. W values, which is defined as the average energy required to form an electron-hole pair or an ion pair, are experimentally measured and have been reliably used in designing calibrated nuclear detectors for decades. The W value has been measured for specific gases, gas mixtures and semiconductor materials (Table 9 and Table 10). All forms of ionizing radiation (gamma rays, neutrons, betas, ions, etc.) have similar W values for any given material that they interact with (i.e., the W value for gammas, betas [29], ions [30] and neutrons interacting with helium, for example, will be similar). The first ionization potential for each material is given in Table 9 as well as the ratio of the ionization potential to W-value. Another important point to be made is that the W-value is independent of the distance that the ionizing radiation travels before losing energy. The specific ionization curve for a 5.4 MeV alpha particle in air, for example, is shown in Figure 26.

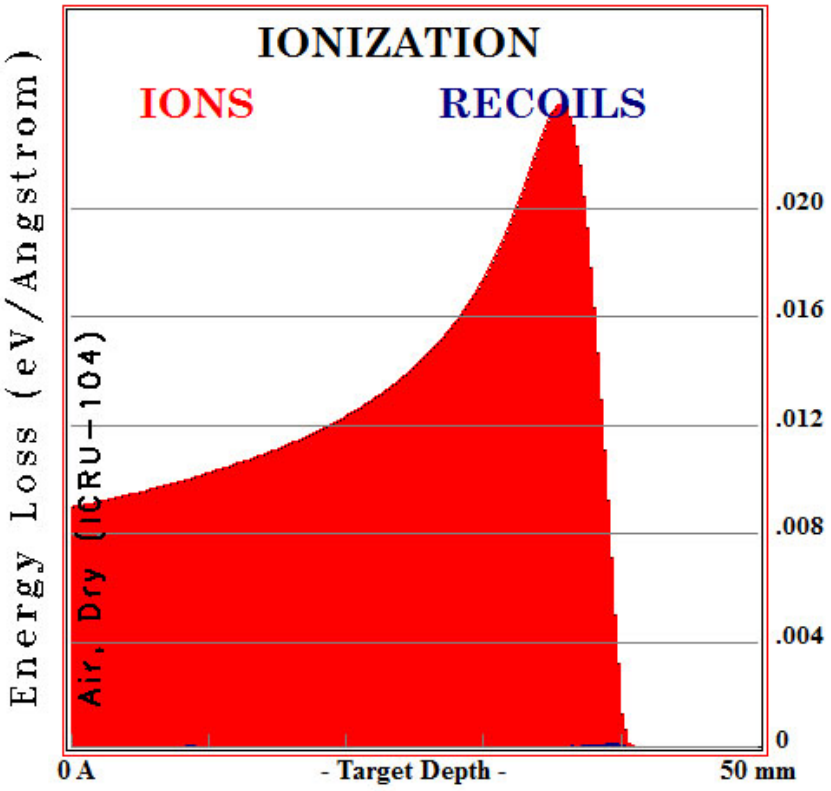

Figure 26. SRIM2011 model showing ionization produced in dry air by 5.4 MeV alpha particle[21].

In addition to forming ion pairs, the alpha particle can lose energy without creating ion pairs, where an electron can receive enough energy by Coulomb interactions to jump to a higher energy state but not sufficiently high to cause ionization. The W-value represents the average energy required to create an ion pair and part of the inefficiency in producing ions is in the production of non-ionized energy states. Non ionizing energy losses go into the creation of excited states and can be accounted for. A rare gas for example has a first electronic state that is a metastable state. This state is typically illustrated with the symbol "*" (e.g. He*). A W*-value is the average energy required to produce a metastable state such as a single He* state in helium gas. For He the W*-value is about 90 eV/He* [31]. In a gaseous system, some of this energy will go into the production of photons through spontaneous emission. Some of the energy ends up as kinetic energy which raises the temperature of the gas. If the photons created in the process are absorbed by the walls of containment or by the gas, then eventually heat is produced.

Table 9. The average energy required to produce ion pairs in various gases [30, 32].

Gas	Energy per Ion Pair, W (eV)	First Ionization Potential (eV)	Fraction of Energy used in Ionization (I/W)
H_2	36.3	15.6	0.43
He (pure)	43	24.5	0.58
N_2	36.5	15.5	0.42
O_2	32.5	12.5	0.38
Air	35.0		
Ne (pure)	36.8	21.5	0.58
Ar	26.4	15.7	0.59
Kr	24.1	13.9	0.58
Xe	21.9	12.1	0.55
CH_4	30	14.5	0.48
C_2H_4	29	10.5	0.36
CO	34	14.3	0.42
CO_2	34		
CS_2	26	10.4	0.40
NH_3	39	10.8	0.28

In the case of radiation interactions with a solid, electron-hole pairs are created as well as heat. The fraction of energy that goes into electron-hole formation depends on the W value and the band-gap energy of the material. In Table 10 some common semiconductor materials are shown along with their relevant properties. As above, the mean ionization energy required to form one electron-hole pair in a solid is the W-value. The ratio of the band-gap energy (E_g) to the W value is the effective efficiency for producing electron-hole pairs through the interaction of radiation with matter. As can be seen in the last column of Table 10, the electron-hole pair production efficiency has considerable variation from one material to another. Diamond has the highest at 0.442. Thus when ionizing radiation interacts with diamond, 44.2% of the energy goes into electron-hole pair production. 55.8% goes of the energy essentially goes into heat production. If nothing is done to use the electron-hole pairs that are being produced, they will recombine and the energy eventually is transformed into heat by a series of processes.

Table 10. Properties for some common semiconductor materials which are useful for direct nuclear energy conversion [33]

Material	Minimum band-gap (E_g) [eV]	Electron drift mobility (μ) [cm²/V-s]	Fano factor (F)	Density (ρ) [g/cm³]	Atomic mass [g/mole]	Molar density [moles/ cm³]	Displacement energy (E_d) [eV]	Mean ionization energy (W) [eV]	Eg/W
Silicon	1.12	1450	0.115	2.329	28.1	0.0829	~19	3.63	0.308
Germanium	0.68	3900	0.13	5.323	72.6	0.0733	30	2.96	0.23
Gallium arsenide	1.42	8500	0.1	5.317	144.6	0.0368	10	4.13	0.344
Silicon carbide	2.9	400	0.09	3.22	40.1	0.0803	28	6.88	0.421
Gallium nitride	3.39	1000	------	6.15	83.7	0.0735	24	8.9	0.381
Diamond	5.48	1800	0.08	3.515	12	0.293	43	12.4	0.442

2.9 Spatial Energy Distribution

In a three dimensional object being exposed to ionizing radiation, the spatial energy deposition distribution is complicated. The problem was described by Chung and Prelas for heavy charged particles irradiating gases in a cylindrical configuration [34]. The energy lost from heavy charged particle interaction with the target gas was calculated as an energy current $\vec{J}(E)$ since primary ionization, which contributes to the energy lost by the heavy charged particle, also deposits energy around the interaction point by secondary and higher-order interactions which occur near the primary interaction point (Figure 22). Chung and Prelas approximated the spatial energy deposition by Equation 24, where $P_d(z)$ is the power density and ∇_r is the gradient in polar coordinates.

$$P_d(z) = \nabla_r \vec{J}(E) \qquad \text{Equation 24}$$

In using this approximation, they assumed that the effective radius (R_{eff}), over which the energy was deposited through primary, secondary, tertiary and higher order reactions, was small. This assumption is accurate for gas pressures above one atmosphere (Figure 27) and is a very good approximation for solids. Some Monte Carlo programs, like MCNPX and GEANT4, follow primary and higher order interactions of particles with a target material and provide data for energy deposited at specific locations in the geometry. These programs do not model the motion of the ions and electrons in the media (due to diffusion and drift velocities in an electric field). Thus it is difficult to accurately obtain a spatial and temporal distribution of ions and electrons. However, if the density of the material is high enough, such as gas pressures above 1 atmosphere or in solids, then the power density generated by Monte Carlo based codes, such as MCNPX or GEANT4, will be sufficiently accurate for most applications. It is feasible but complicated to couple ion and electron motion in a media with Monte Carlo transport codes by developing customized modules.

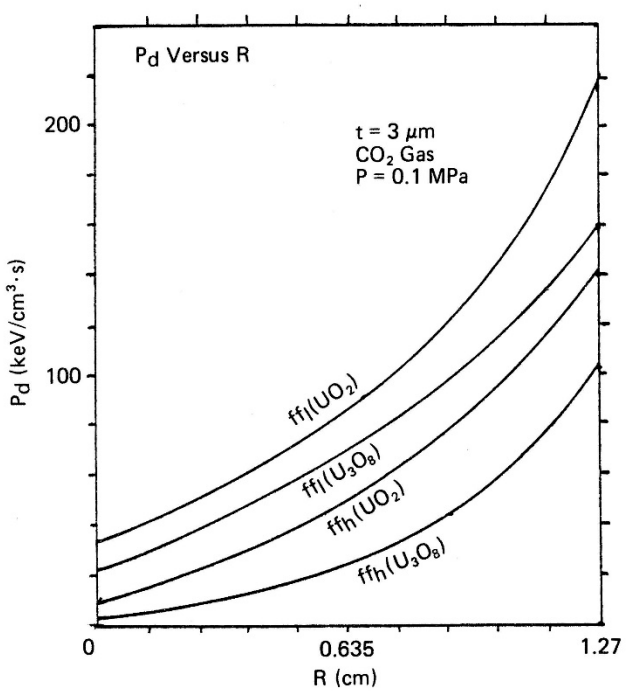

Figure 27. Power deposition (keV/cm^3-s) in a one inch diameter cylinder (with the center being R=0) filled with 0.1 MPa of CO_2 gas and the inner radius lined with a 3 μm coating of UO_2 or U_3O_8. The energy deposition contribution from the light fission fragment (ff_l) and the heavy fission fragment (ff_h) are plotted [34].

3 Choice of Isotopes for Nuclear Batteries

The decision of which isotope to use in a nuclear battery is complex. First of all the type of radiation that the isotope emits will determine whether or not there is a good match between the range of radiation and the scale length of the transducer. Second, the half-life of the isotope determines the activity of the source as well as the effective lifetime of nuclear battery, provided no radiation damage issues exist within the device. The third consideration is the decay energy of the radiation, which, along with activity, determines the effective power density of the source (Tables 3 and 4). The fourth consideration is how the isotope is produced, which effectively determines its cost (see last column of Tables 3 and 4). If the isotope is produced naturally as part of the decay chain of U-238, U-235 or Th-232, then it may be economical if large quantities are not needed. If the isotope is a fission byproduct then it can be recovered from spent nuclear fuel and that may be economical depending on the amount needed. If the isotope must be produced by accelerators or through neutron capture, it will be relatively expensive. The fifth consideration is whether or not there are other radiation forms being emitted by the isotope (e.g., gamma rays). Gamma rays are highly penetrating and thus require shielding to protect humans and electronics. Nuclear battery applications which are intended to be portable would be compromised by bulky shielding.

The production method of an isotope and the existing inventory are important factors in the economics of the device. Krypton-85, for example, is well studied because it is produced by fission of U-235 (yield 0.2717%) and Pu-239 and is released from spent nuclear fuel. The world-wide inventory of Kr-85 was recently reported as being approximately 5250 Peta Becquerel or 1.418×10^8 Ci [35]. This is ~294,000 grams of Kr 85 (Table 11).

Table 11. Estimated world supply of medium half-life (less than 100 yr) isotopes produced in fission.

Isotope	Atomic Mass of Isotope	Half Life (yr)	Activity of World Supply of Isotope (Ci)	World Supply of Isotope (gm)
Eu155	155	4.76	1.18E+08	1.97E+05
Kr85	85	10.76	1.42E+08	2.94E+05
Cd113m	113	14.1	3.97E+05	1.43E+03
Sr90	90	28.9	1.09E+09	6.43E+06
Cs137	137	30.23	1.47E+09	1.38E+07
Sn121m	121	43.9	7.97E+03	9.60E+01
Sm151	151	96.6	3.85E+07	1.27E+06

Isotopes that occur naturally are widely distributed around the world but there may be extraction difficulties as well as limited amounts. For example the Pb-210 content is about 5 milligrams per tonne of uranium ore. The world's uranium reserve is about 7,900,000 tonnes which yields approximately 40,000 grams of Pb-210 with a total activity of 3,280,000 Ci (Table 12).

Isotopes which require an accelerator for production, such as Gd-148, could yield a few grams per year at most with full time operation [2]. The production rate of other isotopes of interest using nuclear reactors and neutron capture will be relatively low due to low cross sections and limited neutron flux. The National Research Council concluded in its study of potential isotopes for nuclear batteries that the supply of radioisotopes is very limited. Only Pu-238 was deemed viable for NASA missions [2]. Pu-238 is created from the ^{237}Np(n, γ)^{238}Np$\rightarrow$^{238}Pu + β reaction. Neptunium 237 is produced in both commercial and military reactors by reactions with uranium 238 (^{238}U(n,2n)^{237}U $\rightarrow$237Np + β) and uranium 235 (^{235}U (n, γ)^{236}U (n, γ)^{237}U$\rightarrow$237Np + β). The available separated inventory of Pu-238 within the National Laboratories in the United States is about 39 kg and the estimated Np-237 inventory is 300 kg [36]. It is feasible to produce Pu-238 from the separated inventory of Np-237 using high neutron flux reactors such as the Advanced Test Reactor at Idaho National Laboratory or the High Flux Isotope Reactor at Oak Ridge National Laboratory [2, 37] to produce about 5 kg of Pu-238 per year. The cost of building the production capability is estimated to be 77 million dollars US [2, 36]. The cost of Pu-238 per kg is about 8 million dollars US. The inventory of unseparated Np-237 worldwide from commercial reactor spent fuel is estimated to be 54,000 kg and from military reactors 1,655 kg [38].

Table 12. The world supply of naturally occurring isotopes from the U238 and U235 decay Assumes world uranium reserves of about 7,900,000 tonnes and world thorium reserves of 5,385,000 tonnes.

Naturally Occurring Isotope	Half Life (yr)	World Supply (gm)	Total Activity Ci
U-238	4.47E+09	7.91E+12	3.28E+06
Th-234	6.60E-02	1.17E+02	3.28E+06
Pa-234m	2.38E-07	4.20E-04	3.27E+06
U-234	2.45E+05	4.33E+08	3.28E+06
Th-230	7.70E+04	1.36E+08	3.28E+06
Ra-226	1.60E+03	2.83E+06	3.28E+06
Rn-222	1.05E-02	1.86E+01	3.28E+06
Po-218	5.80E-06	1.03E-02	3.28E+06
Pb-214	5.10E-05	9.03E-02	3.28E+06
Bi-214	3.79E-05	6.71E-02	3.28E+06
Po-214	5.21E-12	9.23E-09	3.28E+06
Pb-210	2.26E+01	4.00E+04	3.28E+06
Bi-210	1.84E-12	3.26E-09	3.28E+06
Po-210	3.79E-01	6.71E+02	3.28E+06
At-218	6.34E-08	1.12E-04	3.28E+06
Pa-234	7.65E-04	4.47E-03	1.08E+04
U-235	7.03E+08	1.43E+07	3.76E+01
Th-231	2.91E-03	5.91E-05	3.76E+01
Pa-231	3.28E+04	6.65E+02	3.76E+01

Ac-227	2.18E+01	4.42E-01	3.76E+01
Th-227	5.10E-02	1.02E-03	3.71E+01
Ra-223	3.10E-02	6.29E-04	3.76E+01
Rn-219	1.26E-07	2.55E-09	3.76E+01
Po-215	5.64E-11	1.14E-12	3.76E+01
Pb-211	6.87E-05	1.39E-06	3.76E+01
Bi-211	4.07E-06	8.26E-08	3.76E+01
Tl-207	9.08E-06	1.84E-07	3.75E+01
Po-211	1.64E-08	9.29E-13	1.05E-01
Fr-223	4.15E-05	1.16E-08	5.19E-01
Th-232	1.41E+10	5.39E+12	7.28E+05
Ra-228	5.75	2.20E+03	7.28E+05
Ac-228	0.00071347	2.73E-01	7.28E+05
Th-228	1.9116	7.33E+02	7.28E+05
Ra-224	0.018169589	6.96E+00	7.28E+05
Rn-220	1.76306E-06	6.76E-04	7.28E+05
Po-216	4.59792E-09	1.76E-06	7.28E+05
Pb-212	0.001214612	4.66E-01	7.28E+05
Bi-212	0.000114992	4.41E-02	7.28E+05
Po-212	9.48123E-15	2.33E-12	4.66E+05

4 Energy conversion mechanisms

Table 9 and Table 10 are useful in evaluating various isotopes for nuclear battery use. The theoretical limitation for any energy conversion device which uses radiation to produce ion pairs as a first step and then uses the ion pairs for energy conversion is going to be the ratio of the ionization potential divided by the W value (I/W or E_g/W). Thus the last columns of Table 9 and 10 represents the efficiency of converting the energy from radiation into ion pairs in these specific materials. This also represents the theoretical maximum efficiency for any energy conversion process that depends on the production of ion pairs from radiation interactions with a gas or solid. Even though this table was developed for alpha particle interactions with the gases, the W value is consistent for any ionizing radiation as previously discussed (heavy ions, light ions, beta particles, gamma rays and neutrons).

4.1 Scale Length of the Transducer

The transducer which interacts with the radiation will consist of some form of matter (solid, liquid or gas) and will have a size and shape that is characteristic of the energy conversion system. The shape and size of the transducer in recent devices is typically on the scale of

micrometers (e.g., for Schottky barrier betavoltaics, see § 4.1.1.3) or can be on the scale of centimeter (e.g., PIDEC, see § 4.1.6.2.1). The energy conversion mechanism in use will determine the scale length of the transducer. Radiation can be converted to heat or can produce electron-hole pairs (Figure 1). The means of converting radiation to energy can be dependent upon a single cycle or by using the byproduct of one cycle as the feed source for another to form combined cycles (or multi-cycle energy conversion—Figure 28). This section discusses transducer scale length and candidate energy conversion mechanisms for solids, liquids and gases.

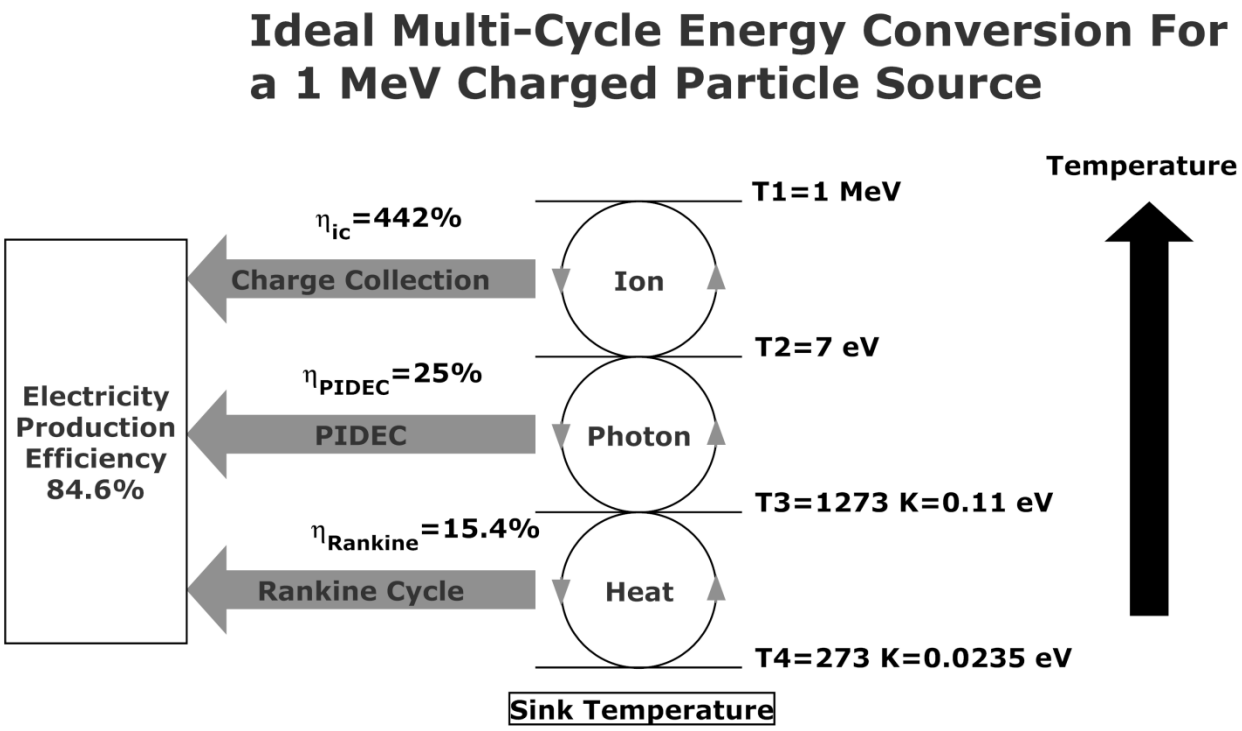

Figure 28. Illustrative example of a multi-cycle energy conversion system where the radiation source starts as a 1 MeV ion which creates electron-hole pairs in a solid. A hypothetical theoretical maximum charge collection device, which approaches Carnot efficiency, produces electricity at an efficiency of 42%. In the second cycle, the remaining energy is in the form of excited states. These excited states produce photons and produces electricity at a theoretical maximum efficiency of 25%. In the third cycle, the remaining energy is in the form of heat and high temperatures. The conversion efficiency of a high temperature Rankine Cycle approaches 50% [39].

4.1.1 Interactions with Solids

The topic of interactions with solids can be complicated by many imagined configurations. However, in the context of nuclear batteries which depend upon p-n junctions, these features will be dominated by metals and semiconductors.

4.1.1.1 Interactions with metallic conductors

In a metal the energy will basically go into heating since the energy differential between the ground state and the conduction band is low. Interactions of radiation with metals do not serve a direct role in nuclear battery technology. Metals can be used as structural components and as conductors (e.g., used to form Schottky barriers or for metallization in semiconductors).

4.1.1.2 Interactions with semiconductors

In a semiconductor the energy will go into electron-hole pair production (about 42% for SiC as shown in Table 10) and heating. Electron-hole pairs represent the most productive route for energy conversion. Thus, methodologies which use electron-hole pairs have a theoretical efficiency limitation based on the ratio of E_g/W (Table 10). The interaction of ionizing radiation with semiconductors is used in alphavoltaics and betavoltaics technology.

4.1.1.2.1 Semiconductor energy conversion based on p-n junction structures

Alphavoltaic and betavoltaic cells are typical of semiconductor based energy conversion. These types of cells have been studied since the 1950's [40, 41]. The ionizing radiation creates electron-hole pairs in a semiconductor. The depletion region, where the p-n junction forms, creates a local potential due to the compensation of the n- and p-type regions, and this potential separates the electrons from the holes. The depletion region is limited in thickness to the micrometer range (~ 1 μm), as will be shown. If the range of the ionizing radiation in the solid is greater than the depletion region, then the fraction of charged pairs produced that the cell can harvest is low. Alpha particles have a range of about 20 micrometers in a solid. The theoretical maximum efficiency of an alphavoltaic cell based on silicon carbide was reported to be about 3% [42]. Likewise, the range of a beta particle in a solid is much higher, thus the corresponding theoretical maximum efficiency of a betavoltic cell is around 1% [22].

If the depletion layer can be extended beyond the one micrometer range, then the achievable efficiency can be increased [26]. In this reference, tables are generated for the energy transport efficiency (η_d) as a function of distance from the source for idealized geometries in SiC (mono directional beam on a slab or a point source in a sphere—this is an intentional overestimation of transport efficiency since these idealized geometries represent the most efficient means to transport radiation to the depletion layer and all other designs will be less efficient: ergo, this is a theoretical maximum). The transport efficiency is maximized by choosing the thickness of the depletion layer and locating it at the peak of the energy deposition curve (see Table 13) for an alpha particle, the tables are lengthy for beta particles and are not presented here but the reader is referred to reference [22]. In several references [22, 26, 42] the depletion layer was chosen as 1

μm because the impurity level in a high a quality SiC wafer is typically on the order of $1x10^{16}$ atoms/cc. To broaden the depletion layer beyond 1 μm, as will be discussed, the dopant densities should be less than $1x10^{16}$ atoms/cm^3. However, the ability to reduce impurity densities below $1x10^{16}$ atoms/cm^3 is a technological challenge. One can compensate for high intrinsic donor or acceptor impurity levels in the wafer by counter-doping with acceptor or donor impurities respectively to try to reduce dopant densities below $1x10^{16}$ atoms/cm^3 but higher impurity density resulting from counter-doping will result in shorter carrier lifetimes and a reduction in the efficiency of the cell.

Table 13. GEANT4 and SRIM/TRIM Calculations for Predicting Energy Deposition in a Depletion Region of 1 μm Thick for the Slab and Sphere Models for a 5.307 MeV (e.g., Po-210) alpha beam or point source respectively.

Range (μm)	GEANT4						SRIM/TRIM	
	Sphere			Slab			Slab	
	Energy (keV)	% deposited	σ (%)	Energy (keV)	% deposited	σ (%)	Energy (keV)	% deposited
0-1	208	3.92	0.006	208	3.92	0.006	211	3.98
1-2	214	4.03	0.006	214	4.03	0.007	218	4.11
2-3	220	4.15	0.006	220	4.15	0.007	223	4.19
3-4	228	4.29	0.006	228	4.29	0.007	226	4.26
4-5	236	4.44	0.006	236	4.45	0.007	235	4.42
5-6	245	4.61	0.006	245	4.61	0.007	243	4.59
6-7	254	4.79	0.006	254	4.79	0.007	258	4.85
7-8	265	5.00	0.006	266	5.00	0.007	269	5.06
8-9	279	5.25	0.006	279	5.25	0.007	279	5.25
9-10	294	5.55	0.006	294	5.55	0.007	296	5.58
10-11	312	5.89	0.006	313	5.89	0.007	315	5.94
11-12	335	6.32	0.006	335	6.32	0.006	337	6.35
12-13	364	6.86	0.005	364	6.86	0.006	365	6.88
13-14	402	7.58	0.006	402	7.58	0.006	405	7.62
14-15	456	8.60	0.006	457	8.61	0.006	454	8.56
15-16	527	9.93	0.006	527	9.94	0.006	508	9.57
16-17	408	7.68	0.017	407	7.66	0.017	382	7.19
17-18	59	1.12	0.118	58	1.09	0.121	0	0.00
18-19	0	0.00	-	0	0.00	-	0	0.00
19-20	0	0.00	-	0	0.00	-	0	0.00
TOTAL	5307	100.00	-	5307	100.00	-	5220	98.40

The major problem with a p-n diode is that the n- and p-type impurities in the depletion region are displaced and the structure becomes more random due to ionizing radiation. Thus the cell ceases to function as a p-n junction relatively quickly. The lifetime of a typical p-n junction beta or alpha voltaic cell is short and even at low dose rates. At high dose rates the cell's lifetime could be on the order of milliseconds [43]. However, this is not the only problem that p-n diodes have. The other problem is a poor match between the scale length of the radiation and the transducer.

The ranges of beta particles do not match well with the depletion widths of p-n diodes except at very low beta energies. Table 14 shows the energy deposition characteristics in SiC, Xe gas and ZnSe for betas from tritium (average energy 5.45 KeV), Ni-63 (average energy 17.20 keV), Sr-90 (average energy 196.03 keV) and Y-90 (average energy 934 keV). As can be seen from the table, 99.95 % of the beta energy is deposited in SiC within 1.71 μm for tritium, 15.7 μm for N-63, 474 μm for Sr-90 and 2873 μm for Y-90. This data shows that the scale length match for a depletion width of the order of 1 μm is good for tritium but gets much worse as the beta energy increases.

Table 14. Energy Deposition Characteristics of the Beta Particles Emitted by Four Radioisotopes In Various Materials. E_exp is the expected beta particle energy calculated using the spectral energy distribution[Ref# which contains spectrum]. E_tot,M is the average beta energy deposited in a sample (where L_trans >> λ_RadTr) as calculated by MCNPX. The % difference between the two methods is shown in column 5. The last four columns describe the depth at which 25%, 50%, 75% and 99.95% of E_tot,M is deposited for the various beta emitters and materials.

Target Material	Isotope	E_{exp} (keV)	$E_{tot,M}$ (keV)	% Diff	Depth (in μm) of % $E_{tot,M}$ Deposition			
					25%	50%	75%	99.95%
SiC	H-3	5.45	4.32	20.8	< 0.1	0.128	0.292	1.71
	Ni-63	17.20	14.08	18.2	< 1	0.968	2.47	15.7
	Sr-90	196.03	159.12	18.8	16.9	49.0	107.7	474
	Y-90	934.40	772.79	17.3	136	366	756	2873
Xe	H-3	5.45	3.72	31.7	29.7	83.7	190	1179
	Ni-63	17.20	11.95	30.6	181	548	1329	8929
	Sr-90	196.03	133.46	31.9	8170	22880	49909	247437
	Y-90	934.40	655.57	29.8	64838	169497	348379	1148492
ZnS	H-3	5.45	4.01	26.4	< 0.1	0.0987	0.2361	1.3941
	Ni-63	17.20	13.04	24.2	< 1	< 1	1.84	12.5
	Sr-90	196.03	101.62	48.2	10.9	31.5	70.5	344
	Y-90	934.40	476.51	49.0	86.97	236.4	498.9	2119

Large ions such as fission fragments have a range on the order of 5 μm, and this range when compared to the 1 μm depletion region is much better match of scale lengths than that for most beta emitters. In this case the theoretical maximum energy conversion can approach 20%. But, the radiation damage to the junction will be even more rapid with these larger fragments of higher energy because of large dose rates.

4.1.1.2.2 Efficiency of a Beta or Alpha Voltaic Cell Based on a Classic P-N Junction

A junction is formed between n- and p-type semiconductor materials. At the junction's interface, the diffusion of charge carriers across the junction sets up a space charge which in turn sets up an electrical potential and electrical field (Figure 29). The depletion region thus has an electrical field which separates electron-hole pairs when they are created by the interaction of radiation with the material. Outside of the depletion region, electron-hole pairs which are created by the interaction of radiation with matter do not have electrical fields to cause their separation. The most likely fate of the charge carriers beyond the depletion region is that they will instead recombine or become trapped by defects. Some of the charge carriers may drift into the depletion region and become part of the cell current driven by the junction's electric field.

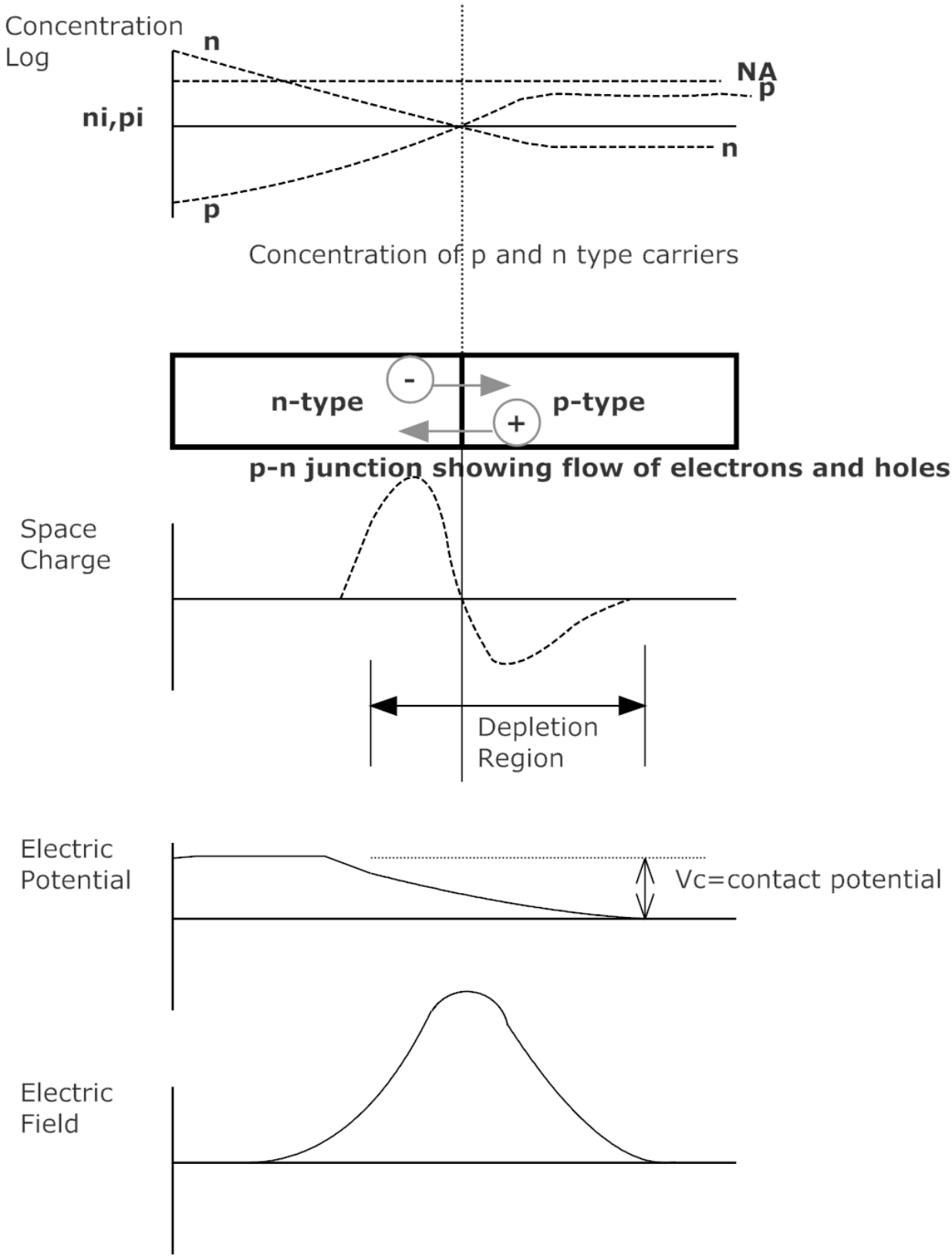
Concentration
Log
n
NA
p
ni,pi
n
p
Concentration of p and n type carriers
n-type
p-type
-
+
p-n junction showing flow of electrons and holes
Space
Charge
Depletion
Region
Electric
Potential
Vc=contact potential
Electric
Field

Figure 29. Illustration of a p-n junction showing (from top to bottom): concentration profiles of n and p type materials; junction interface with charge carriers compensation; diffusion of charge carriers across the junction to produce space charge; the electrical potential; and electric field.

Once an electrical field is in place, a driving potential for current flow exists within the cell. The absolute efficiency (η_{ab}) of an energy conversion device is always defined as shown in Equation), where P_{out} is the output power from the energy conversion device calculated by Equation , P_{total} is the total power deposited in the energy-transducing regions of the device, and P_{rad} is the total radioisotope power incident on the cell; P_{total} can be calculated from Equation .

$$\eta_{ab} = \frac{P_{out}}{P_{total}} \quad \text{Equation 25}$$

$$P_{out}(W) = V(Volts) \cdot I(A) \quad \text{Equation 26}$$

where V is cell potential in volts and I is the cell current in Amps.

$$P_{total}(W) = A\,(Bq) \cdot E_{dis}(eV \cdot Bq^{-1}) \cdot 1.6 \times 10^{-19}\,(J/eV) \quad \text{Equation 27}$$

where A is radioactive source activity, E_{dis} is the energy of the particle produced by the decay of the source.

To estimate the cell current I, one can find the maximum current that can be created in the cell by the interaction of radiation with matter. The maximum current will be dependent on the energy transport efficiency of the radiation (beta or alpha) to the depletion zone. This can be expressed in a term which represents the fraction of power that is deposited in the depletion zone and is a factor called η_d (Equation 28). This is typically calculated by using Monte Carlo based transport Codes.

$$\text{Power absorbed in depletion zone} = P_{dpl} = P_{total} \cdot \eta_d \quad \text{Equation 28}$$

The maximum rate of charge production in the depletion zone is then considered through the examination of the number of electron-hole pairs that are created per second in the depletion zone. As discussed previously, Monte Carlo radiation transport codes do not have the capability of modeling electron and ion motion in the media. The use of the W (eV/ion pair) value, which is the amount of energy that it takes to make on average an electron hole pairs, is imperative. Monte Carlo codes have the capability of calculating the rate of energy absorbed spatially in a material. But, as previously discussed the spatial and temporal distribution of electrons and ions should be in close proximity to the spatial energy deposition in a solid. Thus a reasonable estimate is to use the spatial rate of energy lost calculated by Monte Carlo Codes to find the power density in the depletion zone and then use the power density distribution to estimate the electron and ion density distribution. Therefore the number of electron-hole pairs created per second (N_e) in the depletion zone is,

$$N_e(\#\ \text{pairs/sec}) = \frac{P_{total}\left(\frac{J}{s}\right)\cdot \eta_d}{W\left(\frac{eV}{\text{ion pair}}\right)} \cdot 6.25 \times 10^{18}\ (\text{eV/J}) \qquad \text{Equation 29}$$

Assuming that the cell has no losses due to traps, the production rate of electron-hole pairs is proportional to the maximum ideal short circuit current (J_{sc}) in the junction. Ideal short circuit current is equal to the production rate of electron-hole pairs multiplied by the charge per electron ($1.6x10^{-19}$ Coulomb):

$$J_{sc} = N_e\left(\frac{\#pairs}{sec}\right)\cdot 1.6 \times 10^{-19}\left(\frac{Coulomb}{pair}\right) \qquad \text{Equation 30}$$

$$J_{sc} = P_{total}\cdot \eta_d\ /W \qquad \text{Equation 31}$$

The power out is related to the open circuit voltage (V_{oc}) multiplied by the short circuit current (J_{sc}) and the Fill Factor (FF). Thus, the maximum power out that a p-n junction is capable of producing is shown in Equation 32 , where P_{max} is the optimized power output of the cell. The FF is typically > 0.7 for high grade solar cells (Equation 33).

$$\begin{aligned} P_{out}(W) &= V_{oc}(V)\cdot J_{sc}(A)\cdot FF \\ &= \frac{V_{oc}\cdot P_{total}\cdot \eta_d \cdot FF}{W} \end{aligned} \qquad \text{Equation 32}$$

$$FF = \frac{P_{max}}{V_{oc}\cdot J_{sc}} \qquad \text{Equation 33}$$

4.1.1.2.3 Open Circuit Voltage (V_{oc}) and the Driving potential efficiency

When electron-hole pairs are created in a solid-state material, any energy transferred to the electron greater than the band-gap energy (E_g) eventually ends up becoming heat. Thus, the process of creating electron-hole pairs has a material dependent efficiency (shown in Table 10). When creating an electron-hole pair, the energy that is expended to create the charge carriers is E_g.(eV) In a beta or alpha voltaic cell, the electron-hole pair is driven by the junction voltage. The maximum voltage is the open circuit voltage V_{oc}. The maximum power produced by the cell is thus the open circuit voltage times the short circuit current, J_{sc}. Current flow I (Coulomb/sec) is electron density ρ_e (electrons/m^3) times charge per electron times the drift velocity u (m/s) times the surface area (A m^2). This is very similar to a photovoltaic solar cell, and therefore, for a nuclear battery the maximum possible current will be equal to the number of electron-hole pairs created in the depletion zone per second, assuming no recombination losses.

Using an alternate definition, one can start with the electron-hole production rate through the interaction of the radiation with matter in Equation 29 to define the short circuit current, as in Equation 30Equation 30, and the maximum power out in Equation 32. The power expended to

create the current flow (P_{ex}) can be defined as the electron flow rate times the energy used to form a single electron-hole pair (e.g., the band gap (E_g) energy),

$$P_{ex}(W) = N_e\left(\frac{pair}{s}\right) \cdot E_g(eV/pair) \cdot 1.6 \times 10^{-19}\ (J/eV) \qquad \text{Equation 34}$$

The concept of the driving potential efficiency (η_{dp}) was introduced by Oh, et al. [42]; it originates from the relationship between the open circuit voltage and the band gap of the cell material. The magnitude of the open circuit voltage is less than or equal to the material band gap. A simple way to consider this relationship is that the cell power output will be less than the power expended in creating the electron-hole pairs. The ratio of the power out and the power expended is the driving potential efficiency shown in Equation 35 and Equation 36. The open circuit voltage can then be represented as the product of the driving potential efficiency and the band gap, shown in Equation 37.

$$\eta_{dp} = \frac{P_{out}}{P_{ex}} = \frac{V_{oc}(V) \cdot \left(\frac{N_e\left(\frac{elec}{s}\right)}{6.25 \times 10^{18} elec/C}\right)}{E_g(eV/pair) \cdot N_e\left(\frac{pair}{s}\right) \cdot 1.6 \times 10^{-19}\ (J/eV)} \qquad \text{Equation 35}$$

$$\eta_{dp} = \frac{V_{oc}}{E_g} \qquad \text{Equation 36}$$

$$V_{oc} = \eta_{dp} \cdot E_g \qquad \text{Equation 37}$$

So, the maximum efficiency can be written in terms of the power out and total power of the emitter and can be calculated from Equation 38; substituting Equation 35 causes this expression to simplify to Equation 39. Similarly, the use of the pair production efficiency η_{pp} discussed by Oh, et al. [42], shown in Equation 40Equation 40, causes Equation 39 to resolve to the convenient form in Equation 40, which agrees with the results in the literature.

$$\eta = P_{out}/P_{total} = V_{oc}(V) \cdot \eta_d \cdot \left(\frac{FF}{W\ (eV/pair)}\right) \quad \text{Equation 38}$$

$$\eta = \eta_{dp} \cdot E_g \cdot \eta_d \cdot \frac{FF}{W\ (eV/pair)} \quad \text{Equation 39}$$

$$\eta_{pp} = \frac{E_g\ (eV)}{W\ (eV/pair)} \quad \text{Equation 40}$$

$$\eta = \eta_{dp} \cdot \eta_d \cdot \eta_{pp} \cdot FF \quad \text{Equation 41}$$

The efficiency calculation requires one more parameter, the open circuit voltage. Using the ideal PV cell-equivalent circuit in Figure 30, the output current for an ideal PV cell is related to the dark saturation current of the p-n junction (I_D) and radiation generated current (I_L) by taking the nodal balance of the circuit in Equation 42.

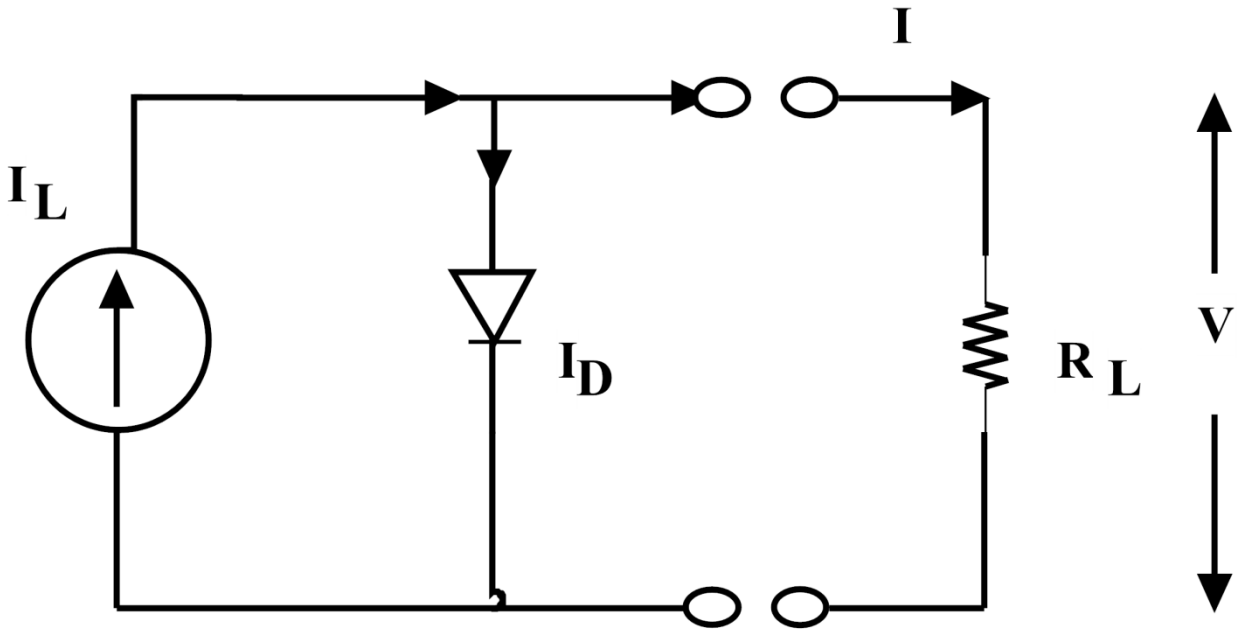

Figure 30. Ideal alpha or beta voltaic cell equivalent circuit.

The open circuit voltage is a function of the dark saturation current (I_0) and the radiation generated current (I_L). The diode current is a function of the dark saturation current in Equation 43Equation 43, where I_0 is the reverse saturation current which is a function of the material and temperature, q is the electron charge (1.602×10^{-19} Coulombs), k is Boltzmann's constant

(1.381×10^{-23} J/K), T is the cell temperature in Kelvin and n is the shape factor (for an ideal cell n=1). The open circuit voltage occurs when the radiation generated current balances the diode current. So setting I=0 and using Equation 43Equation 43 for I_D, one can find the open circuit voltage as shown in Equation 44Equation 44.

$$I = I_L - I_D \qquad \text{Equation 42}$$

$$I_D = I_0\left(e^{\left\{\frac{qV}{nkT}\right\}} - 1\right) \qquad \text{Equation 43}$$

$$V_{oc} = \frac{nkT}{q}\left(\ln\left\{\frac{I_L}{I_0} + 1\right\}\right) \qquad \text{Equation 44}$$

There is also a relationship between band gap energy and open circuit voltage. The dark saturation current I_0 depends on the charge carriers due to the temperature of the cell T. The relationship between the dark saturation current and band-gap E_g is shown in Equation 45.

$$I_0 = D \cdot T^3 \cdot e^{\left(\frac{q \cdot E_g}{n \cdot k \cdot T}\right)} \qquad \text{Equation 45}$$

As the band-gap increases, the dark saturation current will decrease. Thus, open circuit voltage will increase for the ideal cell as band gap energy goes up. The highest open circuit voltage achieved for a wide band-gap cell (e.g., diamond) was 2.6 volts [44] which is equivalent to a driving potential efficiency (η_{dp}) of 0.48.

Depletion Zone Width and Current

The collection probability is the probability that a carrier generated in a cell by the interaction of radiation with matter in a region of the cell will be collected and thereby contribute to the radiation generated current flow (I_L). The carriers generated in the depletion region will have a collection probability of unity because the electron-hole pairs are quickly separated by the electric field and eventually are collected. Outside of the depletion zone, the collection probability decreases because the electron-hole pairs must diffuse into the depletion region. If the distance is more than one diffusion length away from the junction, the collection probability is negligible (Figure 31). For example, the diffusion length in SiC can vary from 0.07 μm to a few μm depending on material defects [45, 46].

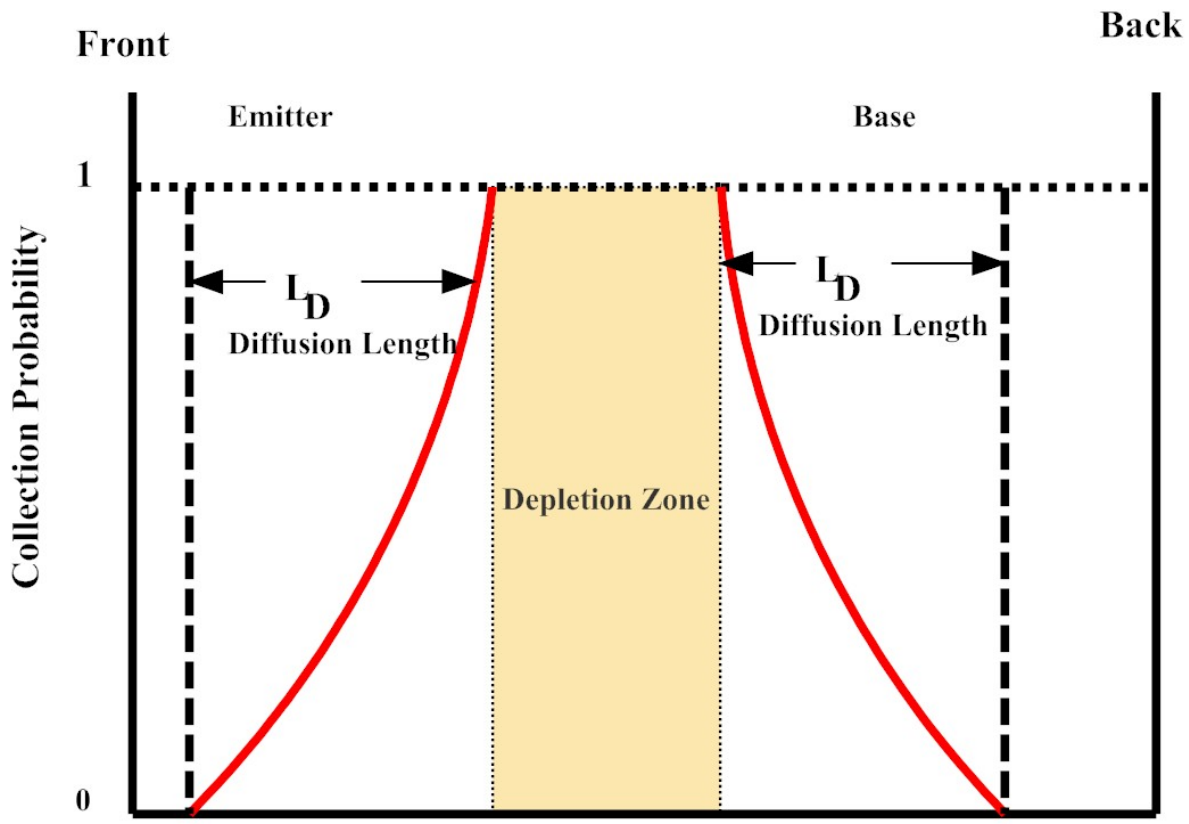

Figure 31. The collection probability for a linearly graded alpha or beta voltaic structure. The collection probability is negligible beyond the diffusion length of carriers.

In the determination of the width of the depletion zone, the conduction of charge carriers is important, but even of more significance is the lifetime of the charge carriers within the semiconducting material from the time of its creation or injection to their subsequent collection by a true conductor, such as copper. The lifetime of charge carriers, electrons and holes, in semiconductors, is governed by the traps that are present within the band structure. The depletion region is limited to very small thicknesses. This means that only the nuclear energy that is deposited within the depletion region has a collection efficiency of unity for power production and thus limits the efficiency of the energy conversion system. Equation 46 through Equation 48Equation 48 below describe this latter property through the intrinsic carrier concentration, n_i, the built-in potential voltage across the depletion region, V_{bi}, and the depletion region width, W [47].

$$n_i = 2\left(\frac{2\pi \cdot k_B T}{h^2}\right)^{3/2} (m_c \cdot m_p)^{3/4} * \mathrm{Exp}\left[-\frac{E_g}{2k_B T}\right] \quad \text{Equation 46}$$

$$V_{bi} = \frac{k_B T}{e} \mathrm{Ln}\left(\frac{N_a \cdot N_d}{n_i^2}\right) \quad \text{Equation 47}$$

$$W = \left\{\frac{2\varepsilon_s \cdot V_{bi}}{e}\left(\frac{N_a + N_d}{N_a \cdot N_d}\right)\right\}^{1/2} \quad \text{Equation 48}$$

In these equations k_B is Boltzmann's constant, T is the temperature of the semiconductor in Kelvin, e is the unit electron charge, ε_s is the permittivity, E_g is the band gap energy, N_a is the relative concentration of vacancies available in the p-type region, N_d is the relative concentration of electrons in the n-type region, and m_p and m_n are the effective masses of the holes and electrons, respectively. As can be seen in these equations the defining variables in determining the built-in potential barrier and the depletion region width is the intrinsic semiconductor properties and the doping concentrations N_a and N_d in the respective p- and n-type regions of the semiconductor, indicating that doping is the primary method to change these properties. Naturally, one could assume that these values can be varied to obtain the desired values, but this is simply not the case. It can be shown that lower doping concentrations produces larger depletion widths but lower built in potentials. In addition, the built in potential approaches zero as the doping concentration product approaches the square of the intrinsic carrier concentration, meaning that no depletion region exists. It also needs to be pointed out that the doping concentration must be greater than the injected charge from the depletion region for the transport of the generated charges to be in the low injection regime and that very low doping concentrations are not controllable in a semiconductor.

Depletion width was calculated for a widely used semiconductor in a nuclear battery research, 4H-SiC. For this semiconductor ε_s is about 10 [48], m_n and m_p were taken to be $1.2m_e$ and $0.76m_e$, respectively, and the band gap is approximately 3.25 eV at room temperature [49]. Using a temperature of 300 ^{o}K in Equation 46 the intrinsic doping concentration for this material was found to be 9.5×10^{-9} cm^{-3}. This data was used with Equation 47, Equation 48, and both N_d and N_a varying between 10^{15} cm^{-3} and 10^{20} cm^{-3} to demonstrate the depletion widths possible within silicon carbide shown in Figure 32. From inspection, it can be seen that the largest depletion region width that can be realized in silicon carbide is 2.6 μm and indicates that the depletion width is the primary limiting factor in any planar single p-n junction-based nuclear battery system. In order to achieve a depletion width of 2.6 μm, the impurity levels have to be on the order of 0.1 ppm. Achieving sub-ppm impurity levels is difficult for SiC. It is more reasonable to obtain impurity levels in the 1 to 10 ppm range and thus achieve a depletion width on the order of 1 μm [Oh et. al.].

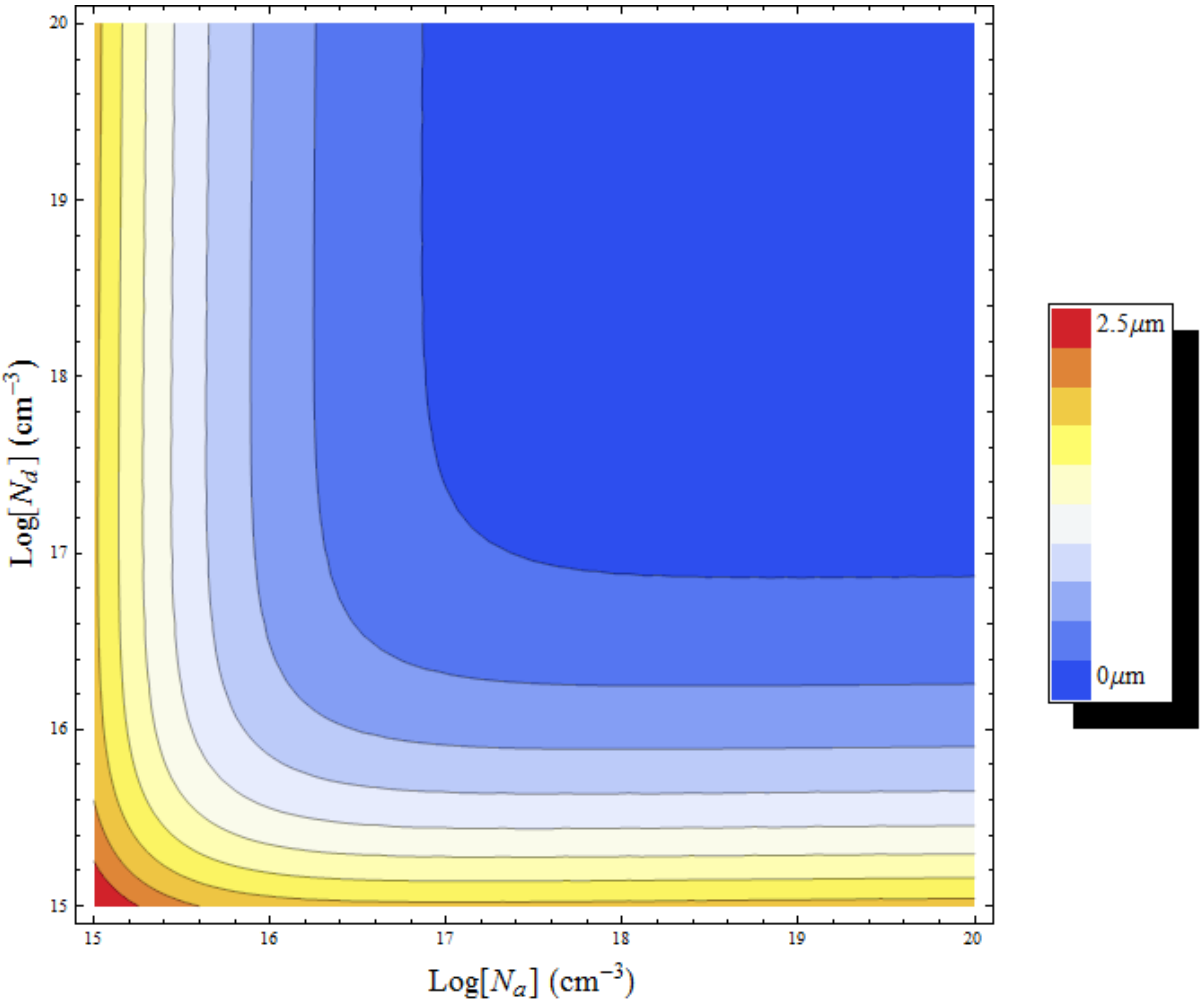

Figure 32. Density plot indicating depletion region width for varying donor and acceptor density concentrations in 4H-SiC.

4.1.1.3 Semiconductor energy conversion based on Schottky barrier diodes

The Schottky barrier is a potential energy barrier between a metal and a semiconductor that forms a diode. It depends on the differential work function between a semiconductor and a metal contact. The surface interface between the metal and semiconductor forms a depletion region that is effectively 100's of nanometers thick. Thus the effective size of the energy conversion region is thin and not well matched to the ranges of ionizing radiation. The theoretical maximum efficiency for Schottky barrier structures is approximately 0.3 % for alphas and approximately 0.1% for low energy betas. Schottky barriers are less susceptible to radiation damage since the atomic layer bonding the metal to the semiconductor is thin and is thus less prone to displacements caused by the radiation. Schottky barriers can be formed between liquid

semiconductors and metals. These types of Schottky diodes are not as prone to radiation damage since the liquid constantly wets the interface.

Fission fragments have a better match (a range of about 5 μm) for the ~100 nm depletion region of a Schottky barrier diode. For fission reactions combined with a Schottky barrier diode, the theoretical maximum efficiency approaches 3%. This is still not attractive enough for a large scale direct energy conversion system in fission reactors.

4.1.1.4 Radioisotopes Embedded in Solid State Energy Conversion Systems with Limited Self Absorption

By focusing on the matching of scale lengths for the radiation transport process to the transducer in configurations which limit radiation damage, improvement in efficiency is possible. One example which might bear interesting results is the use of solid-state fluorescers which have limited or no self-absorption of the photon emission. This differs from the discussion of solid-state scintillator research (e.g., polymers, phosphors, liquid scintillators, etc.). Scintillators were developed for radiation detection in situations where the dose rates were orders of magnitude lower than nuclear batteries. In prior nuclear battery research the existing scintillators were adopted for use in nuclear batteries. The self-absorption problems in these types of line sources have not been adequately considered as the power density in the scintillator scales up. The solid-state scintillator lifetime is thus short with strong ionizing radiation sources [50-54].

The self-absorption issue was considered for solid-state emitters by focusing on direct wide-band gap materials and excitons [55]. In this approach, the radiation source is embedded in a diamond crystal. As the radiation interacts with the diamond crystal lattice, the electron-hole pairs which form are weakly bound and create an exciton (with a binding energy of ~70 mV). Provided the crystal temperature is on the order of liquid nitrogen temperatures, the electron-hole pairs diffuse together and when they recombine, they do so directly without the need for a phonon. The photon energy is about 5.1 eV. The photon will efficiently exit the crystal and be transported to a photovoltaic cell that has a band-gap that matches well with the photon energy (e.g., $Al_xGa_{1-x}N$ band-gap can be tailored from 3.4eV (x_{Al}=0) to 6.2eV (x_{Al}=1) [56]) The Solid-State Electrical Generator using Radionuclide Induced Exciton Production (SEGRIEP) was conceived of for space exploration. Due to diamond's high thermal conductivity and the background temperature of space being 4 K, it was shown that it is feasible to build a radiative cooling system to maintain liquid nitrogen temperatures in the diamond crystal.

4.1.2 Solid-State Emitter and PV

Diamond is not a direct band-gap material but does have a bound exciton which can be used like a direct band-gap emitter. However there will be no self-absorption of the exciton photon because the photon energy, 5.1 eV, is less than the band-gap of diamond, 5.49 eV. The binding energy of the electron-hole pair that makes up the exciton is 70 mV. This device will have temperature limitations that need to be explored. The theoretical maximum efficiency for this configuration is 33%.

An approach being studied by the authors that is similar to the SEGRIEP concept is to use solid-state emitters based on high quality binary solid state crystals which exhibit wide band-gaps and direct band-gap transitions. In a direct wide band-gap binary material the photon self-absorption and reabsorption processes are in balance until the photon escapes the solid. Loss processes such as luminescence emission from the surface and Auger recombination can be limited by proper design. The photon can escape through a loss cone that is coupled to a photovoltaic cell transducer (Figure 33). Ionizing radiation will create displacements in the solid-state crystal. The rate of displacements will be on the order of 170 displacements per ion fragment. The number of photons create by each fragment (with estimated energy of 10 MeV) is on the order of 2 million photons (fraction of energy into electron-hole pair formation (0.42) times the energy of fragment (10,000,000 eV)/band-gap of semiconductor (2.2 eV for GaP)). Thus the rate of photon generation exceeds the rate of potential trap formation by a factor of 20,000. The potential traps do continue to build up with time. However, if the device operates at a temperature where self-annealing can occur (600 K to 800 K), there will be a rate at which point defects (displacements) are repaired at a sufficient rate to limit the effects of displacements due to radiation damage. It is feasible to use this balance of defect creation and defect repair to extend the lifetime of the solid-state emitter. This device will still have radiation damage issues. Defects will be created in the emitter and the traps that are formed can absorb photons and electrons. The key to the extended lifetime of the emitter is through self-annealing to mitigate trap formation. Displacement issues are more serious with binary materials such as, III-V, than with diamond (used in the SEGRIEP concept). The physics of the process is still being researched and refined.

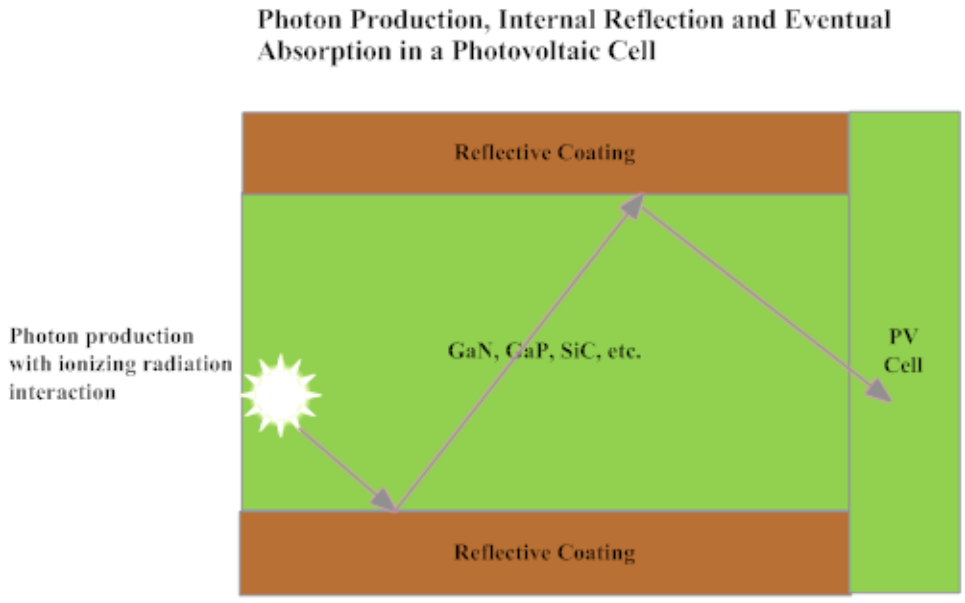

Figure 33. The solid-state material interacts with radiation and produces an electron-hole pair. The pair recombines and produces a photon. The photon is then reabsorbed to form another electron-hole pair or to reflect off the surface. If an electron-hole pair is formed, it recombines

and produces a photon. The process is in balance with few other losses and continues until the photon is lost through the loss cone into the PV cell. The theoretical maximum efficiency for this configuration is 33%.

4.1.3 Hybrid solid-state emitter

A hybrid approach to addressing the self-absorption problem is to form microbubbles with excimer gases in the solid-state material [57]. Micro bubbles can be formed at very high pressures in a solid-state material using ion implantation (up to 4 GPa). At 4 GPa, the density of a xenon gas bubble is on the order of 4 g/cm^3. The transport length of radiation in a high pressure xenon micro bubble is about 5 micrometers, about the scale length of the heavy fragment. As shown in Figure 34 the radioisotope can be coated on the cell's surface. A series of micro bubbles lie between the radioisotope layer and the p-n junction. The particle from the radioisotope is emitted isotropically and the micro bubble serves as both a shield to protect the junction as well as a photon source which emits at the excimer wavelength. The photons then resonate in the PV cell and are absorbed. Even at this high density the issues of pressure broadening should not lead to losses and the micro bubble should not self-absorb. Thus the cell will have a transducer scale length compatible with the radiation source and with the PV cell. The advantages of this approach are that the wide band-gap p-n structure will use a thin film with the radioisotope coated or imbedded into the structure. Wide band-gap materials can operate at high temperatures without efficiency loss and have high thermal conductivities. The films can be stacked, which will allow for scaling of the power source at relatively high power densities (see discussion on the limitations of nuclear battery power density). Problems with this mechanism do exist. Even though it is well known that micro bubbles form by ion implantation, the possibility of the bubble delaminating may be a problem. The theoretical maximum efficiency for this configuration is 20 to 30 %.

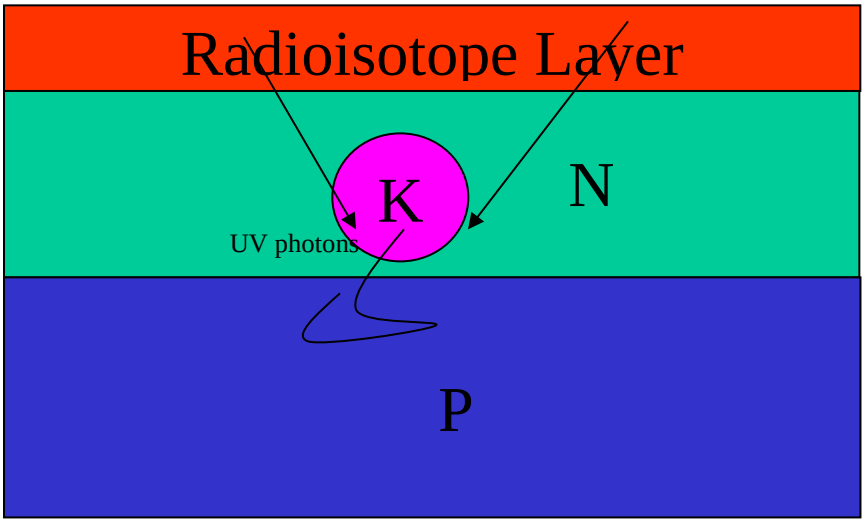

Figure 34. Option A: Micro bubble as a radiation shield as well as a way of converting the kinetic energy of radiation into narrow band UV photons that are absorbed by the p-n junction.

4.1.4 A Method of Charge Collection in a Solid-State Current Source Generated with Nuclear Radiation

The most efficient means of converting the ion pairs produced in matter by ionizing radiation is to directly collect the charge. In a solid-state device, the fraction of the energy from ionizing radiation which goes into electron-hole production is going to be the band-gap energy (E_g) divided by the W value. From Table 9 the fraction of energy going into electron-hole production in diamond is 0.442. If the charge could be collected with no losses, and then utilized with no losses, the theoretical maximum efficiency of a charge collection conversion method with a diamond substrate would be 44.2%. The depletion region of the diamond substrate can be manipulated by putting a high potential across the cell. This is the approach used for diamond radiation detectors. However, PSpice modeling shows that a good fraction of the current through a load resistor is from the voltage source. If a diode is used to prohibit current flow from the voltage source, then the bulk of the current flowing through the load will be due to the electron-hole pair production in the diamond caused by ionizing radiation. The power in the load is thus primarily generated by the ionizing radiation. Such a device could be constructed as shown in Figure 35. In this figure, an electronic grade diamond crystal is being bombarded with ionizing radiation. The diamond then becomes a current source. A voltage source placed in parallel with the diamond provides the driving voltage for the flow of current from the diamond to the load resistor.

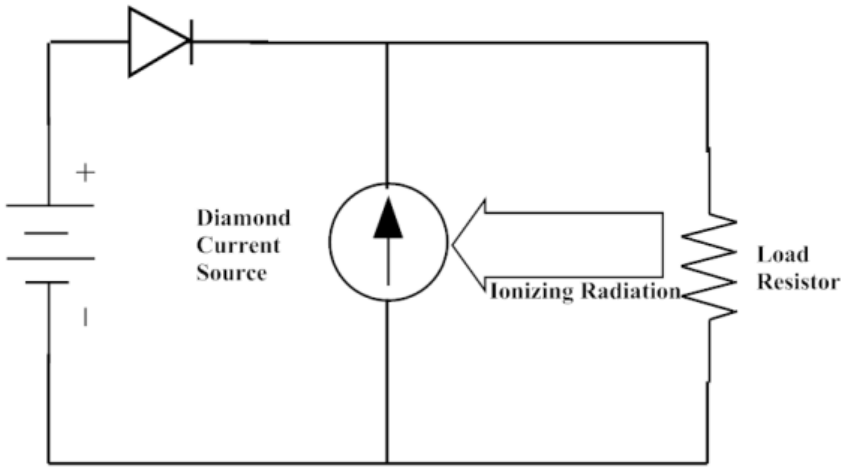

Figure 35. Basic diagram of an electronic grade substrate being bombarded with ionizing radiation and being used a current source to provide power to a load.

The schematic in Figure 35 was modeled with PSpice. In this model the diamond substrate being bombarded with ionizing radiation was modeled as a current source (with current being equal to the rate of electron-hole pair production from the ionizing radiation). In the model the diamond was given capacitance and resistance. The resulting flow of power predicted by PSpice is shown in Figure 36. The problem with this configuration is that the load resistor R_1 must be fairly large (~ 0.1 MΩ to 1 MΩ) in order to maximize power output. If R_1 drops then the power output decreases substantially. The basic approach of Figure 35 shows that the current generated in diamond by the interaction of ionizing radiation with matter can be harvested by a load resistor through the use of an external driving voltage. Any deviation from the predicted theoretical maximum efficiency of 44.2% will be due to electron capture in the diamond and losses in the circuit. The electronic grade diamond has a suitable carrier lifetime to mitigate internal losses. This approach should be able to come close to the predicted theoretical maximum.

Figure 36. PSpice model output which shows that the drain on the battery is 1.01×10^{-16} W while the flow to the load resistor (R3) is 1.002 microwatts.

4.1.5 Interactions with liquids

Ionizing radiation interacts with liquids by creating ion pairs and excited states. Liquids have been used in liquid semiconductor alphavoltaic cells, betavoltaic cells and fission energy conversion cells. Liquids have also been used in radiolysis to produce chemicals.

4.1.5.1 Liquid Semiconductor Energy Conversion based on Schottky Barriers

The use of a liquid semiconductor to mitigate radiation damage to a nuclear battery was patented with a priority date of November 21, 2003 [58]. The premise of this cell is that two plates with a liquid semiconductor (such as selenium) between them, one forming a Schottky barrier and the other an Ohmic contact, can form a potential barrier which will serve as the driving force for the collection of electron-hole pairs created in the cell. The semiconducting property of a molten semiconducting metal, such as germanium, is accompanied by a rapid temperature-dependent increase in conductivity. Thus the molten material has metallic properties. There exist however some materials which upon melting do not exhibit metallic conductivity but retain their semiconducting properties. These materials are primarily the chalcogens (oxygen, sulfur, selenium, tellurium and polonium). Selenium is particularly interesting due to the decrease in conductivity as temperatures increases thus exhibiting semiconducting behavior at high temperatures. The preferred embodiment of the cell uses selenium as the liquid semiconductor. There is a depletion region that is formed in the cell by the Schottky barrier where the collection efficiency will be close to 100% and there will be a rapid drop off in collection efficiency a diffusion length or so beyond the depletion region. A test cell was built by Global Technologies Inc. and operated at an efficiency of about 1%. This efficiency is greater than the expected efficiencies of solid-state Schottky cells. But the diffusion lengths in a liquid medium should be larger than those in a solid which should lead to higher efficiencies than solid-state Schottky cells. The 1% efficiency reported is reasonable. The basic technology behind the Global Technology Inc. liquid selenium Schottky cell has since been explored by others using a beta source that is mixed with the liquid [59].

A theoretical study was published on a liquid nuclear battery by the Jet Propulsion Laboratory. This study [60] used liquid gallium as the electrolyte in an electrolytic cell. The driving voltage was the work function difference between the anode and cathode (~1.6 V). The basis for the device is that the liquid gallium would be a semi-metal (however the conductivity of liquid gallium is linear with temperature and is on the order of 26 to 46 μΩ-cm which appears to be metallic—e.g., silver has a resistivity at room temperature of 1.59 μΩ-cm). Furthermore, it was argued that the gallium ion does not immediately recombine, thus leading to high current collection efficiencies. But the ion and electron mobilities and carrier lifetimes in the liquid metal were not discussed making it difficult to evaluate the study.

4.1.5.2 Depletion Width of a Schottky Barrier

A Schottky barrier is formed when two different materials with different work functions are placed in direct contact with each other. A Fermi potential will form at the material interface. Because this boundary between the two materials is sharp, a Schottky barrier will have a much

thinner depletion zone than a p-n junction. The width of the depletion region for a Schottky barrier, *W*, is expressed by Sze and Ng [61]:

$$W = \sqrt{\frac{2\varepsilon_s}{q \cdot N}(V_{bi} - V_A)} \quad \text{Equation 49}$$

$$\eta_{dp} = \frac{V_{bi}}{E_g} \quad \text{Equation 50}$$

where V_{bi} is the built-in voltage in the Schottky contact, *N* is the dopant density, q is the unit charge, ε_s is the permittivity of the semiconductor, and V_A is the applied voltage across the junction in the forward bias. In the beta or alpha voltaic mode, V_A=0. A typical barrier height for a SiC Schottky barrier is 1 Volt [62]. The depletion width for a Ni/4H-SiC Schottky diode is given for several donor concentrations in Östlund [63]. With a dopant density of 1×10^{17} cm^{-3}, the depletion width of a Ni/4H-SiC Schottky diode is about 0.25 μm.

The efficiency of a Schottky barrier diode for nuclear energy conversion will be significantly less than a p-n diode due to the smaller depletion width as well as a lower potential barrier height (V_{bi}). The smaller depletion width will decrease the transducer scale length and thus will decrease efficiency. The lower potential barrier height will lower the driving potential efficiency in Equation 36 where V_{bi} is substituted for V_{oc}. The difference between V_{bi} and *Voc* can be substantial, V_{bi} = 1 V and V_{oc}=2.04 V [64], which can reduce η_{dp} by 50%.

4.1.6 Interactions with gases

The interaction of ionizing radiation with a gas leads to both ionization and excitation of the gas. Ionized gases form weak plasmas which typically exhibit a low ionization fraction and a high fraction of neutral species. Weak plasmas emit photons which can be used for energy conversion.

4.1.6.1 Spectral Considerations for Line emitters

In a gas the energy will go into ionization and excitation. In typical gas mixtures, the ionization and excitation produces excited states in the atoms or molecules that make up the gas. For low power density, the bulk of the excitations will occur in neutral atoms and molecules. The line emission will be dispersed over a broad range of the spectra from the ultraviolet to the infrared. Optical emitters based on line emission are subject to self-absorption and will only be optically thin over a limited size and pressure. The efficiency of a specific line with a narrow frequency is typically less than 1% which is generally the theoretical limitation of a single line with few exceptions. One such exception is mercury which can have high efficiencies at very low power density and low pressure (up to 70%). Another exception is sodium which can have

high efficiencies at low power density and low pressure (up 40%). Both mercury and sodium are not acceptable for use in a nuclear battery for several reasons. The low power density requirement means that the size of the fluorescer would have to be very large in order to get a reasonable power output. Secondly, the efficiency of the light source would decrease as the size of the lamp increases due to the self-absorption effects of line emitters (meaning the lower energy state of the emitter is sufficiently dense to absorb photons created by the spontaneous emission of an upper state). Mercury and sodium lamps are useful for fluorescer bulbs or street lights, respectively, because these lamps are scaled to a relatively small size with a low power density to avoid self-absorption, thus they are optically thin. As the lamp scales, it becomes optically thick and loses its efficiency.

4.1.6.2 Spectral Considerations for Excimer emitters

The term excimer is short for excited dimers. A dimer is a short lived dimeric or heterodimeric molecule formed by two atoms where at least one of the atoms has a completely filled valance shell (such as a rare gas). For example, rare gases can't form molecules in the ground state, but can form a molecule in an electronic excited state. Examples of excimer molecules include the rare gas excimers Ar_2* (where the "*" indicates an excited state), Kr_2* and Xe_2*, the rare gas-halide excimers ArF*, KrF*, XeF*, ArCl*, KrCl*, XeCl* etc. and a number of other excimer gas combinations [31]. When an excimer molecule decays by spontaneous emission, a photon is given off by the bound excited molecular state to an unbound state where the atoms making up the molecule become neutral and independent. In an excimer gas mixture (a mixture of gases that form the excimer state), both ionization and excitation contribute to the formation of the excimer states (with about 50% efficiency for photon production for rare gas excimers). Excimers thus depend upon the formation of ions and metastable states by the interaction of ionizing radiation with a gas. In an excimer forming gas, if the pressure of the gas is high enough (usually greater than a half atmosphere), the formation of excimers is favored over formation of atomic excited states (atomic excited states lead to undesirable line emissions from the atom). Excimers emit in a very narrow wavelength range (plus or minus 10 nm). Excimers do not have a bound ground state and thus are not subject to self-absorption. Thus excimer gas mixtures remain optically thin (meaning no self-absorption) over large size, large power density and high pressure.

If the excimer is a rare gas excimer, like the xenon excimer, the bulk of the energy that goes into the formation of xenon ions and xenon metastable states proceeds into the formation of the xenon excimer state. From Table 9, it takes 21.9 eV to form an ion pair. The W* value for xenon metastable state formation (42 eV per metastable state) is also known [31]. The theoretical maximum efficiency for xenon excimer production (η_f) is the ratio of the xenon excimer photon energy (7.2 eV) divided by the W value for ion pair production plus the ratio of the xenon photon energy divided by the W* value for Xe metastable production shown in Equation 51.

$$\eta_f \approx \frac{7.2}{21.9} + \frac{7.2}{42} = 0.5 \qquad \text{Equation 51}$$

Thus the theoretical maximum efficiency of an energy conversion method using xenon excimer formation is about 50%. This value of 50% is approximately correct for all rare gas excimers.

4.1.6.2.1 Photon Intermediate Direct Energy Conversion (PIDEC)

PIDEC is an indirect energy conversion scheme which uses high efficiency fluorescers to convert the energy from ionizing radiation to photons. These photons are then transported to a transducer (photovoltaic cell which band-gap energy is matched to the photon energy) to produce electrical current. A great deal of work has been developed around PIDEC in which different geometrical interfaces between the ionizing radiation and an excimer emitter have been examined. PIDEC was developed to overcome the limitations which were identified in the 1950's for p-n junction based betavoltaics and alphavoltaics (e.g., radiation damage, short lifetime and efficiency). PIDEC addresses some important issues; it is a way of matching the scale length of the radiation source to the transducer (the fluorescer can absorb all of the energy from the radiation source by adjusting size and pressure). It has high theoretical conversion efficiencies and provides a means of shielding sensitive transducers from radiation. Typical theoretical maximum system efficiencies (between 10-35%) can approach the theoretical limitation of rare gas excimers fluorescers as shown in Table 15 where η_f is the fluorescence efficiency, E_λ (eV) is the average photon energy and E_g is band-gap energy of the photovoltaic material. The variation in efficiencies is based on design parameters (e.g., interface between the fluorescer gas and radiation source, the system size, photon transport to the transducer and matchup of transducer to photons). PIDEC was proposed for use with fusion [65], fission [14], and conventional decay sources[6, 66, 67].

Table 15. The theoretical maximum intrinsic photovoltaic, η_{pv}, and ion-to-electric, η_{ie}, efficiencies for selected rare-gas and rare-gas halide excimer fluorescers with matched wide-band-gap photovoltaic materials are shown. The fluorescence efficiency (η_f), the energy of the photon (E_λ) and the band gap of the photovoltaic (E_g) are also shown for select excimers.

Excimer	η_f	E_λ (eV)	Photovoltaic Material	Band-gap Energy (eV)	$\eta_{pv}= E_g/E_\lambda$	$\eta_{ie}=\eta_{pv}\eta_f$
Ar_2*	0.5	9.6	AlN	6.2	0.645	0.324
Kr_2*	0.47	8.4	AlN	6.2	0.789	0.345
	0.47	8.4	Diamond	5.5	0.655	0.308
Xe_2*	0.48	7.2	AlN	6.2	0.861	0.413
	0.48	7.2	Diamond	5.5	0.764	0.367
ArF*	0.35	6.4	AlN	6.2	0.969	0.339
	0.35	6.4	Diamond	5.5	0.859	0.301

KrBr*	0.33	6	Diamond	5.5	0.917	0.302
KrCl*	0.31	5.6	Diamond	5.5	0.982	0.304
Na_2*	0.46	2.84	ZnSe	2.7	0.951	0.437
	0.46	2.84	SiC (3C)	2.3	0.810	0.373
Li_2*	0.42	2.7	$CuAlSe_2$	2.6	0.963	0.404
	0.42	2.7	SiC (3C)	2.3	0.852	0.358

5 Alpha and Beta Voltaic Cell Research Issues

The difficulty in following alpha and beta voltaic cell research literature is that most studies fail to provide enough information for a reader to fully understand the experiment and to properly interpret the results. The problems begin with a complete description of the important variables. These variables include information about the radionuclide source, the mix of materials which make up the source (e.g., a fairly common practice is to mix the radionuclide with gold for example), how the source is geometrically coupled to the cell, the dimensions of the source, the p-n junction material, and both the geometry and dimensions of the p-n junction. To illustrate these factors in an example, suppose that device uses a polonium 210 source (Po-210 is an alpha emitter) which is mixed with silver at a 1:10 ratio. This metal mix is then rolled into a foil. If a 5 μm foil of the Po-210 source material is placed on top of a 1 cm by 1 cm p-n junction made of SiC, then in order to fully describe the experiment it is important to know the ratio of Po-210 to silver, the surface area of the p-n junction, the thickness of the source (t_1), the activity of the source, the thickness of the n-type layer (t_2), the depletion width (t_3), and the thickness of the p-type layer (t_4) as shown in Figure 37. The thicknesses are needed to model the path of alpha particle emissions from the source into the depletion layer. The foil will absorb some of the energy of an alpha particle. For example, commercially available encapsulated alpha sources typically lose ~10% of the alpha particle energy in the source structure [68] (Figure 38). It is reasonable to assume that the Po-210 atoms are uniformly distributed in the foil. In setting up a Monte Carlo transport model, the location of the atom which decays in the foil, the time of decay, and the emission angle can be incorporated. Since alpha decays are isotropic, there is an equal probability that the alpha particle will be emitted at any possible solid angle. Thus half of the emission trajectories are away from the surface of the p-n junction. The Monte Carlo transport model would then follow the trajectory of the alpha particle and determine its path and where electron-hole pairs are created. Thus a complete description of the geometry of the device is necessary. If an experimental paper fails to provide the complete description, then the experiment is not fully described. The reader can't model the alpha or beta voltaic cell without making potentially invalid assumptions about the missing variables. Table 16 presents a representative group of recent alpha- and betavoltaic cell studies from the literature. As the table shows, important properties of the cell need to be reported and it states whether or not these important dimensions were reported.

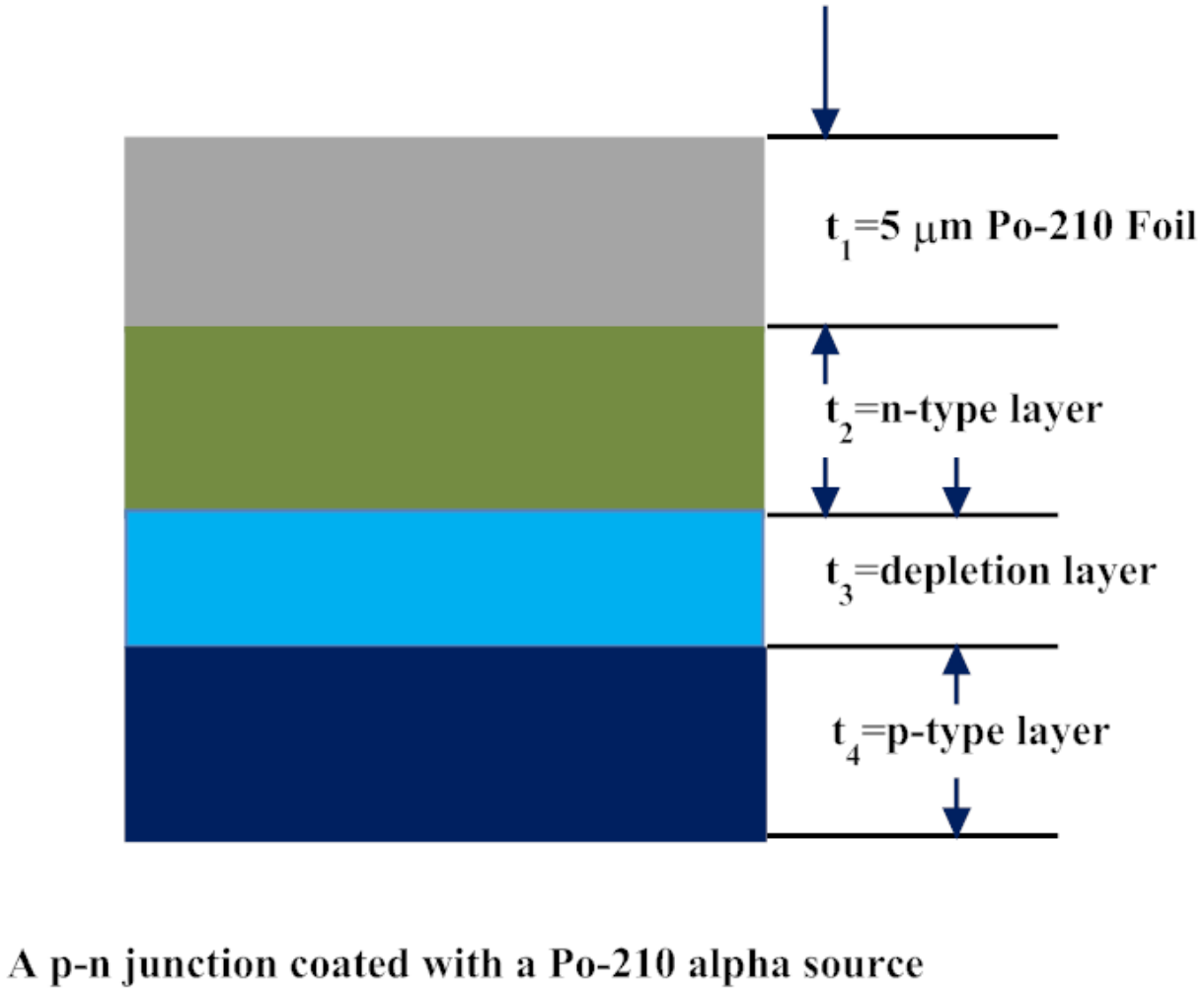

Figure 37. Layout of a typical p-n junction based alphavoltaic using a polonium 210 foil made of 10% polonium and 90% silver placed on a silicon carbide p-n junction.

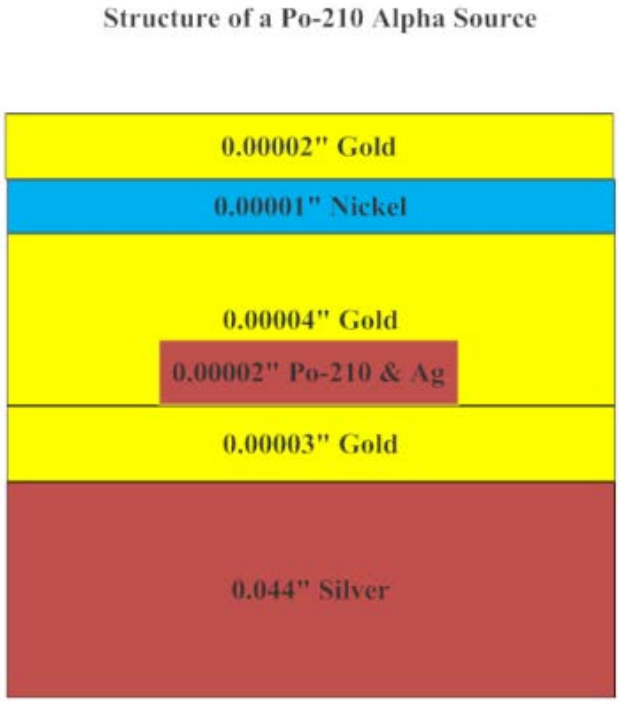

Figure 38. Typical design of a Po-210 alpha source. The polonium 210 foil is made of 10% polonium and 90% silver

The next issue that impacts a reader's ability to interpret an experiment is how the power that is generated from the beta or alpha voltaic is measured. The p-n junction has an operating voltage (V_{op}) and current (I_{op}) which is dependent on the p-n junction's material properties (e.g., type of material, carrier lifetime, defect density, etc.). The product of the operating voltage and current represents the power output of the cell. As can be seen in Table 16, the sources are typically of low activity (A < 1 mCi). This low activity leads to low power output; most reported data is on the order of a nW. So for example, if a SiC cell has an operating voltage of 2 Volts, then the current output would be on the order 0.5 nA. A current level of 0.5 nA is very difficult to measure and requires a great deal of attention to the conditioning of the power lines and ground to take out ripple effects that can cause errors in the picoammeter readings. Picoammeters can also exhibit an electronic drift which can lead to higher output signals at the beginning of a measurement which then decreases with time. If the experimental measurement methods are not well described, the reader would have to decide whether or not the authors took appropriate precautions in making these critical measurements.

The absolute efficiency (η_{ab}) of a cell is defined as power out divided by the total power produced by the radioisotope source Equation 27. Sometimes the efficiency that is reported by researchers in the literature is not the absolute efficiency as shown in Table 16. One of the common ways of reporting efficiencies uses the power out (P_{out}) divided by the power deposited

by the radiation interactions in the depletion layer volume (P_{dpl}). In this paper we will call this the intrinsic efficiency (η_{int}). The intrinsic efficiency will be an order of magnitude higher than the absolute efficiency as shown in (Equation 52).

$$\eta_{\mathrm{int}} = \frac{P_{\mathrm{out}}}{P_{\mathrm{dpl}}} \quad \text{Equation 52}$$

Calculation of the intrinsic efficiency requires specific details about how the alpha or beta source is constructed (an example of which is shown in Figure 38), the exact geometry of the source interface with the cell, and the critical dimensions of the cell. Manufacturers of alpha or beta sources will provide data with regard to a standard design (e.g., Eckert & Ziegler Isotope Product radioisotope sources). However, the thin metal coatings can vary +/- 30% for high precision sources or +/- 200 % for lower precision sources. The thickness of the metal coatings will impact the energies of the alpha particles which are emitted from the source's surface. The emitted alpha particles will have a spectral distribution and an angular distribution which is dependent upon the dimensions of the source. For example, a Nuclespot Alpha Ionizer model P-2042 will reduce the average energy of the 5.3 MeV alpha emitted by Po-210 to about 4.5 MeV out of the source's surface [68]. Models which do not include a full alpha spectrum or angular distribution produce differences in energy deposition which are substantially different from the actual value. Beta sources are even more complex due to beta spectrum considerations [22, 26]. If the author uses a monoenergetic beta source with a particle energy of ⅓ β_{max}, the errors will be substantial. Thus authors who report intrinsic efficiencies need to provide the reader with complete details of source, a complete set of dimensions (e.g., layer thicknesses, areas, etc.), the geometry of the source coupling to the cell, how P_{dpl} is calculated and complete data on the cell design in order for the reader to understand if the calculation of the power deposited in the depletion layer was done correctly. Because so many variables are incorporated in the radioisotope design, in Table 16, all of these variables are combined into a column titled "Is Radioisotope Design Information Sufficient."

Some authors have defined efficiency as the power out (P_{out}) divided by the power absorbed in the device (P_{abdev}). So for the example cell shown in Figure 37, only the alpha particles which have trajectories that intersect the p-n junction are counted. Thus the other 50% of the particles going the wrong way are not counted. This efficiency will be defined as the device efficiency η_{dev}, as shown in Equation 53. The device efficiency will be about twice as high as the absolute efficiency. Again, the same errors which occur in calculating intrinsic efficiency as described above will be concerns from works that report device efficiency.

$$\eta_{\mathrm{dev}} = \frac{P_{\mathrm{out}}}{P_{\mathrm{abdev}}} \quad \text{Equation 53}$$

Another important parameter to note is whether or not an external bias to the p-n junction is used to increase the depletion width of the cell. If an external bias is used, then the external voltage source can contribute current output. Often times the authors do not account for this

important contribution in current measurements and thus will report efficiencies which are higher than they should be.

A final but very important issue is that P-n junction based transducers are highly susceptible to radiation damage which effects their operational lifetime adversely. Ionizing radiation displaces atoms within the crystal lattice thus creating a vacancy. The displaced atom is typically located at an interstitial site [69]. The rate of displacements is directly proportional to the power density created by the interaction of the radiation source with the material. For example, an alpha particle with high Linear Energy Transfer (LET) can displace a couple of hundred atoms in the crystal. The characteristics of p-n junctions degrade with radiation exposure, thus limiting the lifetime of the junction. It has been argued that wide band-gap p-n junctions are less susceptible to radiation, but even wide band-gap p-n junctions are impacted by radiation damage since the binding energy of atoms in the crystal is much lower than the energy of ionizing radiation. Some authors [70] provide time dependent data on the power output from the cell which shows how radiation damage impacts the device.

Table 16. Summary of completeness of information provided by a representative set of nuclear battery papers. A paper should provide information on the isotope used, the detailed design of the isotope encapsulation, details on how the source is interfaced to the device, detail design information on the device, details information on how power out is measured, details on how efficiencies are calculated and was external bias applied to increase the depletion width.

Paper	isotope	Activity	Is radioisotope design information Sufficient ?	Are dimensions of junction or device described Adequate?	How is power Measured (is signal to noise ratio given)	P_{out}	Reported efficiency η_{ab}, η_{int} or η_{dev}	E_{dep} fraction
Andreev, Kevetsky [71]	Tritium & Fe-55	No Activity info; Pdep 10-15 (mW/cm^2) but no 3D info	Only 1D geometry	No doping concentrations	I-V analysis	Max: 0.55 μ W/cm^2	Expect 3%	No discussion
Min Lu, Guo-guang Zhang [72]	Ni-63	33 μCi/mm^2	Yes	Yes	J-V data	Not Stated	0.32%	No
Flicker, Loferski, Elleman [73]	Pm-147	6.3 Ci, 6.8 Ci	Yes	Yes	J-V data	Not explicitly stated, given in a plot (less than 10 μW)	0.4%, 0.77%	No
Li, Yong et al [74]	Ni-63	0.12 mCi	Yes	Yes	J-V analysis	4.08 nW/cm^2	1.01%	no
Clarkson, Sun, et al [75]	Tritium	Only states samples were exposed to tritium gas	No	Yes	J-V data	Not stated. I-V plots given	0.22%	No
Zaijun Cheng , Haisheng San, YanfeiLi [76, 77]	Ni-63	11 mCi	No	No	J-V data	Not stated, plots given	<1%	No
Steffen Deus [11]	Tritium	Only states samples were exposed to tritium gas	No	No	J-V data	129 nW max initial	2.3% (initial)	no
Guo and Lal 2003 [78]	Ni-63 (beta)	0.25 mCi	No electroplated	Yes	I-V analysis	.24 nW	NA	No
Guo and Lal 2003 [78]	Ni-63 (beta)	1 mCi	No Exposed to encapsulated source	Yes	I-V analysis	0.32 nW	NA	No
Cress, Landi, et al 2006 [79]	Po-210	0.35 mCi	No- (foil information issue)	Yes	J-V data	0.0504 μW	η_d =36.3% η_{dev}=3.2% "	No
Cress, Landi, et al 2006 [79]	Am-241	1.12 μCi	No (Foil information issue)	Yes	J-V data	0.0068 nW	η_d =0.8% η_{dev}=0.04%	No

Duggirala, Li, Lal 2008 [12]	Ni-63	9 mCi	No- (foil information issue) calls it a thin film source	Yes	electrical output of 22 nW + 750 uW piezoelectric power at 0.07% duty cycle	22 nW + 750 μW	η_d =5.10%	No
Kavetskiy, Yakubova, Yousaf, et. al. 2011 [80, 81]	Pm-147	1.5*10^{10} Bq	No- (foil information issue)	Yes (Direct Charge Radioisotope Battery)	VI	NA	η_d =4.2% calculated, η_d =3.5% experimental	No
Kavetskiy, Yakubova, Yousaf, et. al. 2011 [80, 81]	Pm-147	9.6*10^{10} Bq	No- (foil information issue)	Yes (Direct Charge Radioisotope Battery)	VI	NA	η_d =7.5% calculated, η_d =8% experimental	No
Kavetskiy, Yakubova, Yousaf, et. al. 2011 [80, 81]	Pm-147	9.6*10^{10} Bq	No- (foil information issue)	Yes (Direct Charge Radioisotope Battery)	VI	NA	η_d =14.1% calculated, η_d =15% experimental	No
Rybicki, Vargas-Aburto, and Uribe [70]	Am-241 (alpha)	5 mCi	No	No	VI	0.015 μ W/cm^2 at 0 hrs 0.0085 μ W/cm^2 at 100 hrs	η_d =18%.	No
Jeffery Snyder, Jagdishbhai Patel, Jean-Pierre [60]	Cm-244 (alpha)	1 Ci	Yes	No dimensions specified.	theoretical calculations, no actual tests	20 mW	η_d =57%.	No
Maxim Sychov, Alexandr Kavetsky, Galina Yakubova [82]	Pu-238 (alpha)	300 mCi	No-	No	Measured power output	21 μ W	η_{dev}=0.11%.	No
Qiao, Chen, Ren, Yuan 2011 [83]	Ni-63	No	No	Yes Schottky barrier diode 1.46 micron depletion width	Measured power output	2.04 nW/cm^2	η_{dev}=0.50%	No
Qiao, Chen, Ren, Yuan 2011 [83]	Am-241	Am-241: 0.018 mCi/cm^2	No	1.46 micron depletion width	Measured power output	Am: 1.25 nW/cm^2	η_{dev}=0.10%	No

In summary, Table 16 is a representation of articles in the literature. As shown in the table, the papers generally do not provide all of the information which is needed for the reader to fully understand the experiment and to properly interpret the results. The complexity of reporting nuclear battery research is due to the nature of radiation transport. Each type of radiation has a scale length (λ_{Radtr}) associated with it which is energy and material specific. The efficiency of the energy conversion scheme is dependent upon the similarity of scale lengths of the radiation source and the transducer (L_{trans}). Inherently, the scale length of alpha and beta voltaic cells

based on a linearly graded p-n junction (on the order of 1 μm), typical of the nuclear batteries described in the literature, is poorly matched to the scale length of the radiation source. Even in a favorable scenario in which the radiation source is an alpha particle, the scale length in a solid is on the order of 20 μm which is not very good. As previously discussed, beta particles have a much less favorable scale length match.

6 Power Output and Power Density

One other important factor in the construction of a nuclear battery is the feasible output power and power density from the isotope. It should also be noted that as the power density increases, so does the displacement of atoms and the resultant radiation damage. In Table 17, isotopes that were identified earlier as having a useful half-life (this governs the shelf-life of the nuclear battery where half the power is lost in one half-life), a useful radiation emission (either beta or alpha), and a useful power output are shown. In the last column of the table, the specific power of the isotope (from the alpha or beta particles being emitted) is shown. The significance of the power output per gram of isotope is that it identifies the maximum achievable power density from the isotope. The interface of the isotope to the nuclear battery will further limit the power density. For example, Gd-148, even though it is expensive to make, is almost an ideal isotope for a nuclear battery due to its 3.182 year half-life and being a pure alpha emitter. Its power output per gram of material is 0.61 W. The density of Gd is 7.90 g per cubic centimeter. The absolute maximum power density from Gd-148 metal is 0.61 W/g times 7.9 g/cm^3 which is 4.8 W/cm^3. If a surface of an alphavoltaic chip is coated with metallic Gd-148, the coating thickness will have to be on the order of 5 μm to minimize self-absorption. Thus the surface area of a 1 gram coating of metallic Gd-148 at a thickness of 5 μm on a chip is 25.32 cm^2. This chip would have 0.61 W of power from the alpha particles emitted by the Gd-148. If the chip efficiency were optimized, it could be around 1 % efficient. Thus the power output of the 25 cm^2 cell would be about 6.1 milli Watt. The effective power density will be on the order of area times the range of the alpha particle (~20 μm) divided into 6.1 milli Watt or about 0.12 W/cc. Since isotopes are usually sold in quantities measured by Curies (Ci), the amount of power produced by one Ci is also of interest. The power that Gd-148 produces per Ci is 0.019 W/Ci. If the chip efficiency is 1% then the cell will produce 0.19 mWatt/Ci.

Alpha emitters are a much better matchup for a p-n junction than beta emitters. It is true that beta emitters have a longer range and thus will have a coating that can be thicker than the alphavoltaic example. Looking at beta emitters, suppose that the isotope chosen is Pm-147. It has a power output of 0.41 W/g and a density of 6.475 g/cm^3. The absolute maximum power density from Pm-147 metal is 0.41 W/g times 6.475 g/cm^3 which is 2.7 W/ cm^3. If a metallic Pm-147 coating were put on a betavoltaic chip at a thickness of ~500 μm to minimize self-absorption, then 1 gram of Pm-147 will coat a surface area of 3.1 cm^2. The poor matchup of the beta range to the scale length of the p-n transducer will create a cell with a low efficiency (~0.1%). The power output of the betavoltaic cell will be about 0.41 milli Watts. Its effective power density will be on the order of 0.0013 W/cc. The power that Pm-147 produces per Ci is 0.44 mW/Ci. If the chip efficiency is 0.1% then the cell will produce 0.44 μW/Ci.

Table 17. Power characteristics of alpha- and beta-emitters.

Nuclide	Decay Energy (MeV)	Half Life (yr)	Decay	Specific Power (W/gm)	Power (W/Ci)
H-3	0.019	12.33	Beta	0.36060	0.00034
Ar-39	0.565	269	Beta	0.03711	0.01003
Ar-42	0.6	32.9	Beta	0.30674	0.01066
Co-60	2.824	5.2713	Beta and γ	0.71042	0.05015
Kr-85	0.67	10.755	beta.	0.51781	0.01190
Sr-90	0.546	28.77	Beta	0.14898	0.00970
Ru-106	0.039	1.0234	Beta	0.25396	0.00069
Cd-113m	0.58	14.1	Beta	0.25714	0.01030
Sb-125	0.767	2.73	Beta	1.58755	0.01362
Cs-134	2.058	2.061	Beta	1.26575	0.03655
Cs-137	1.175	30.1	Beta	0.09540	0.02087
Pm-146	1.542	5.52	EC (66%). Beta (34%)	0.23686	0.02739
Pm-147	0.225	2.624	Beta	0.41193	0.00400
Sm-151	0.076	90	Beta	0.00395	0.00135
Eu-152	1.822	13.54	EC (72.1%), beta (27.9%)	0.17403	0.03236
Eu-154	1.969	8.592	Beta (99.98%), ec (0.02%)	0.24702	0.03497
Eu-155	0.253	4.67	Beta	0.16702	0.00449
Gd-148	3.182	74.6	Alpha	0.61057	0.01884
Tm-171	0.096	1.92	Beta	0.20444	0.00170
Os-194	0.097	6	Beta	0.03976	0.00172
Tl-204	0.763	3.78	Beta (97.1%), EC (2.90%)	0.67819	0.01355
Pb-210	0.063	22.29	Beta (100%), alpha (1.9×10^{-6} %) + beta from	2.66471	0.03495

			Bi210 + alpha from Po210		
Po-208	5.216	2.8979	Alpha (99.9958%), ec (0.0042%)	17.96949	0.03088
Po-210	5.305	0.379	Alpha (100%), γ (0.0011%)	141.143	0.03141
Ra-228	0.046	5.75	Beta	0.01541	0.00082
Ac-227	0.044	21.773	Beta (98.6%), alpha (1.38%)	2.12706	0.00078
Th-228	5.52	1.9131	Alpha	26.05395	0.09804
U-232	5.414	68.9	Alpha	0.70009	0.03205
Pu-236	5.867	2.857	Alpha (100%), fis (1.3E-7%)	18.03220	0.03473
Pu-238	5.593	87.74	Alpha (100%), fis (1.85E-7%)	0.55559	0.03311
Pu-241	0.021	14.35	Beta (99.998%), alpha (0.00245)	2.85580	0.00037
Am-241	5.638	432.2	Alpha (100%), fis (4.3E-10%)	0.10857	0.03338
Cm-243	6.168	29.1	Alpha (99.71%), ec (0.29%), fis (5.3E-9%)	1.64762	0.10954
Cm-244	5.902	18.1	Alpha (100%), fis (1.37E-4%)	2.77754	0.03494
Bk-248	5.793	9	Alpha	5.49388	0.03429
Cf-250	6.128	13.07	Alpha (99.923%),	3.89080	0.03628

			fis (0.0775%)		
Cf-252	6.217	2.645	Alpha (96.908%),fis (3.092%)	18.78859	0.03680
Es-252	6.739	1.292	Alpha (76.4%), ec (24.2%), beta (0.01%)	30.86044	0.03989

The problem with using solid radioisotopes in a thin film is that the resulting device will scale with surface area and will be limited to very low power density. This situation will occur when a thin film of a solid radioisotope is coated on the surface of a solid transducer. The phase of the radioisotope, the phase of the transducer, and the interface between the two determines if the cell scales with surface or volume. The radioisotopes can be embedded with the energy conversion cell in several ways (for volume like scaling) including gaseous radioisotopes, radioisotopes embedded in thin films, radioisotopes embedded in thin fibers, or a microscopic aerosol of radioisotopes. It is possible to obtain volume scaling by using multiple phase interfaces between radioisotopes and transducers as discussed by Prelas, et al. [84].

If the cell scales by volume then it is possible to improve the power density. A PIDEC cell, for example, using gaseous Kr-85 at high pressures scales with volume [85]. For example 1 liter at 1000 atmospheres will contain about 3450 grams of Kr-85[*]. Kr-85 produces about 0.51 W/g. The absolute maximum power density from 1000 atmospheres of Kr-85 is 0.51 W/g times 3.45 g/cc which is 1.76 W/cc. The total power in a liter at 1000 atmospheres will be about 1760 Watts. If the PIDEC cell uses a SiC photovoltaic cell as a transducer, the approximate efficiency of the cell will be approximately 16% [66]. Thus the cell will produce about 281 W or a power density of about 0.281 W/cc. However, as pointed out earlier there is a world-wide inventory of ~290,000 grams of Kr 85 [35] which limits its uses.

$$\left[P + a\frac{n^2}{V^2}\right]\left(\frac{V}{n} - b\right) = RT \qquad \text{Equation 54}$$

Solid radioisotopes can effectively mimic gaseous like behavior by mixing a solid radioisotope in aerosol form with a gas or embedding solid radioisotopes in thin fibers or films

[*] The mass of Kr is estimated using Van der Waals equation of state to describe the relationship between pressure and temperature shown in Equation 54, where *n* is the number of moles of Kr, *a* and *b* for Krypton are 0.5193 Pa·m^6/mol^2 and 0.000106 m^3/mol respectively, *R* is the universal gas constant (8.3145 J/mol·K) and *T* is temperature in Kelvin.

hanging in a gas (Figure 39 and Figure 40). The average density of radioisotopes in the mixed phase systems can be very high thus approaching the maximum possible power density [84].

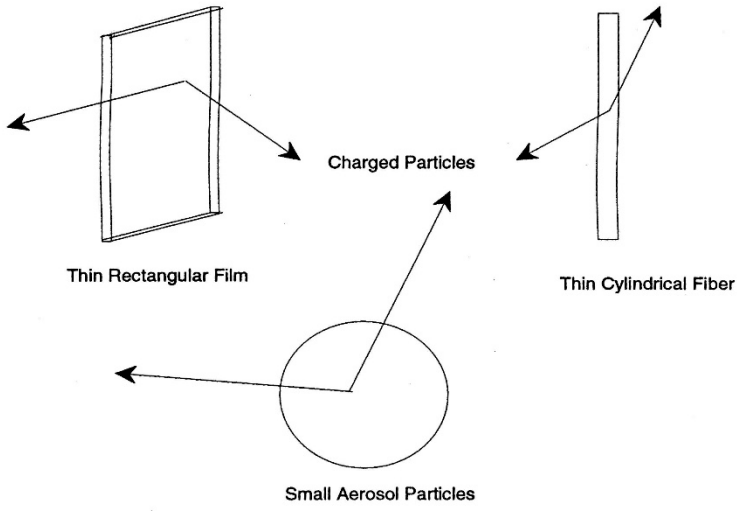

Figure 39. An illustration of the use of thin solid geometries which allow reaction products (indicated by arrows) to escape the solid matrix into a surrounding gas [80].

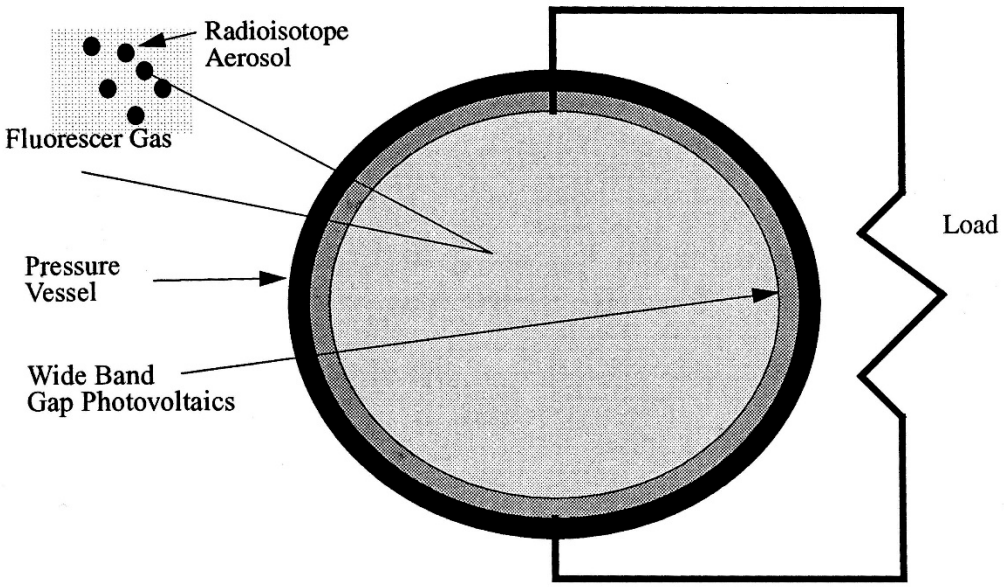

Figure 40. Schematic diagram of a PIDEC nuclear battery which uses a radioisotope fuel in aerosol form [80].

7 Conclusions

In conclusion, microscale nuclear battery efficiencies are dependent upon the matchup of the range of the radiation source to the scale length of the transducer used in the energy conversion process. The scale length matchups are in general poor for radiation/transducer combinations based upon current production, and for the most part are very limited in the maximum energy conversion efficiency. A planar p-n junction, for example, has a very poor scale length matchup between the radiation source and transducer even for heavy particles such as alpha emitters which have a relatively short range. The scale length matchup for beta emitters is much worse. Thus nuclear batteries which use a single planar p-n junction as a transducer in general will have low energy conversion efficiencies.

One can try to geometrically surround the source with p-n junction devices, but even optimizing geometrical collection of alpha or beta particles can only lead to a theoretical maximum efficiency of ~3% [22, 26]. Another approach is to increase the depletion layer volume. This can't simply be done by reducing the dopant densities (due to limitations of impurities in the material during the growth phase) or by doping with compensating impurities (since this will reduce the quality of the crystal and affect its charge carrier lifetime). It is possible to stack thin p-n junctions to increase depletion layer volume but this is expensive and complex. Even more fundamental is that ionizing radiation will displace atoms in the crystal lattice thus causing radiation damage which severely limits the shelf life of a device where the transducer is in direct contact with the ionizing radiation. Even wide band-gap semiconductors will succumb to radiation damage.

Methods in which the range of the radiation corresponds with the range of the transducer will harvest a higher fraction of the energy and thus increase the effective efficiency. For example, PIDEC is a two -step process in which the radiation is matched with the dimensions of a photon emitting material (solid, liquid or gas) and then the photons are transported to photovoltaic cells. The method also has the added benefit of protecting the transducer from the effects of radiation damage. The photon emitting material can be scaled to any size thus the method can be used with any ionizing radiation (e.g., heavy ions, light ions, electrons, gamma rays or even neutrons). The method is impervious to radiation damage with the proper choice of photon producing media (e.g., gases present no issues and studies are underway to find potential liquids and solids). Efficiencies of methods like PIDEC are promising, but the limited supply of radioisotopes themselves present significant limitations for development of a large scale industry.

Radioisotopes do not have a high power density. The highest power density isotope is Po-210 at about 1,315 Watt/ cm^3 (not very interesting due to a short half-life which means a short shelf-life and operational life), but the bulk of the most interesting isotopes have power densities below 1 Watt/ cm^3. However, when taking the inefficiencies of scale matching of the particle range to the transducers, the inefficiencies in interfacing the radiation source to the transducer and the efficiency of the transducers, the power density drops considerably. An additional consideration is that high power density translates to high rates of radiation damage. Nuclear

batteries which use alpha emitters will typically have effective power densities less than 1 W/ cm^3. Betavoltaic cells will typically have effective power densities less than 0.1 W/ cm^3. These power densities do not work well with applications that require miniaturization even if radiation damage issues are not considered.

The supply of radioisotopes is a significant issue for commercialization of nuclear batteries. Even though this paper does not advocate the use of rules of thumb, a simple rule of thumb is useful for gaining perspective on the commercial potential of nuclear batteries when considering the supply of radioisotopes: 1 Ci of activity translates to about 1 milliwatt of power output for a very optimistic 10% efficient nuclear battery. So, considering the world supply of one of the most abundant isotopes released in fission, Sr-90 (estimated at 1.09×10^9 Ci as shown in Table 11), the potential power production is only 1.09 MW. Given that a desirable sized unit would be 100 W, approximately 10,000 units could be constructed based on the world supply of Sr-90. Other sources of isotopes would not even fare that well. For naturally occurring isotopes the available activity is about 1000 times less than isotopes in spent fuel (Po-210 for example is estimated to be 3.28 MegaCi). The production of radioisotopes through neutron capture using a high flux reactor or interactions with the charged particle beam of an accelerator are not promising due to typically low interaction cross sections. The expense (the cost per neutron capture or interaction with an ion) would be a significant deterrence in using reactor or accelerator produced isotopes.

Size is a factor which should also be considered. Typically, the size of the device inversely scales with the power density. Energy conversion methods which use surface scaling will have lower power density (and power output) than methods that use volume scaling. Surface scaling occurs when thin coatings of radioisotopes are placed on the transducer surface, which is typical of a radioisotope in the solid phase coupled with a transducer in the solid phase. It is possible to develop multiphase systems that embed radioisotopes within the transducers in order to reap the benefits of volume scaling. But the methods of embedding isotopes will dilute the radioisotope density and reduce the effective power density. For applications which require miniature power sources, these limitations may prove to be unacceptable. However if miniaturization is not a consideration, (such as portable power supplies for space power systems, mobile power sources for military uses, etc.) moderately sized nuclear batteries may prove useful.

The issue of radiation damage to the transducer is a significant limitation. Transducers which use p-n junctions are highly susceptible to radiation damage which adversely effects their operational lifetime. It has been argued that by keeping power density in the nuclear battery low, that radiation damage can be managed. However, low power density batteries which produce microwatts of power or less are not very attractive for applications which need milliwatt or more power (such as MEMS devices and sensors). Solutions to the radiation damage issue, like the PIDEC design, which is able to shield radiation sensitive transducers, are needed. Alternately, transducers which are radiation tolerant (like thermocouples used in an RTG) work well. It is very difficult to compete with the shelf-life of current RTG designs when a microscale battery is not the goal, although the Advanced Sterling Radioisotope Generator (ASRG) promises to provide efficiencies up to 20% using thermal cycles (branch 1) [86]

In addition to radioisotopes, ionizing radiation is also created by fission and fusion. The range of an ion in matter will be dependent upon the ion mass and energy. Heavy ions, such as those created in fission, will have relatively short ranges than a light ion created in fusion (e.g., proton, tritium, helium-3 or alpha). Direct energy conversion of fission and fusion reactions can use methods employed by nuclear batteries [14, 65, 87, 88].

1 Images

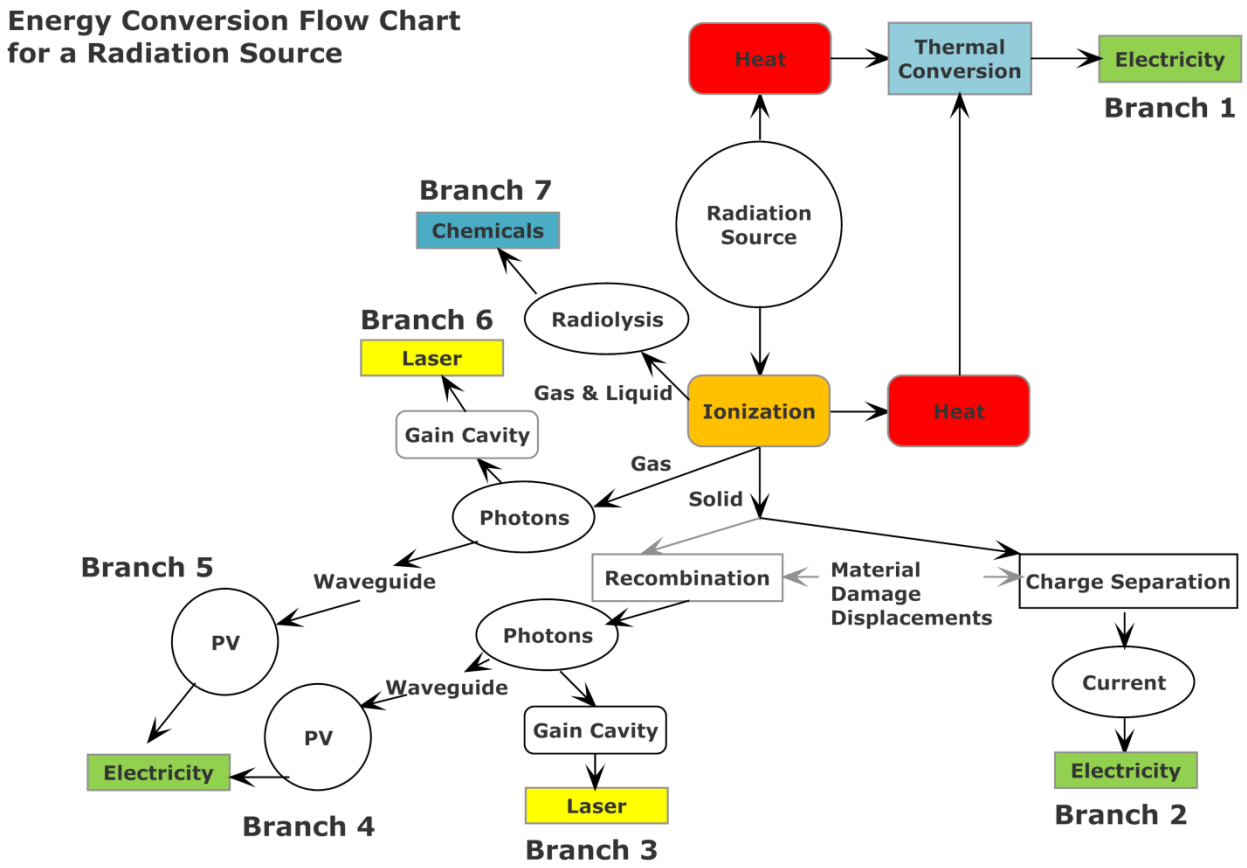

Figure 7. Energy conversion flow chart for radiation sources. Branch 1 uses radiation for heat production. Branch 2 uses the production of charged species in a solid to generate a current flow. Branch 3 uses the production of charged species in a solid to produce laser photons. Branch 4 uses the production of charged species in a solid to produce photons which are used to produce electricity from photovoltaic (PV) cells. Branch 5 uses the production of charged species in a gas to produce photons which then interaction with photovoltaic (PV) cells to produce electricity. Branch 6 uses the production of charged species in a gas to produce laser photons. Branch 7 uses the production of charged species in a gas or liquid to produce chemicals through radiolysis.

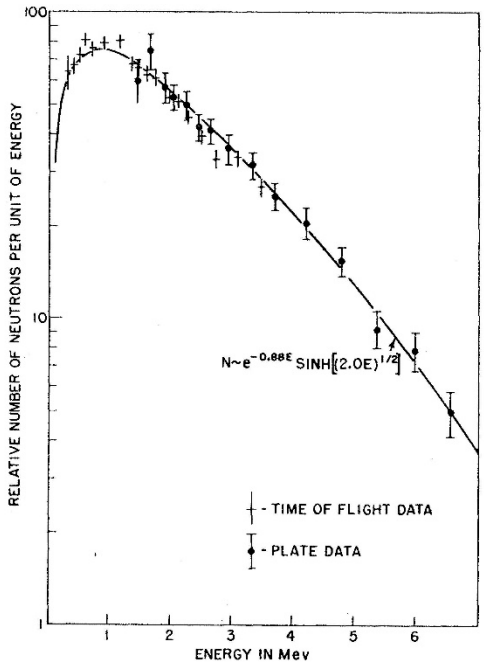

Figure 8. Energy spectrum of neutrons produced by the spontaneous fission of Cf-252 [16].

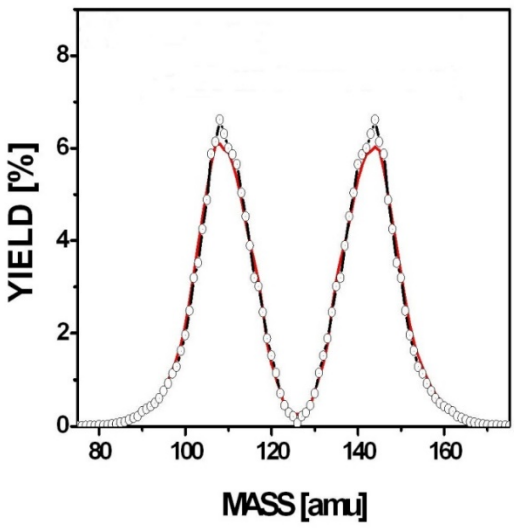

Figure 9. Spontaneous fission yields of Cf-252 [18].

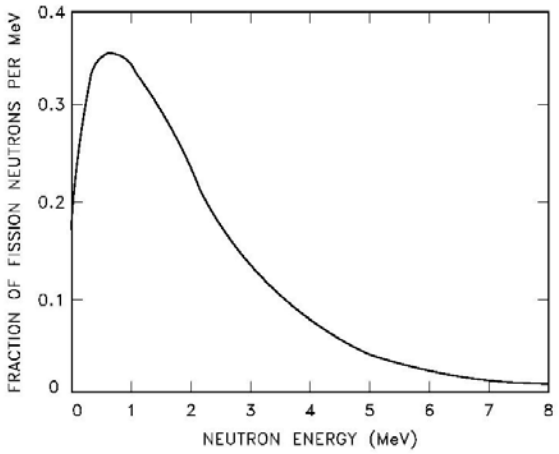

Figure 10. Neutrons energy spectrum produced by the thermal fission of U-235 [19].

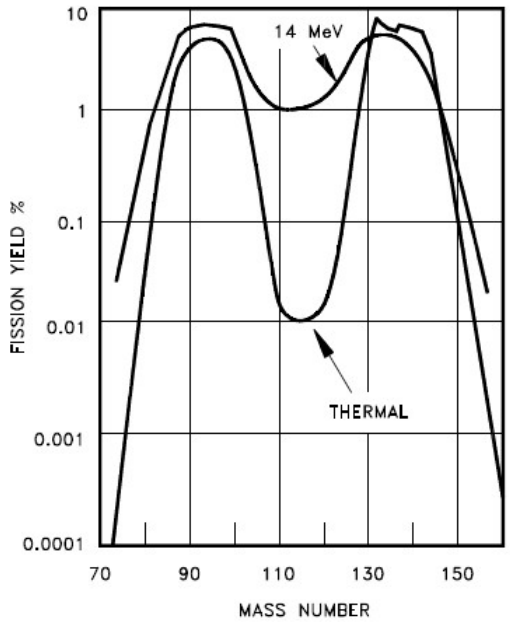

Figure 11. U-235 fission yields for high- and low-energy (thermal) incident neutrons [19].

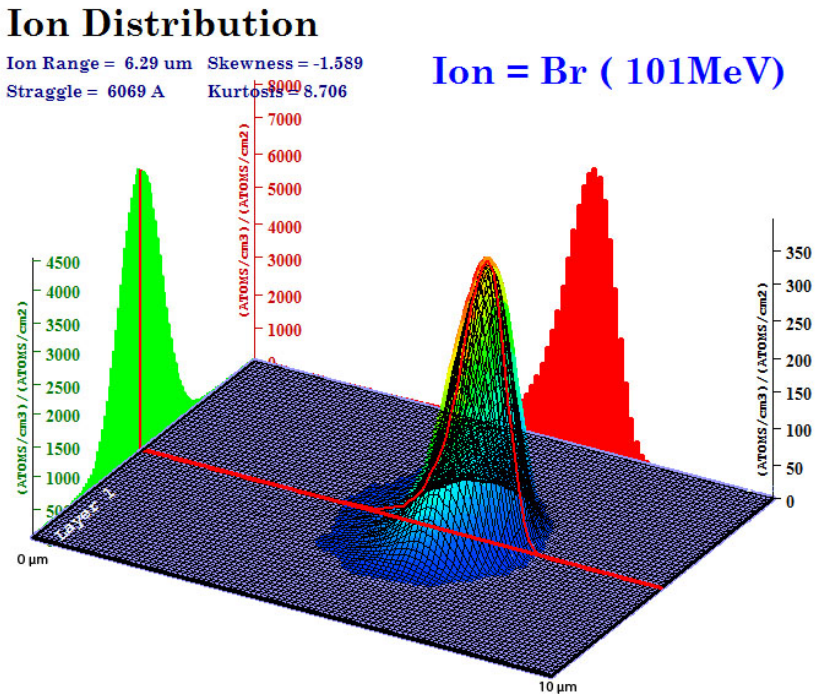

Figure 12. SRIM2011 model showing ion distribution in uranium of 101 MeV bromine-87 ions slowing down [21]. The plot ordinate has units (Atoms/cm^3)/(Atoms/cm^2). By multiplying with ion dose (units of Atoms/cm^2 of bromine-87), the ordinate converts to a density distribution of Br-87 with units of (Atoms/cm^3). The ion source originates from the left side so the two dimensional plane indicates the depth and width of the ion distribution.

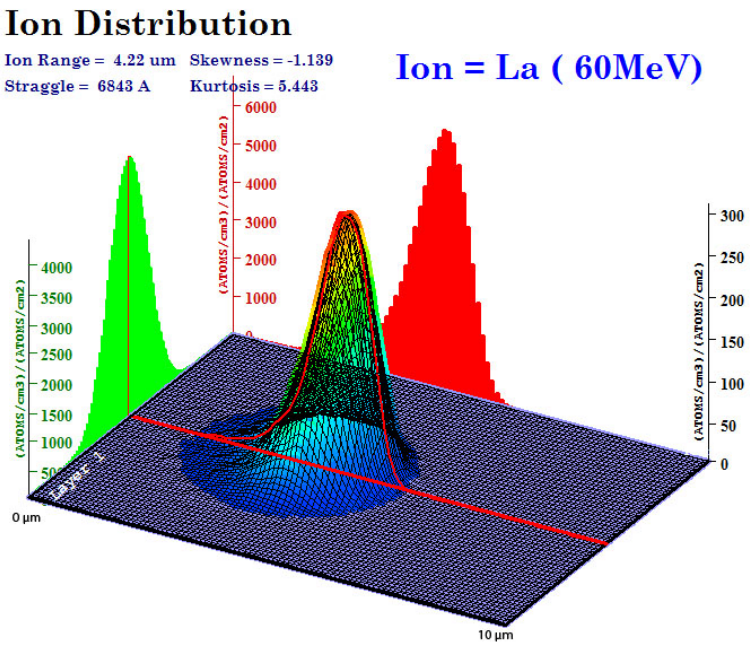

Figure 7. SRIM2011 model showing final ion distribution of 60 MeV lanthanum-147 ions transported through uranium metal[21]. The plot ordinate has units (Atoms/cm^3)/(Atoms/cm^2). By multiplying with ion dose (units of Atoms/cm^2 of La-147), the ordinate converts to a density distribution of La-147 with units of (Atoms/cm^3). The ion source originates from the left side so the two dimensional plane indicates the depth and width of the ion distribution.

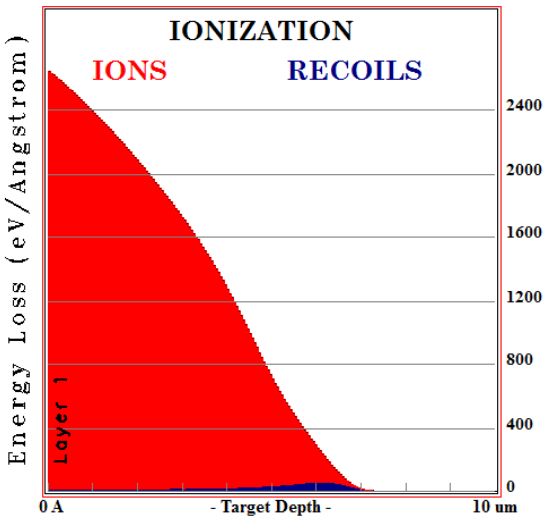

Figure 8. SRIM2011 model showing target ionization in uranium metal by 101 MeV bromine-87 ions[21]. The left ordinate is energy loss (eV/Angstrom), the right ordinate is the number of recoil atoms.

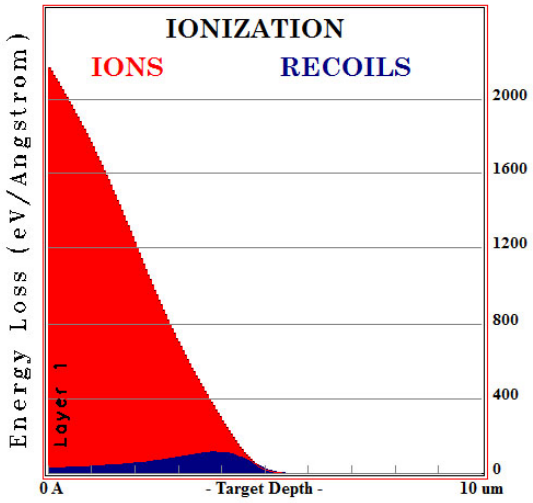

Figure 9. SRIM2011 model of target ionization in uranium metal by 60 MeV lanthanum-147 ion[21]. The left ordinate is energy loss (eV/Angstrom), the right ordinate is the number of recoil atoms.

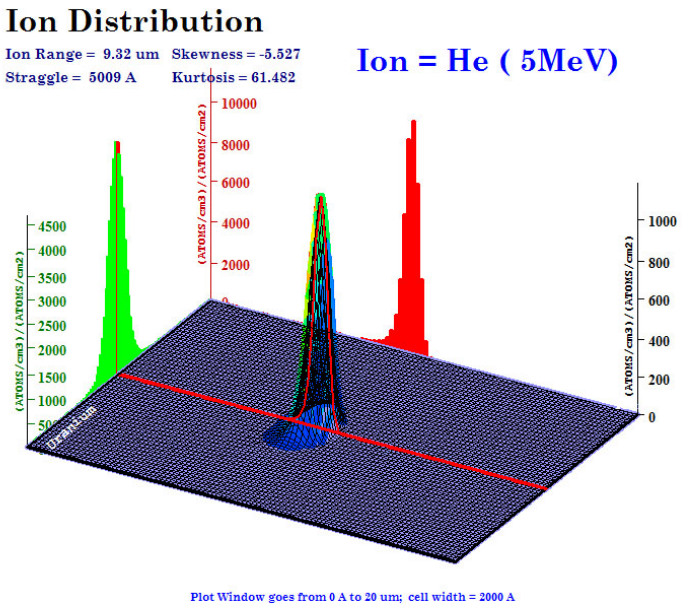

Figure 10. SRIM2011 model showing final ion distribution of 5.3 MeV alpha particles in uranium metal [21]. The plot ordinate has units (Atoms/cm^3)/(Atoms/cm^2). By multiplying with ion dose (units of Atoms/cm^2 of He-4), the ordinate converts to a density distribution of He-4 with units of (Atoms/cm^3). The ion source originates from the left side so the two dimensional plane indicates the depth and width of the ion distribution.

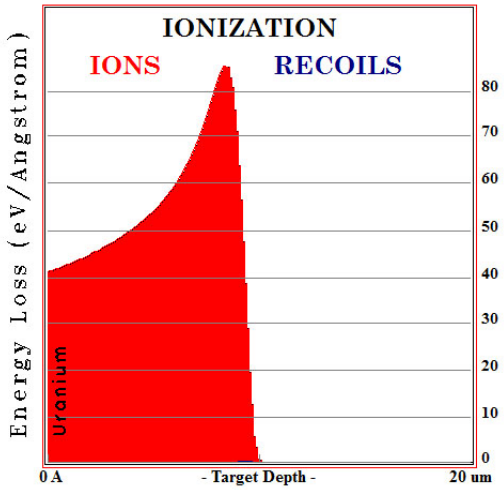

Figure 11. SRIM2011 model showing target ionization produced in uranium metal by 5.3 MeV alpha particles [21]. The left ordinate is energy loss (eV/Angstrom), the right ordinate is the number of recoil atoms.

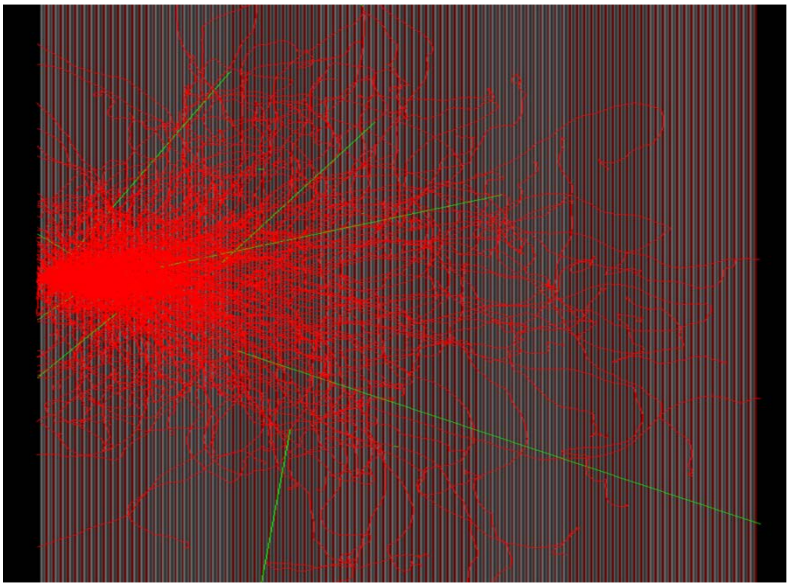

Figure 12. GEANT4 simulation of Sr-90 Beta Decay into SiC of Slab, showing beta particle tracks (random walk path) and bremsstrahlung photons (straight lines)**[22]**.

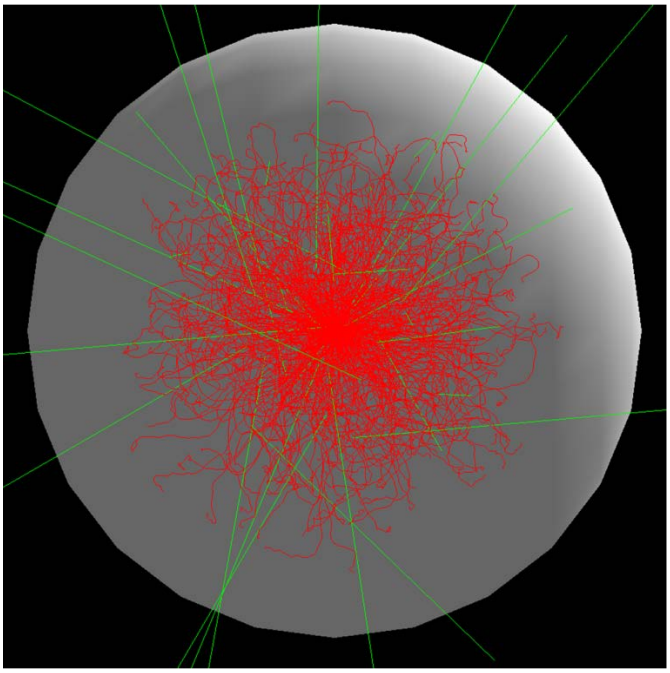

Figure 13. GEANT4 simulation of Sr-90 Beta Decay into SiC of Spherical Model, showing beta particle tracks (random walk path) and bremsstrahlung photons (straight lines)[22]

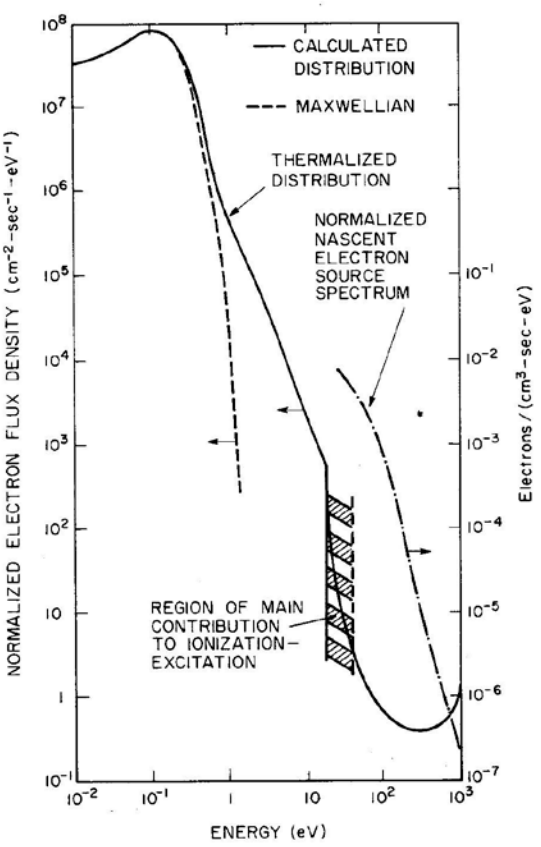

Figure 14. Nascent and asymptotic electron energy distributions for 1-MeV alpha particle bombardment of helium [23].

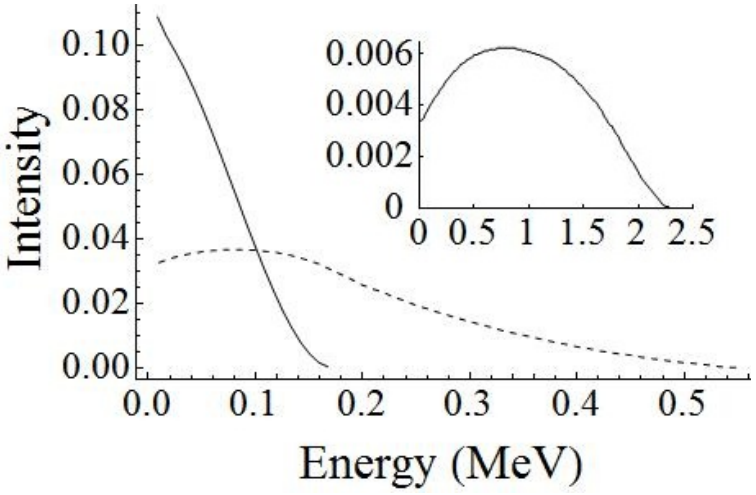

Figure 15. Beta emission energy spectra for S-35 (solid), Sr-90 (dashed), and Y-90 (inset) [22]

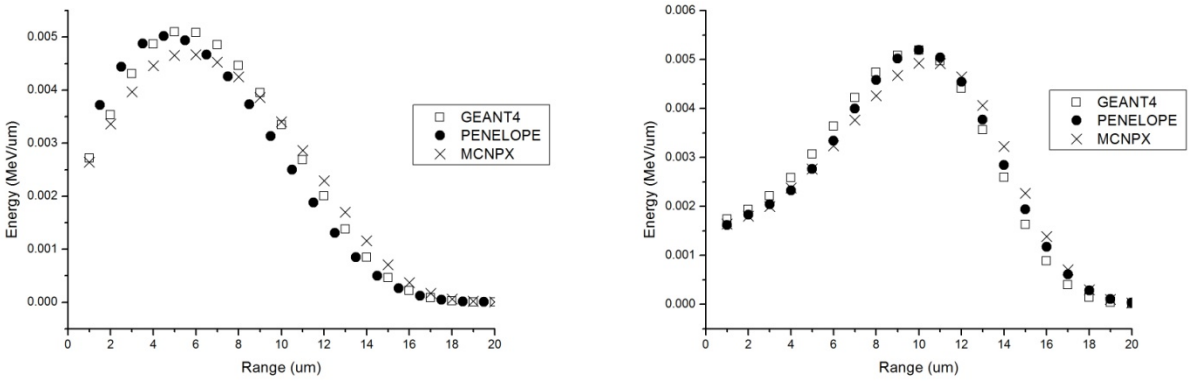
Energy (MeV/um)
Range (um)
GEANT4
PENELOPE
MCNPX

(a)

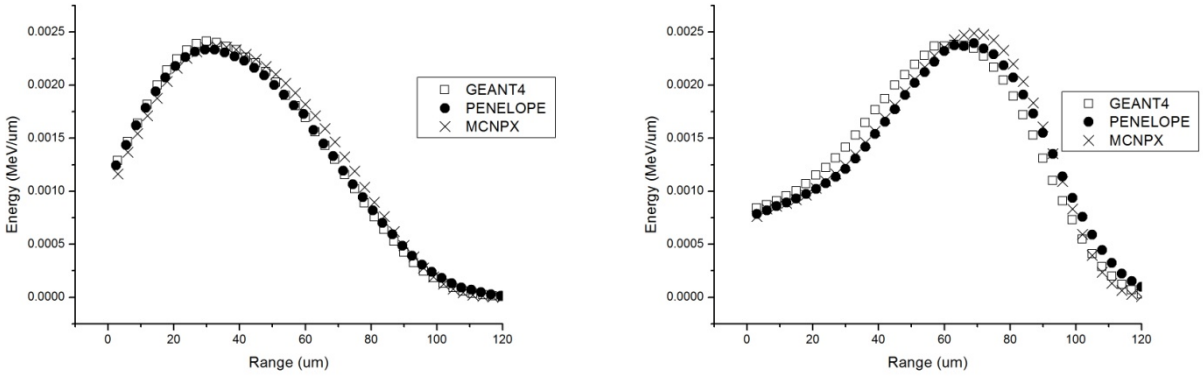
Energy (MeV/um)
Range (um)
GEANT4
PENELOPE
MCNPX

(b)

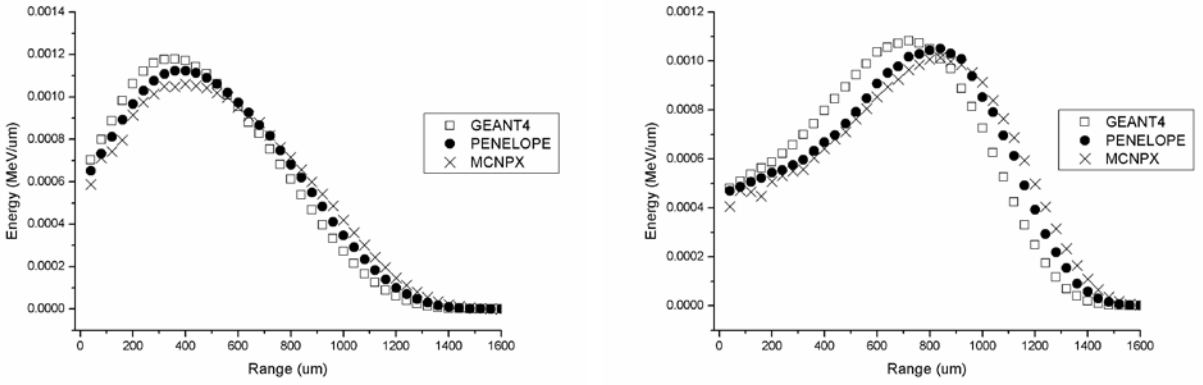
Energy (MeV/um)
Range (um)
GEANT4
PENELOPE
MCNPX

(c)

Figure 16. Simulated energy deposition based on the average beta energy versus distance in both the monodirectional beta source incident on a slab (left) and an isotropic source at the center of a spherical (right) geometries using GEANT4, PENELOPE, and MCNPX codes for (a) S-35, (b) Sr-90, (c) Y-90. [22]

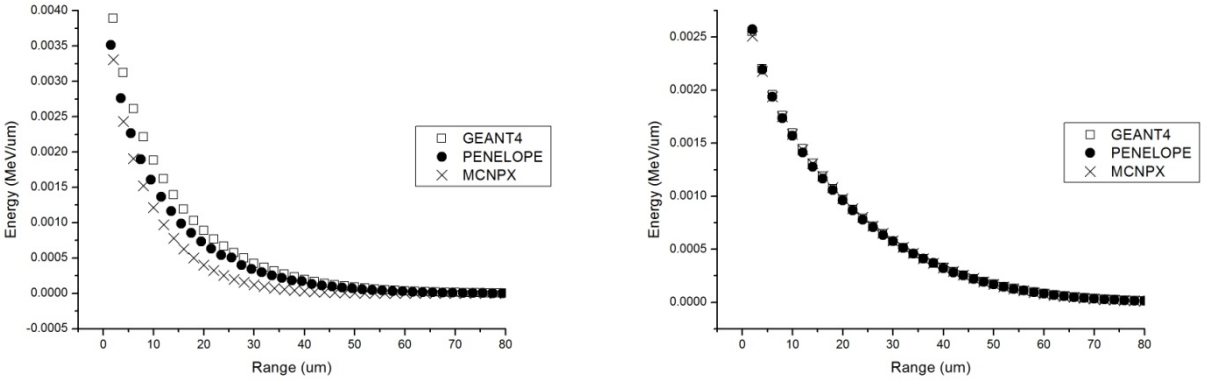

(a)

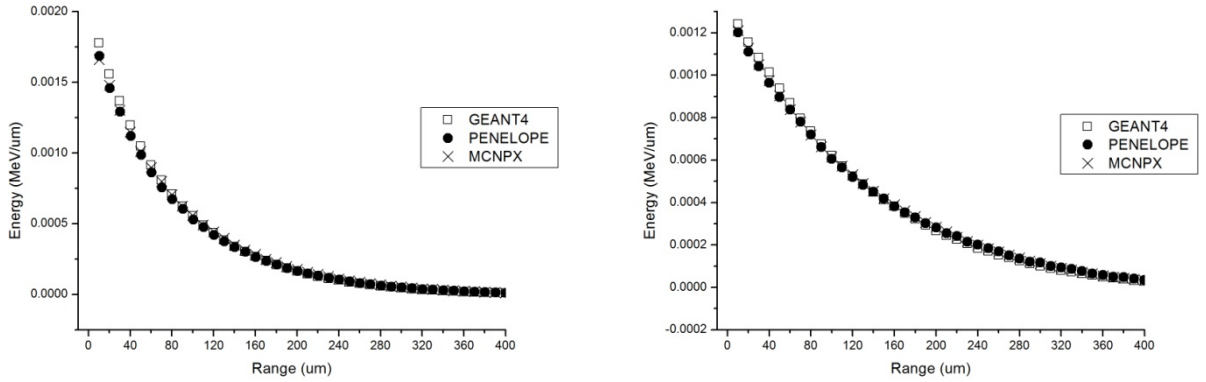

(b)

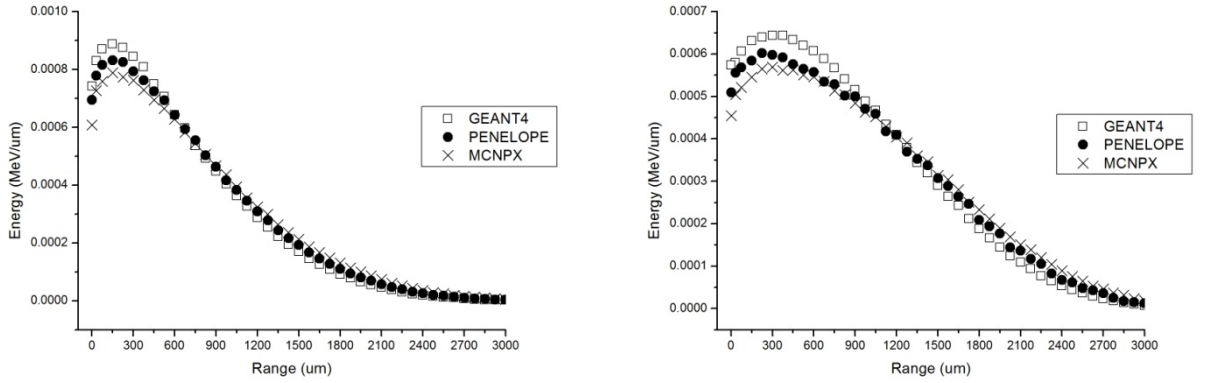

(c)

Figure 17 Simulated energy deposition based on the full beta energy spectrum versus distance for the monodirectional beta source incident on a slab (left) and an isotropic source at the center of a spherical (right) models using GEANT4, PENELOPE, and MCNPX codes for (a) S-35, (b) Sr-90, (c) Y-90.

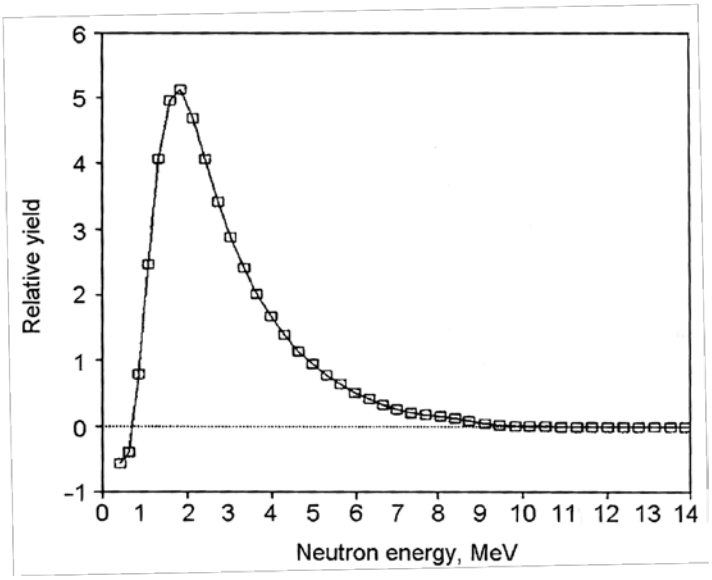

Figure 18. Neutron spectra from the spontaneous fission of Cf-252 [27].

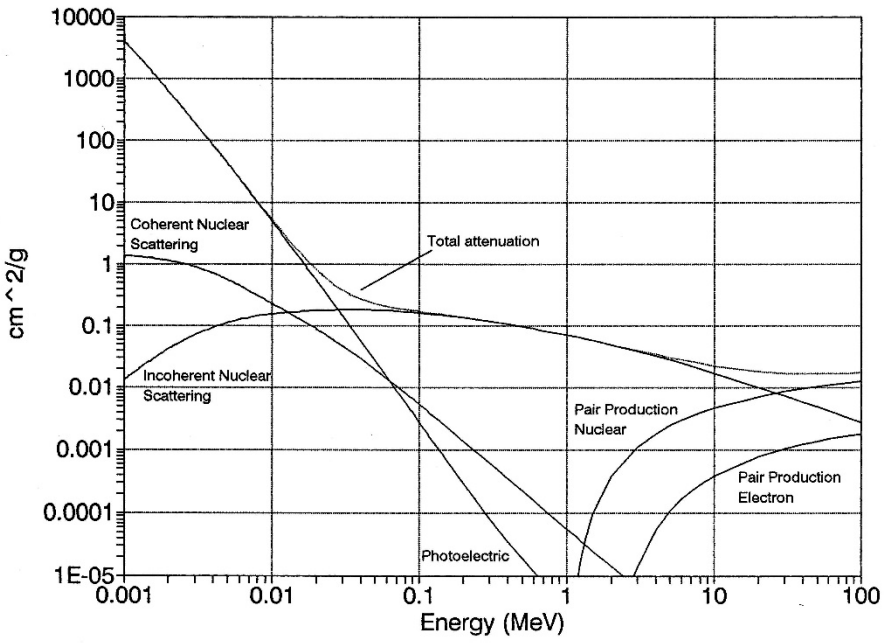

c) Water

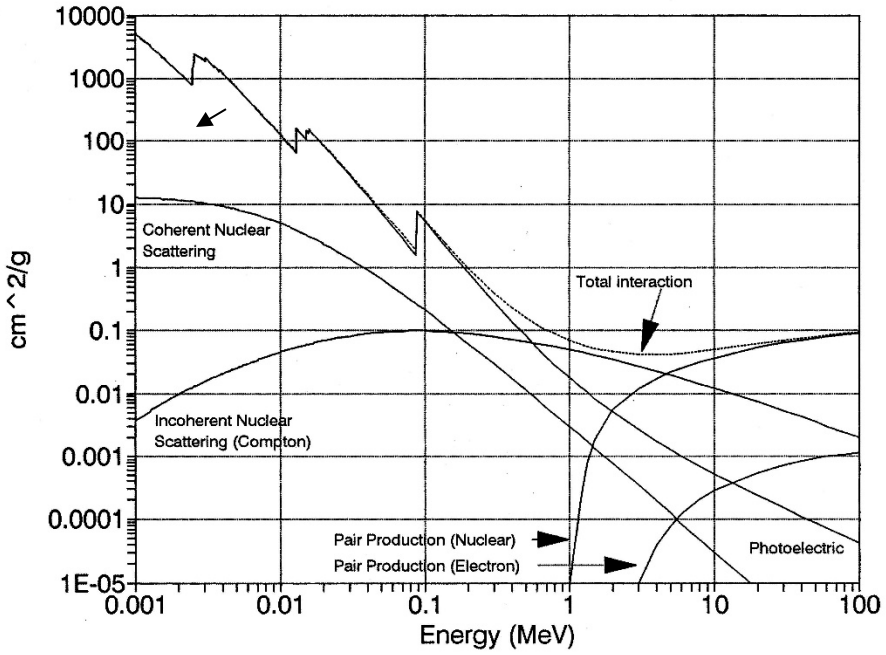

d) Lead

Figure 19. The mass attenuation coefficients for gamma rays of various energies are shown in a) water and b) lead. Note that at low energies the photoelectric effect dominates. At energies near 0.1 MeV, Compton scattering dominates and at very high energies pair production dominates [25].

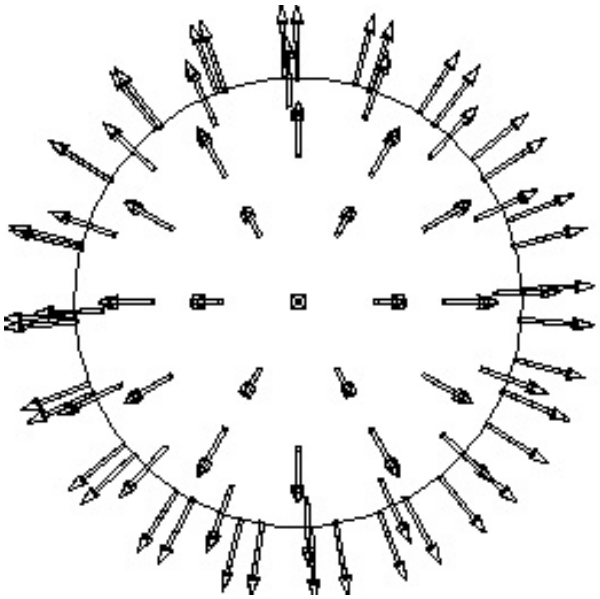

Figure 20. Illustration of a radiation source. The emission is isotropic.

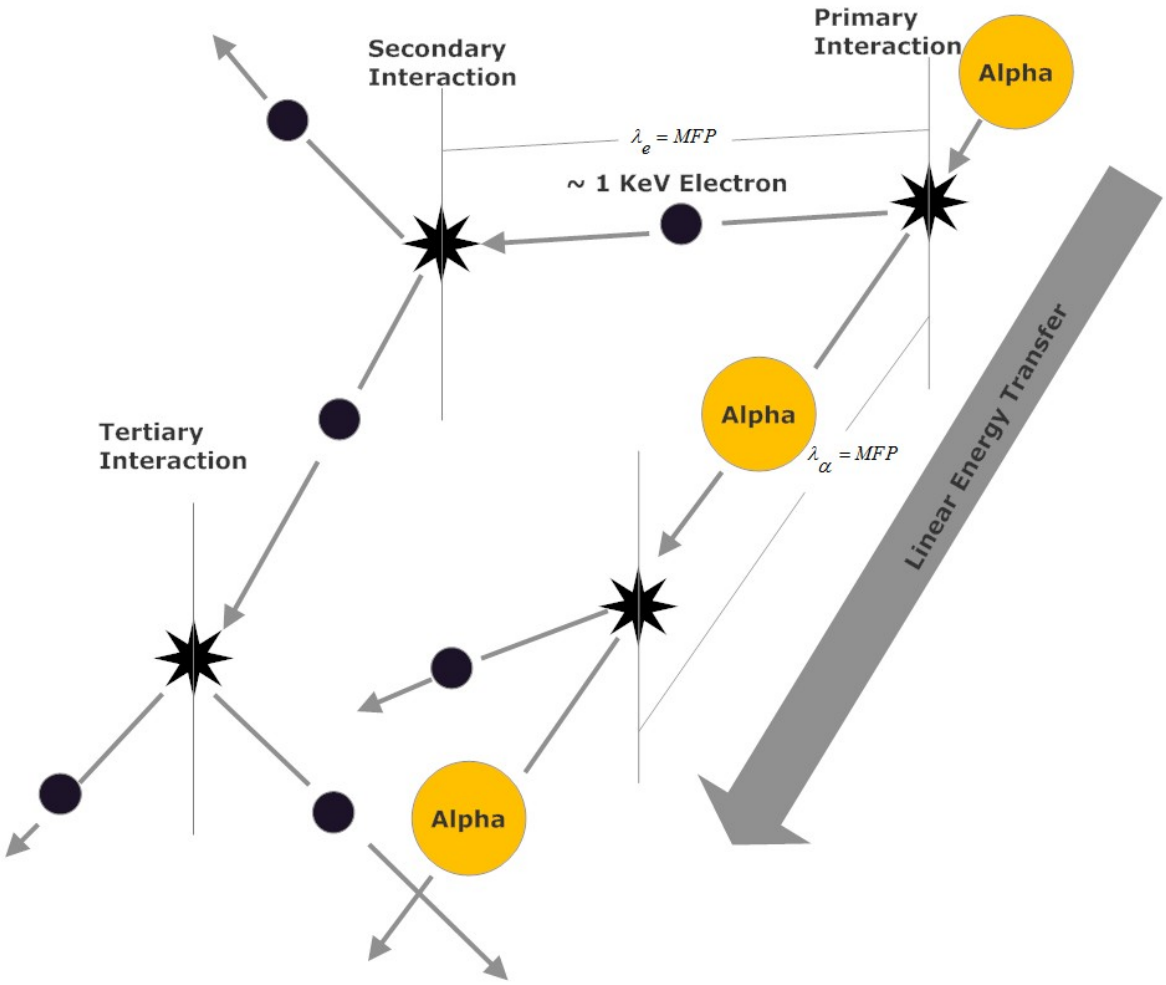

Figure 21. Illustration of an alpha particle interacting with matter. The alpha particle has a linear trajectory through matter and loses energy through Coulomb collisions with electrons in the cloud. These electrons are energetic and can undergo secondary, tertiary and high order interactions as they lose energy.

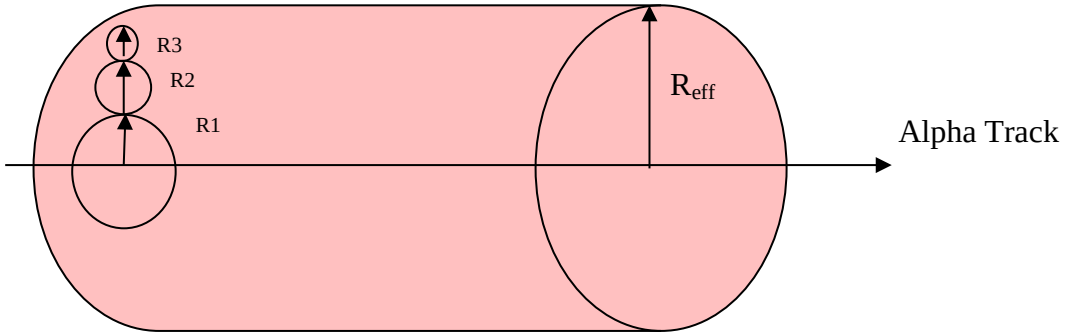

Figure 22. Energy deposition along and radially from the track of an alpha particle is illustrated. The energy of the primary electron is higher than that of the secondary which is higher than that of the tertiary, etc., thus R1>R2>R3>R4 etc. Ionization takes place in a cylinder surrounding the alpha particle path with an effective radius of R_{eff}.

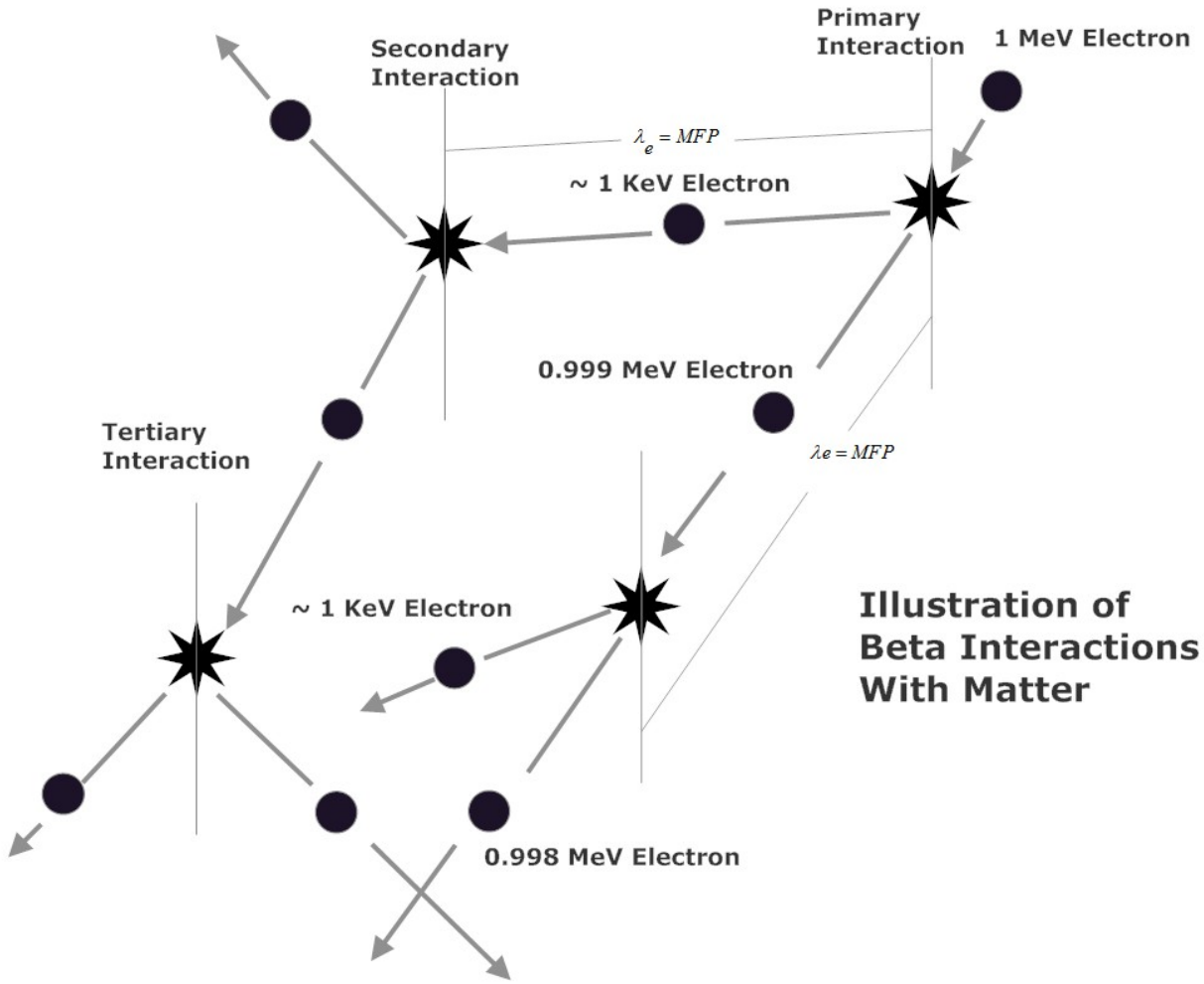

Figure 23. Illustration of a beta particle interacting with matter. The beta particle primarily loses energy through Coulombic collisions with electrons in the cloud. These electrons are energetic and can undergo secondary, tertiary and high order interactions as they lose energy.

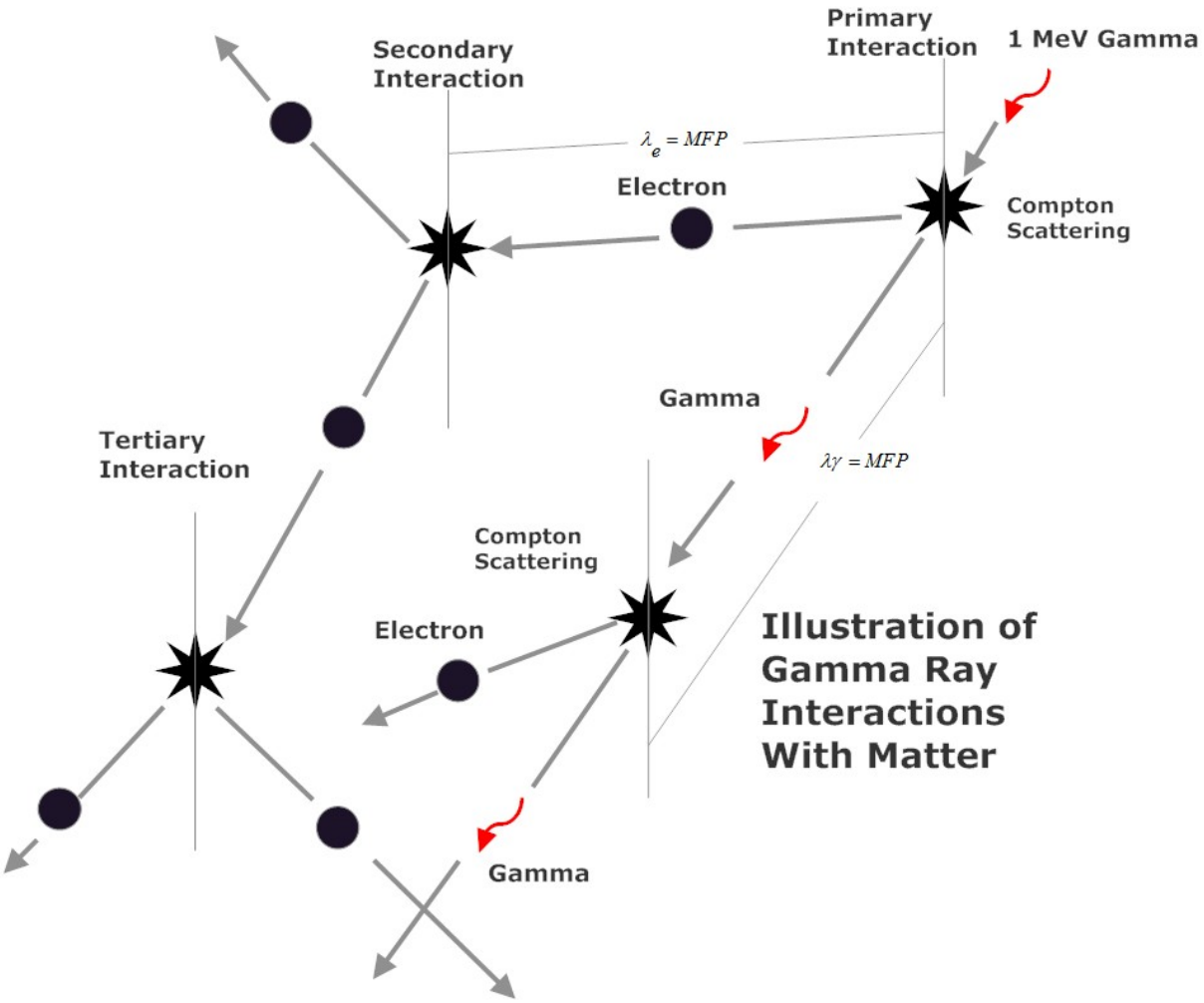

Figure 24. Illustration of a gamma ray interacting with matter. The gamma ray primarily loses energy through the Lorentz force with electrons in the cloud. These electrons are energetic and can undergo secondary, tertiary and higher order interactions as they lose energy.

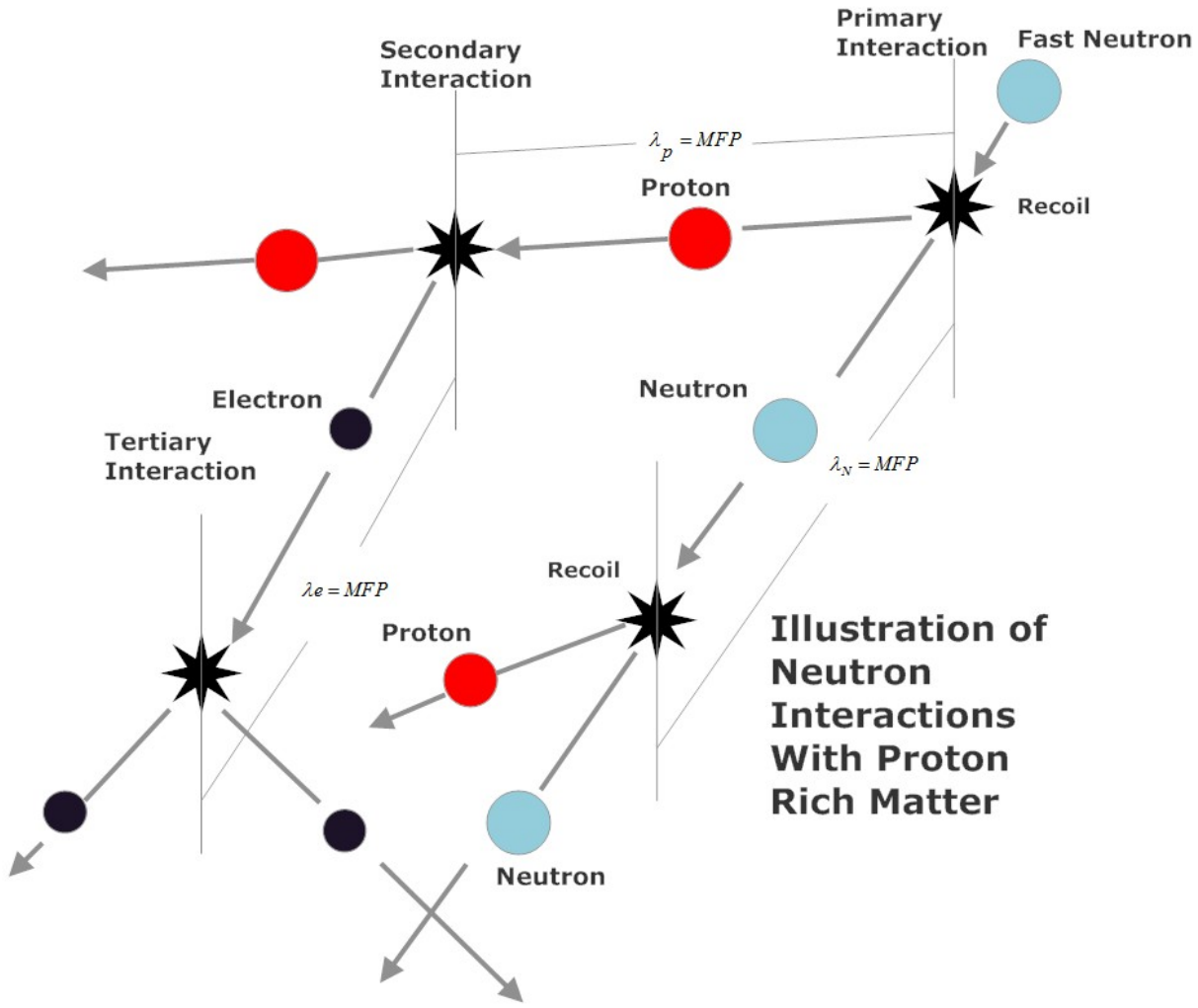

Figure 25. Illustration of fast neutron interactions with a proton rich form of matter. The neutron undergoes an elastic collision with a proton in the target material. The proton recoils and then interacts with the electron cloud, much like the reaction between an alpha particle and matter (Figure 18). The scattered neutron proceeds onward and may have enough energy remaining to undergo another elastic scattering collision with a proton in the material and so forth. On average, a fast neutron will undergo 19 collisions in water before it is thermalized.

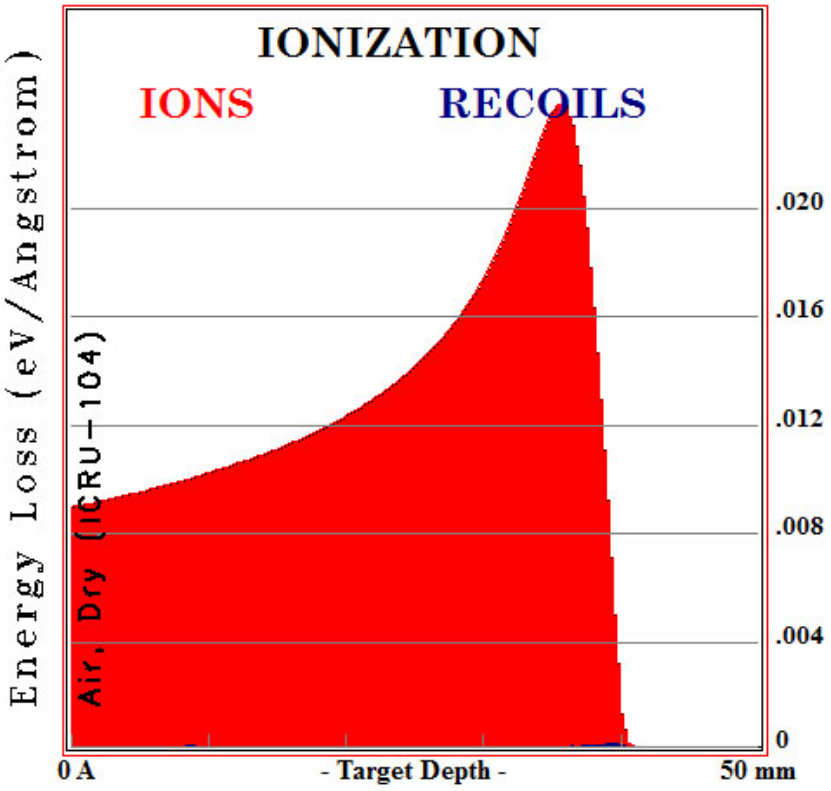

Figure 26. SRIM2011 model showing ionization produced in dry air by 5.4 MeV alpha particle[21].

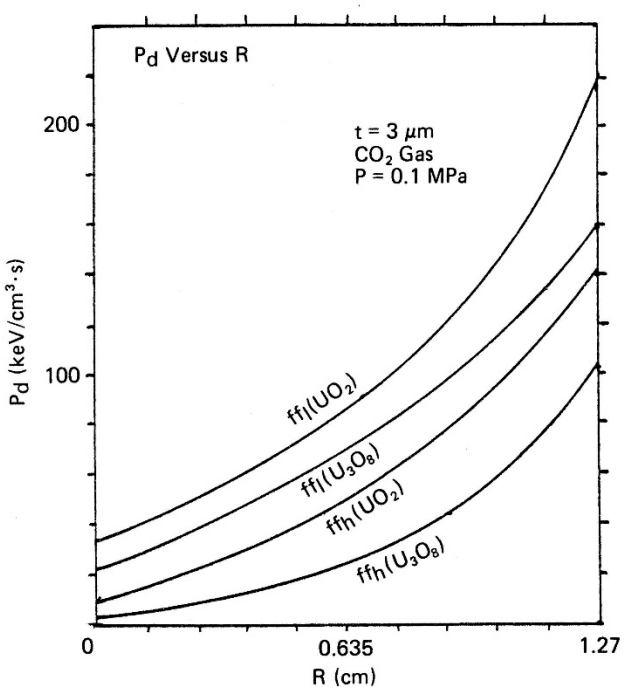

Figure 27. Power deposition (keV/cm^3-s) in a one inch diameter cylinder (with the center being R=0) filled with 0.1 MPa of CO_2 gas and the inner radius lined with a 3 μm coating of UO_2 or U_3O_8. The energy deposition contribution from the light fission fragment (ff_l) and the heavy fission fragment (ff_h) are plotted [34].

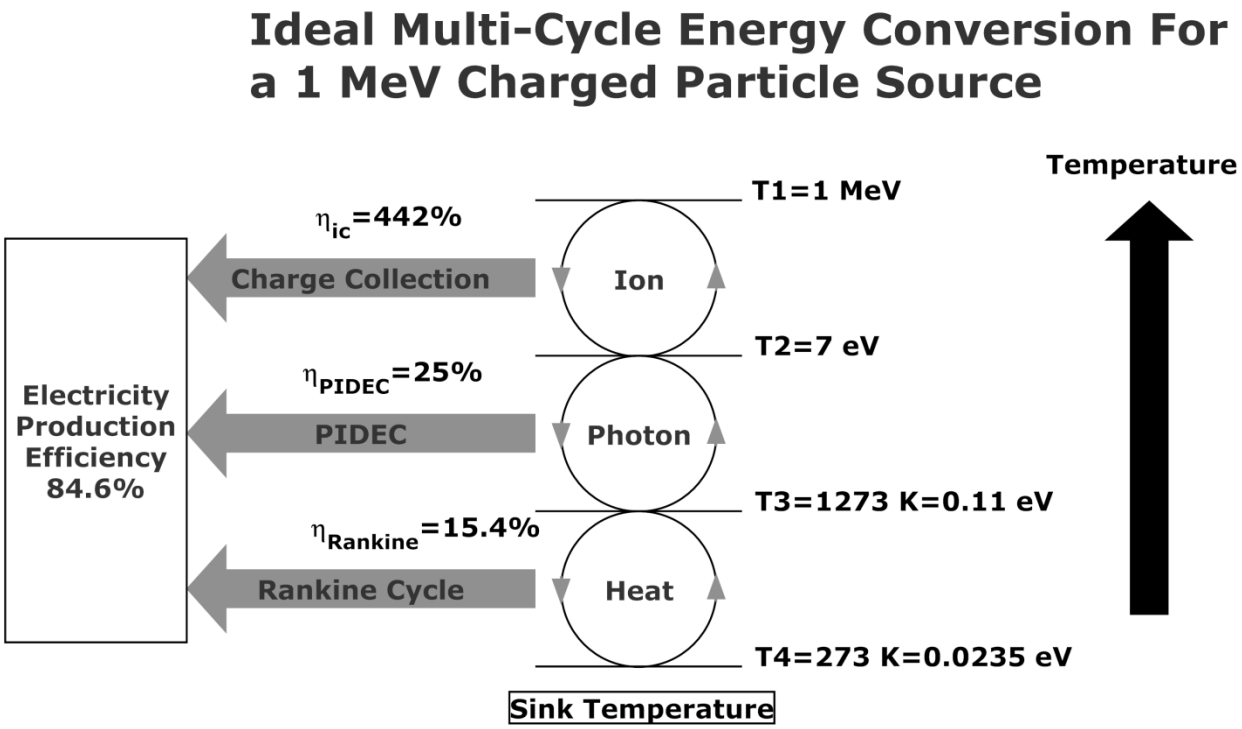

Figure 28. Illustrative example of a multi-cycle energy conversion system where the radiation source starts as a 1 MeV ion which creates electron-hole pairs in a solid. A hypothetical theoretical maximum charge collection device, which approaches Carnot efficiency, produces electricity at an efficiency of 42%. In the second cycle, the remaining energy is in the form of excited states. These excited states produce photons and produces electricity at a theoretical maximum efficiency of 25%. In the third cycle, the remaining energy is in the form of heat and high temperatures. The conversion efficiency of a high temperature Rankine Cycle approaches 50% [39].

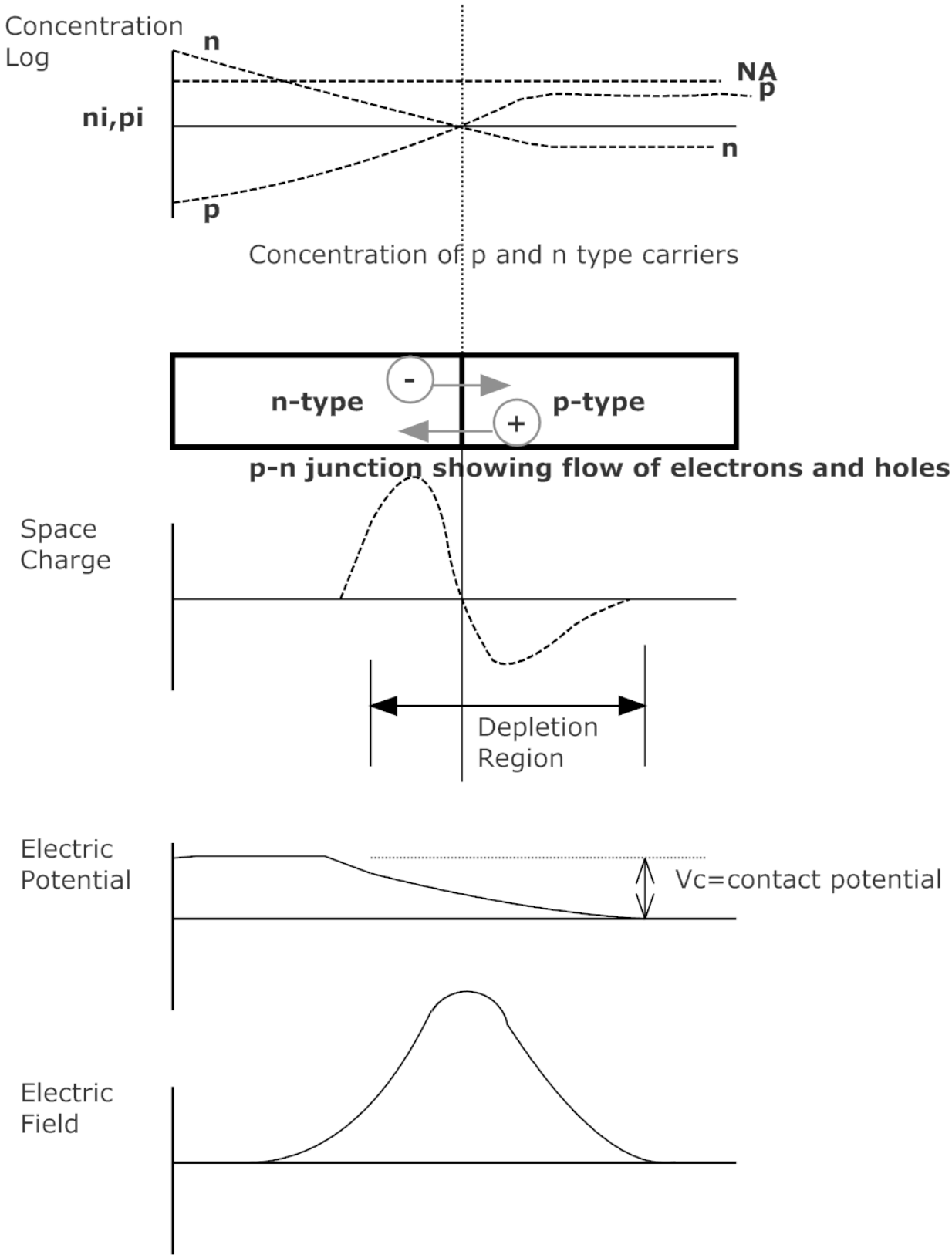
Concentration
Log
n
NA
p
ni,pi
n
p
Concentration of p and n type carriers
n-type
p-type
-
+
p-n junction showing flow of electrons and holes
Space
Charge
Depletion
Region
Electric
Potential
Vc=contact potential
Electric
Field

Figure 29. Illustration of a p-n junction showing (from top to bottom): concentration profiles of n and p type materials; junction interface with charge carriers compensation; diffusion of charge carriers across the junction to produce space charge; the electrical potential; and electric field.

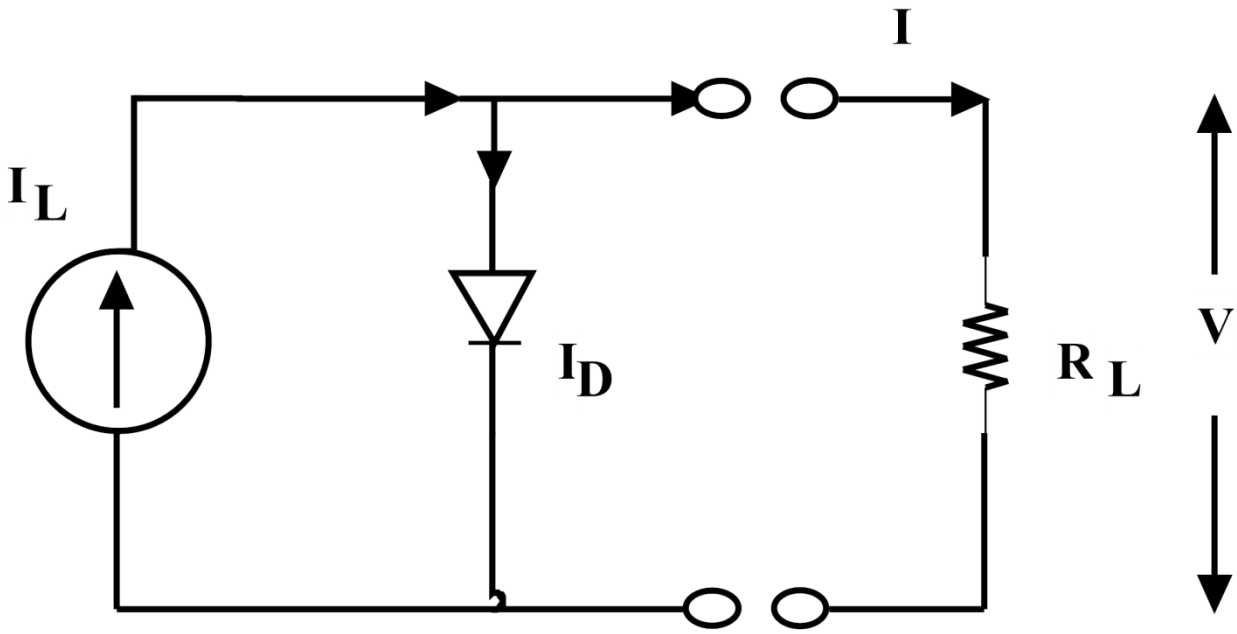

Figure 30. Ideal alpha or beta voltaic cell equivalent circuit.

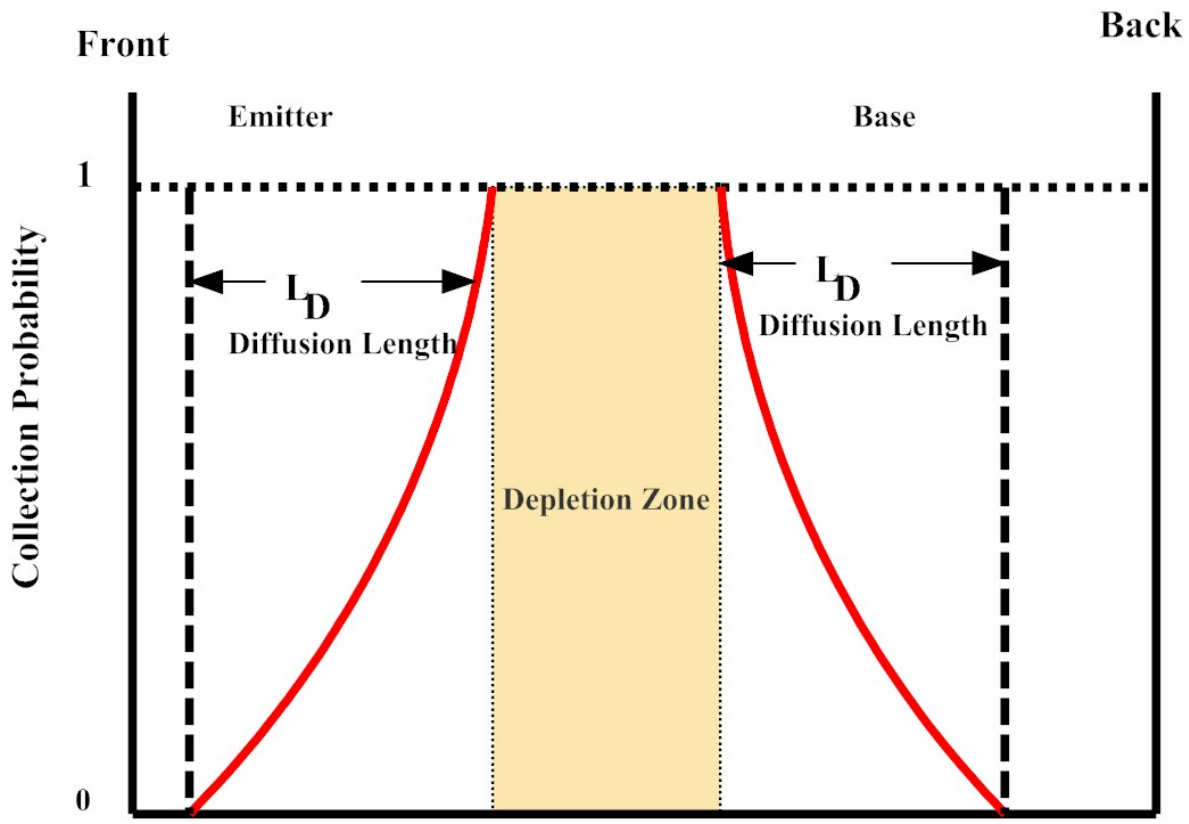

Figure 31. The collection probability for a linearly graded alpha or beta voltaic structure. The collection probability is negligible beyond the diffusion length of carriers.

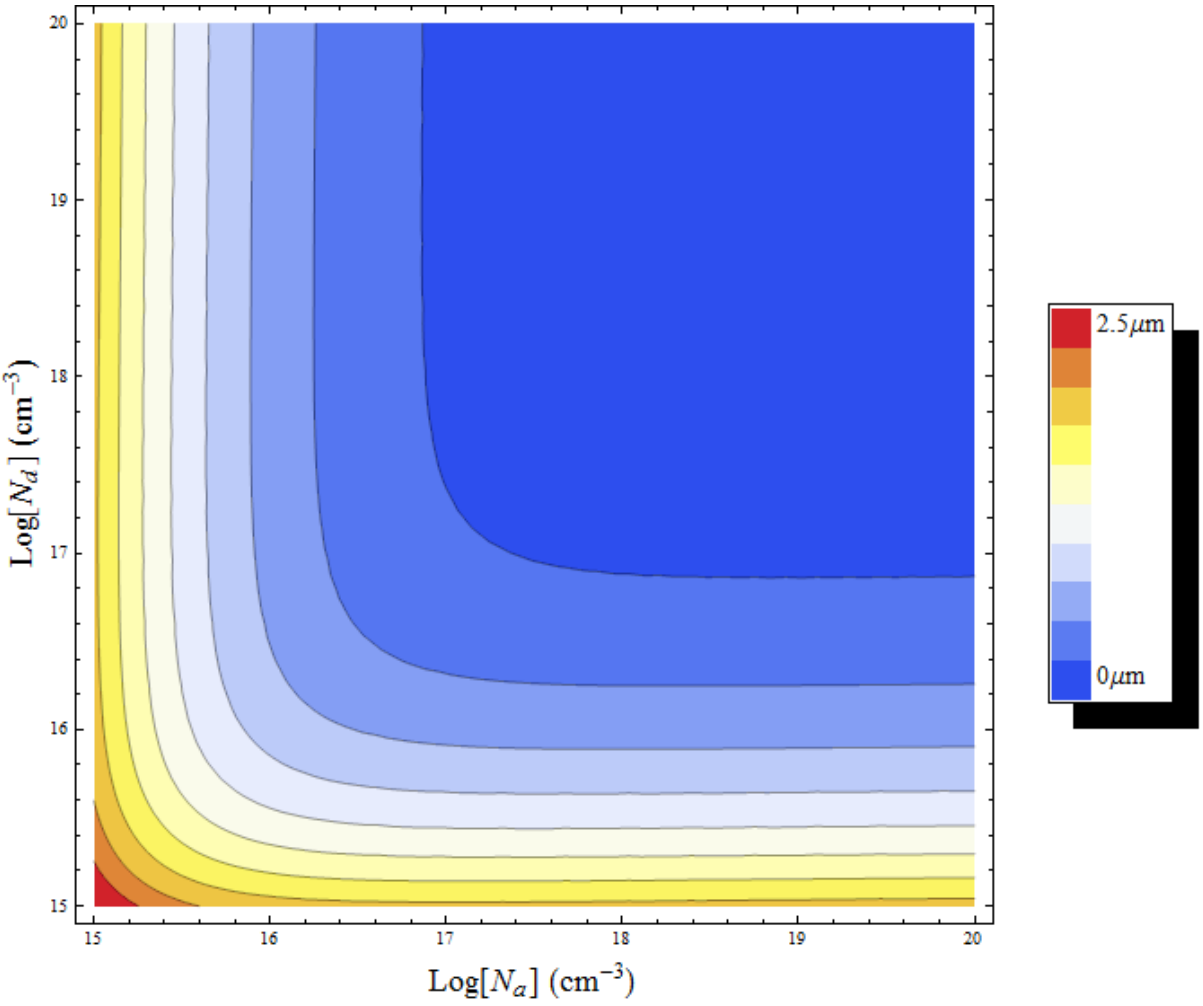

Figure 32. Density plot indicating depletion region width for varying donor and acceptor density concentrations in 4H-SiC.

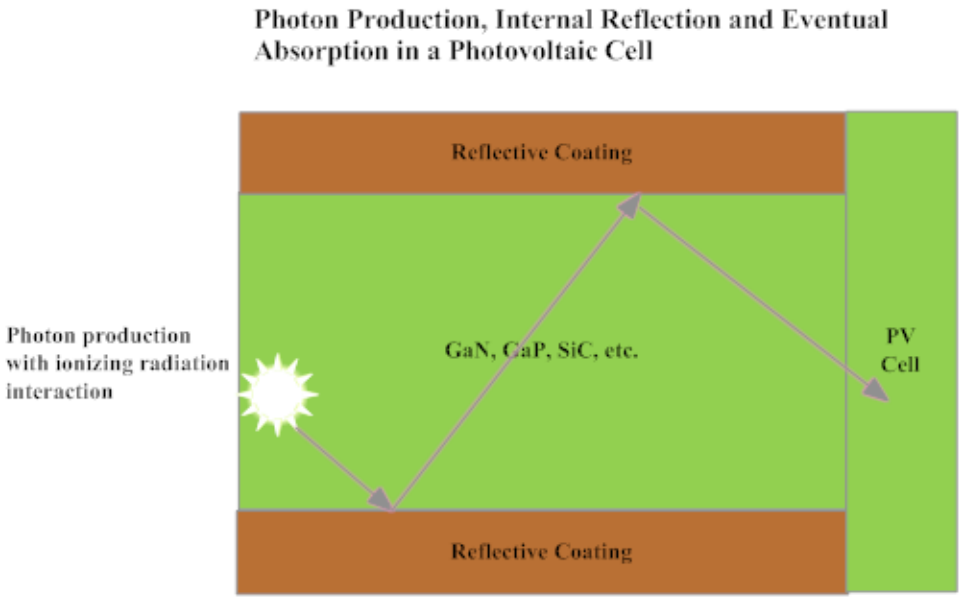

Figure 33. The solid-state material interacts with radiation and produces an electron-hole pair. The pair recombines and produces a photon. The photon is then reabsorbed to form another electron-hole pair or to reflect off the surface. If an electron-hole pair is formed, it recombines and produces a photon. The process is in balance with few other losses and continues until the photon is lost through the loss cone into the PV cell. The theoretical maximum efficiency for this configuration is 33%.

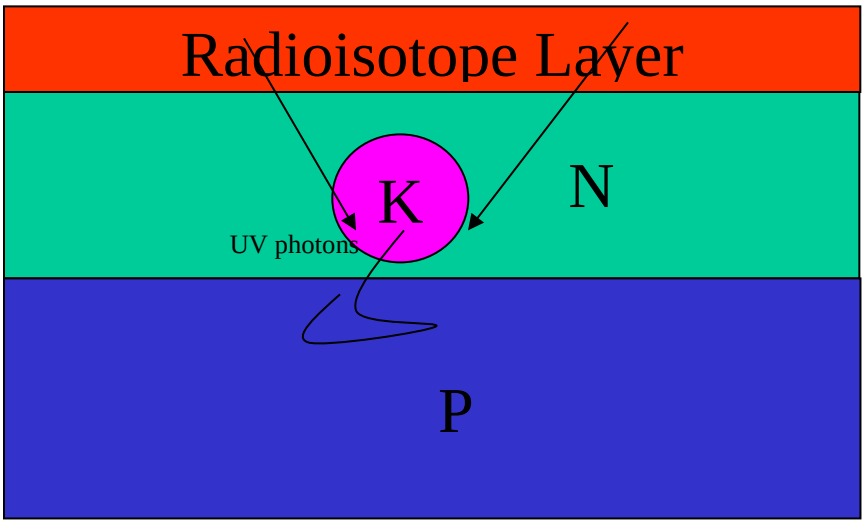

Figure 34. Option A: Micro bubble as a radiation shield as well as a way of converting the kinetic energy of radiation into narrow band UV photons that are absorbed by the p-n junction.

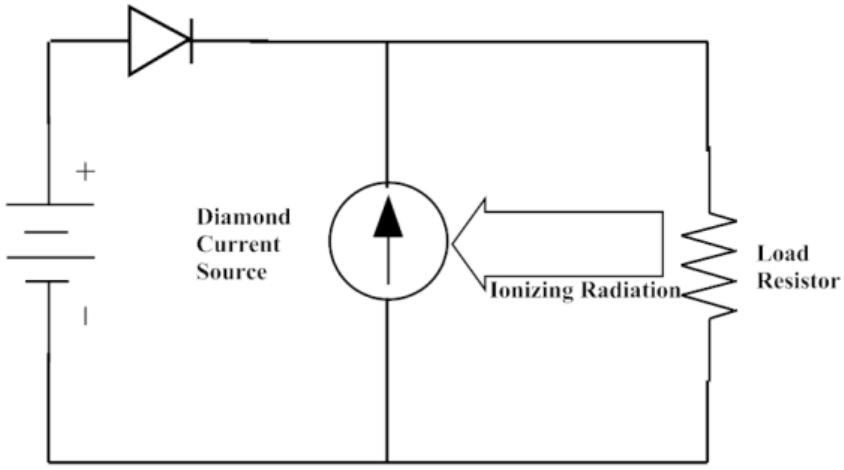

Figure 35. Basic diagram of an electronic grade substrate being bombarded with ionizing radiation and being used a current source to provide power to a load.

Figure 36. PSpice model output which shows that the drain on the battery is 1.01×10^{-16} W while the flow to the load resistor (R3) is 1.002 microwatts.

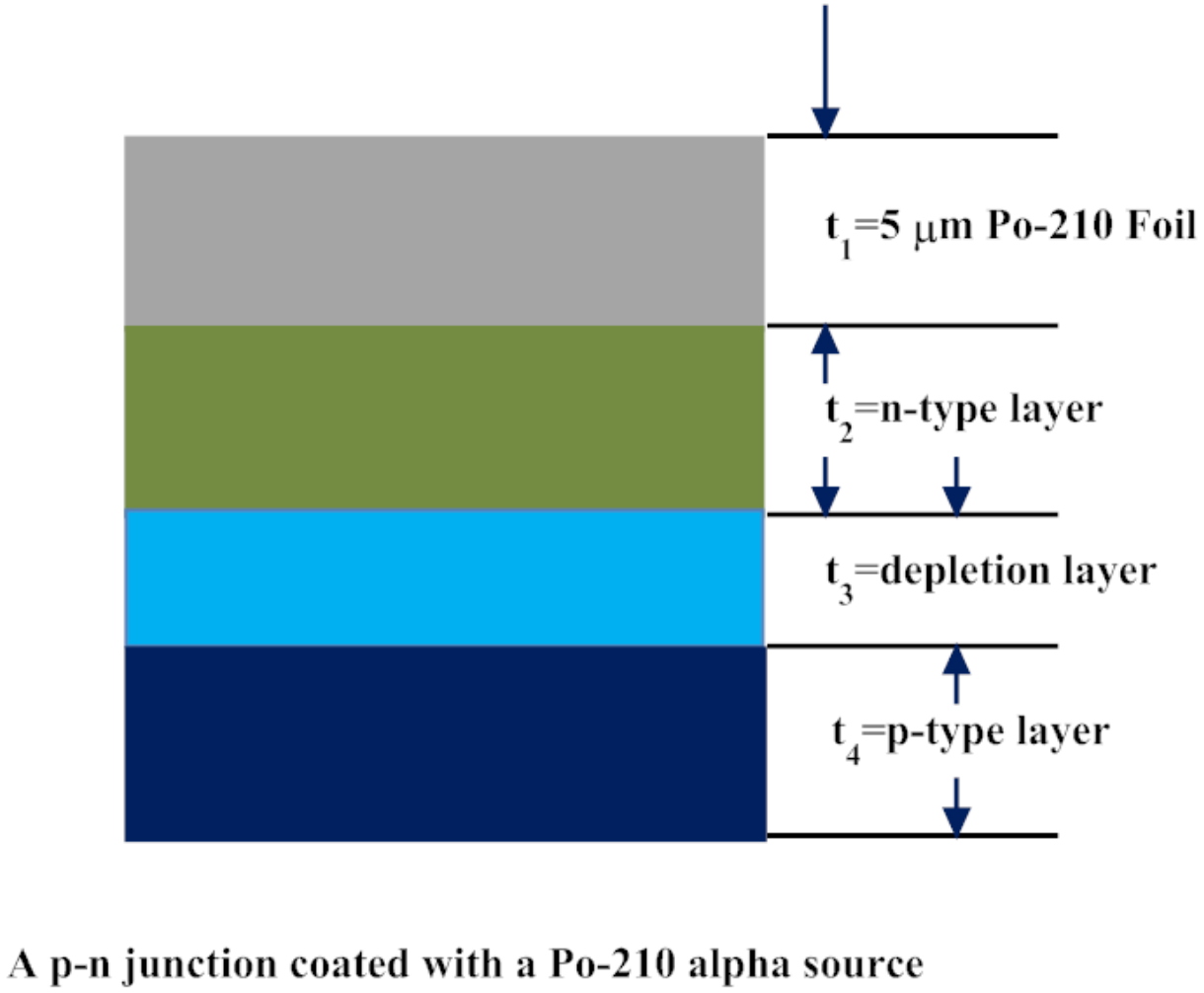

Figure 37. Layout of a typical p-n junction based alphavoltaic using a polonium 210 foil made of 10% polonium and 90% silver placed on a silicon carbide p-n junction.

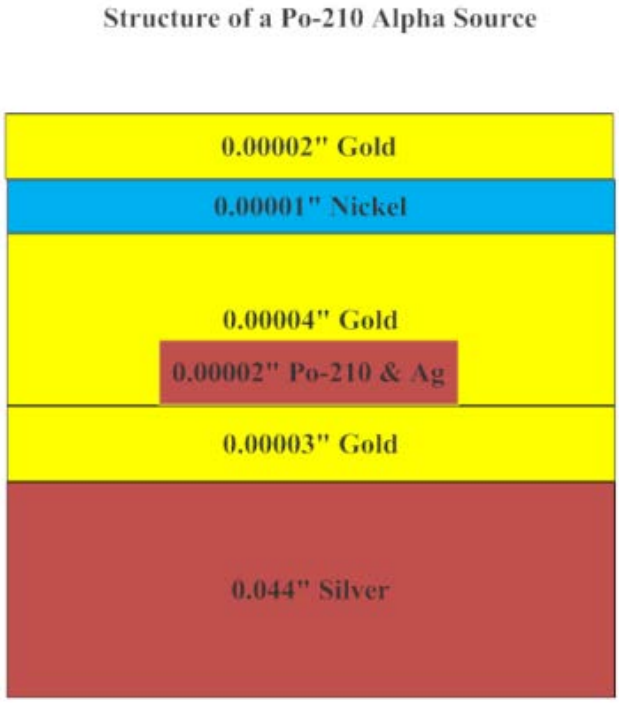

Figure 38. Typical design of a Po-210 alpha source. The polonium 210 foil is made of 10% polonium and 90% silver

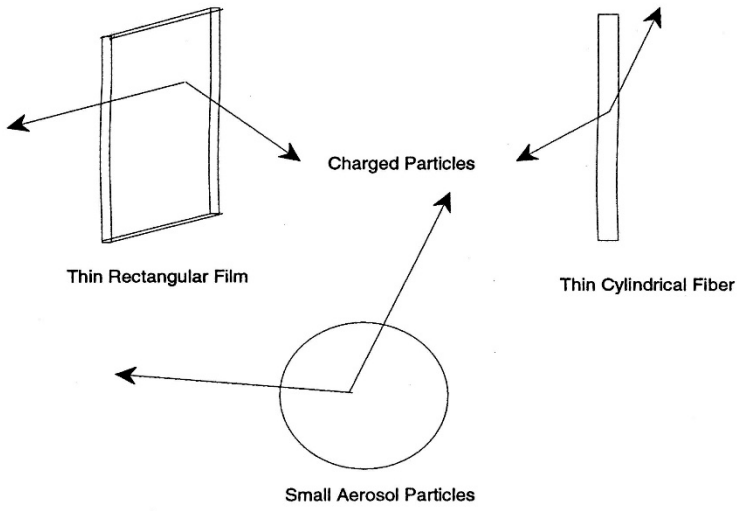

Figure 39. An illustration of the use of thin solid geometries which allow reaction products (indicated by arrows) to escape the solid matrix into a surrounding gas [84].

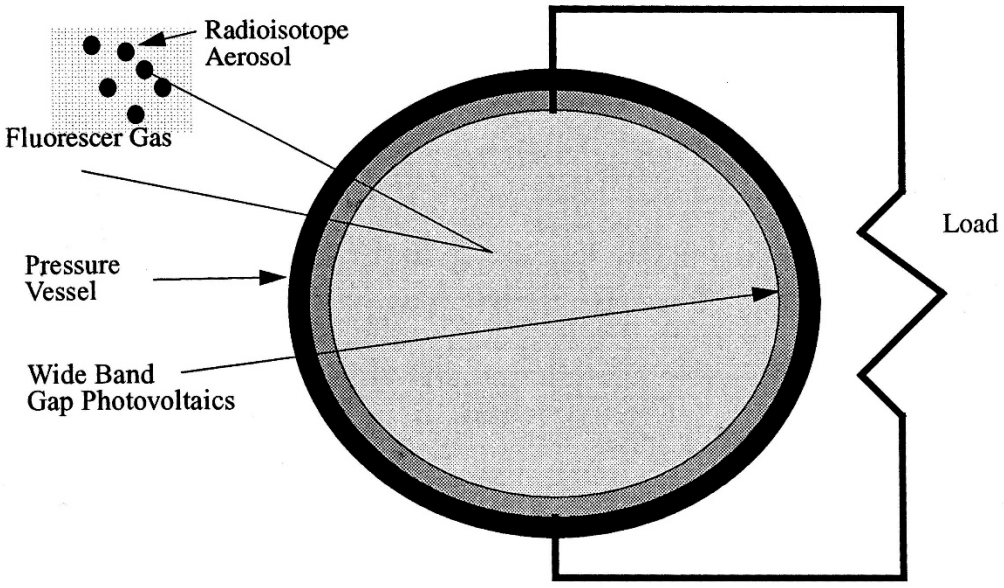

Figure 40. Schematic diagram of a PIDEC nuclear battery which uses a radioisotope fuel in aerosol form [84].

References

[1] H. G. J. Moseley and J. Harling, "The Attainment of High Potentials by the Use of Radium,," *Proc. R. Soc. (London) A,* vol. 88, p. 471, 1913.

[2] National_Research_Council_Radioisotope_Power_Systems_Committee, *Radioisotope Power Systems: An Imperative for Maintaining US Leadership in Space Exploration*: National Academies Press, 2009.

[3] F. Ritz and C. E. Peterson, "Multi-mission radioisotope thermoelectric generator (MMRTG) program overview," in *Aerospace Conference, 2004. Proceedings. 2004 IEEE*, 2004, p. 2957 Vol.5.

[4] B. C. Blanke, J. H. Birden, K. C. Jordan, and E. L. Murphy, "Nuclear Battery-Thermocouple Type Summary Report," U. S. A. E. Comission, Ed., 16 ed: U.S. Department of Commerce, 1962.

[5] G. R. Schmidt, T. J. Sutliff, and L. A. Dudzinski, "Radioisotope Power: A Key Technology for Deep Space Exploration," in *Radioisotopes - Applications in Physical Sciences*, P. N. Singh, Ed., ed: INTECH, 2011.

[6] M. A. Prelas and S. K. Loyalka, "A review of the utilization of energetic ions for the production of excited atomic and molecular states and chemical synthesis," *Progress in Nuclear Energy,* vol. 8, pp. 35-52, // 1981.

[7] G. N. Hatsopoulos and E. P. Gyftopoulos, *Thermionic Energy Conversion, Vol. 1: Processes and Devices*: The MIT Press, 1973.

[8] R. E. Nelson, " A brief history of thermophotovoltaic development," *Semiconductor Science and Technology,* vol. 18, pp. S141–S143, 2003.

[9] T. K. Hunt, N. Weber, and T. Cole, "High Efficiency Thermoelectric Conversion with Beta"-Alumina Electrolytes, The Sodium Heat Engine," *Solid State Ionics,* vol. 5, pp. 263-266, 1981.

[10] Department_of_Energy, "Summary of Plutonium-238 Production Alternatives Analysis Final Report," I. N. Laboratory, Ed., ed: DOE, 2013.

[11] S. Deus, "Tritium-powered betavoltaic cells based on amorphous silicon," in *Photovoltaic Specialists Conference, 2000. Conference Record of the Twenty-Eighth IEEE*, 2000, pp. 1246-1249.

[12] R. Duggirala, H. Li, and A. Lal, "High efficiency radioisotope energy conversion using reciprocating electromechanical converters with integrated betavoltaics," *Appl. Phys. Lett.,* vol. 92, 2008.

[13] M. A. Prelas, "Nuclear-Driven Solid-State Lasers," in *International Conference on Lasers '89*, New Orleans, LA, 1989.

[14] M. Prelas, E. Charlson, F. Boody, and G. Miley, "Advanced nuclear energy conversion using a two step photon intermediate technique," *Prog. In Nuclear Energy,* vol. 23, pp. 223-240, 1990.

[15] M. L. Watermann and M. A. Prelas, "Integrated Solid-State Nuclear Pumped Laser/Reactor Design for Asteroid Redirection," *Transactions of the American Nuclear Society,* November 2013 2013.

[16] A. Smith, P. Fields, and J. Roberts, "Spontaneous Fission Neutron Spectrum of Cf252," *Physical Review,* vol. 108, pp. 411-413, 1957.

[17] D. B. Nicodemus and H. H. Staub, "Fission Neutron Spectrum of U^{235}," *Physical Review,* vol. 89, pp. 1288-1290, 03/15/ 1953.

[18] S. Zeynalov, F.-J. Hambsch, and S. Obertstedt, "Neutron Emission in Fission of ^252Cf(SF)," *Journal of the Korean Physical Society,* vol. 59, p. 1396, 2011.

[19] DOE-HDBK-1019/1-93, "Nuclear Physics and Reactor Theory," *Washington DC: Department of Energy,* 1993.

[20] J. E. Turner and C. A. Kelsey, *Atoms, radiation, and radiation protection*: Wiley New York, 1995.

[21] J. F. Ziegler, M. D. Ziegler, and J. P. Biersack, "SRIM–The stopping and range of ions in matter (2010)," *Nuclear Instruments and Methods in Physics Research Section B: Beam Interactions with Materials and Atoms,* vol. 268, pp. 1818-1823, 2010.

[22] K. Oh, M. A. Prelas, J. B. Rothenberger, E. D. Lukosi, J. Jeong, D. E. Montenegro*, et al.*, "Theoretical Maximum Efficiencies of Optimized Slab and Spherical Betavoltaic Systems Utilizing Sulfur-35, Strontium-90, and Yttrium-90," *Nuclear Technology,* vol. 179, p. 9, 2012.

[23] J. Guyot, G. Miley, and J. Verdeyen, "Application of a two-region heavy charged particle model to Noble-gas plasmas induced by nuclear radiations," *Nucl. Sci. Eng,* vol. 48, pp. 373-386, 1972.

[24] J. L. Giuliani, G. M. Petrov, and A. Dasgupta, "Electron energy deposition in an electron-beam pumped KrF amplifier: Impact of the gas composition," *Journal of Applied Physics,* vol. 92, pp. 1200-1206, 2002.

[25] S. Bernard, A. Slaback Jr Lester, and B. B. Kent, "Handbook of Health Physics and Radiological Health," ed: Baltimore: Williams & Wilkins, 1998.

[26] K. Oh, "Modeling and maximum theoretical efficiencies of linearly graded alphavoltaic and betavoltaltaic cells," M.Sc., Nuclear Science & Engineering Institute, University of Missouri, University of Missouri -- Columbia, 2011.

[27] Y. Musienko, S. Reucroft, D. Ruuska, and J. Swain, "Studies of neutron irradiation of avalanche photodiodes using< sup> 252</sup> Cf," *Nuclear Instruments and Methods in Physics Research Section A: Accelerators, Spectrometers, Detectors and Associated Equipment,* vol. 447, pp. 437-458, 2000.

[28] T. E. Johnson and B. K. Birky, *Health physics and radiological health*: Lippincott Williams & Wilkins, 2012.

[29] W. P. Jesse, "Absolute Energy to Produce an Ion Pair in Various Gases by Beta Particles from ^{35}S," *Physical Review,* vol. 109, pp. 2002-2004, 03/15/ 1958.

[30] G. Friedlander, *Nuclear and radiochemistry*. New York, N.Y. [etc.]: Wiley, 1981.

[31] M. A. Prelas, F. P. Boody, G. H. Miley, and J. F. Kunze, "Nuclear driven flashlamps," *Laser and Particle Beams,* vol. 6, pp. 25-62, 1988.

[32] G. Friedländer and J. W. Kennedy, *Nuclear and Radiochemistry*: John Wiley, 1955.

[33] J. D. Wrbanek, S. Y. Wrbanek, G. C. Fralick, and L.-Y. Chen, "Micro-fabricated solid-state radiation detectors for active personal dosimetry," *NASA/TM,* vol. 214674, 2007.

[34] A. K. Chung and M. A. Perelas, "The transport of heavy charged particles in a cylindrical nuclear-pumped plasma," *Journal Name: Nucl. Sci. Eng.; (United States); Journal Volume: 86:3,* pp. Medium: X; Size: Pages: 267-274, 1984.

[35] J. Ahlswede, S. Hebel, M. B. Kalinowski, and J. O. Roß, *Update of the global krypton-85 emission inventory*: Carl-Friedrich-von-Weizsäcker-Zentrum für Naturwissenschaft und Friedensforschung der Universität Hamburg, 2009.

[36] Department_of_Energy, "Draft EIS for the Proposed Consolidation of Nuclear Operations Related to Production of Radioisotope Power Systems," S. a. T. Office of Nuclear Energy, Ed., ed. Washington DC: DOE, 2005.

[37] O. Lastres, D. Chandler, J. J. Jarrell, and G. I. Maldonado, "Studies of Plutonium-238 Production at the High Flux Isotope Reactor," *Transactions of the American Nuclear Society,* vol. 104, pp. 716-718, 2011.

[38] D. Albright and K. Kramer, "Neptunium 237 and Americium: World Inventories and Proliferation Concerns," in *ISIS Document Collection*, I. f. S. a. I. Security, Ed., ed. ISIS, 2005.

[39] M. Prelas, J. Romero, and E. Pearson, "A Critical REview of Fusion Systems for Radiolytic Conversion of Inorganics to Gaseous Fuels," *Nuclear Technology Fusion,* vol. 2, p. 143, 1982.

[40] P. Rappaport, "Radioactive Battery Employing Intrinsic Semiconductor," USA Patent 2,745,973, 1956.

[41] J. N. Anno, "A Direct-Energy Conversion Device Using Alpha Particles," *Nuclear News,* vol. 6, 1962.

[42] K. Oh, M. A. Prelas, E. D. Lukosi, J. B. Rothenberger, R. J. Schott, C. L. Weaver*, et al.*, "The Theoretical Maximum Efficiency for a Linearly Graded Alphavoltaic Nuclear Battery," *Nuclear Technology,* vol. 179, p. 7, August 2012.

[43] R. J. Schott, "Photon intermediate direct energy conversion using a Sr-90 beta source," PhD, Nuclear Science and Engineering Institute, University of Missouri, 2012.

[44] G. Popovici, A. Melnikov, V. V. Varichenko, T. Sung, M. A. Prelas, R. G. Wilson*, et al.*, "Diamond ultraviolet photovoltaic cell obtained by lithium and boron doping," *Journal of Applied Physics,* vol. 81, p. 2429, 1997.

[45] W. A. Doolittle, A. Rohatgi, R. Ahrenkiel, D. Levi, G. Augustine, and R. H. Hopkins, "Understanding The Role Of Defects In Limiting The Minority Carrier Lifetime In Sic," *MRS Online Proceedings Library,* vol. 483, pp. null-null, 1997.

[46] J. F. Seely, B. Kjornrattanawanich, G. E. Holland, and R. Korde, "Response of a SiC photodiode to extreme ultraviolet through visible radiation," *Optics Letters,* vol. 30, pp. 3120-3122, 2005/12/01 2005.

[47] D. A. Neamen, *Semiconductor physics and devices*: McGraw Hill, 2003.

[48] A. Savtchouk, E. Oborina, A. Hoff, and J. Lagowski, "Non-contact doping profiling in epitaxial SiC," in *Materials Science Forum*, 2004, pp. 755-758.

[49] M. Huang, N. Goldsman, C.-H. Chang, I. Mayergoyz, J. M. McGarrity, and D. Woolard, "Determining 4H silicon carbide electronic properties through combined use of device simulation and metal--semiconductor field-effect-transistor terminal characteristics," *Journal of Applied Physics,* vol. 84, pp. 2065-2070, 08/15/ 1998.

[50] E. Steinfelds and J. Tulenko, "Isotopes and Radiation: General-Evaluation and Verification of Durability and Efficiency of Components of Photon Assisted Radioisotopic Batteries," *Transactions of the American Nuclear Society,* vol. 104, p. 201, 2011.

[51] E. V. Steinfelds and J. S. Tulenko, "Development and Testing of a Nanotech Nuclear Battery for Powering MEMS Devices," *Nuclear Technology,* vol. 174, pp. 119-123, 2011.

[52] E. Steinfelds and J. S. Tulenko, "Designs and Performance Assessments of Photon Assisted Radioisotopic Energy Sources," *Transactions of the American Nuclear Society,* vol. 100, pp. 672-674, 2009.

[53] E. Steinfelds and M. Prelas, "More sources and review of design for radioisotope energy conversion systems," *Transactions of the American Nuclear Society,* vol. 96, pp. 811-812, 2007.

[54] K. E. Bower, Y. A. Barbanel, Y. G. Shreter, and G. W. Bohnert, *Polymers, Phosphors, and Voltaics for Radioisotope Microbatteries*: CRC Press, 2002.

[55] M. A. Prelas, J. Sved, A. Dann, H. J. Jennings, and A. Mountford, "Solid state electric generator using radionuclide-induced exciton production, WO 1999036967 A1," 1999.

[56] W. Shan, J. W. A. III, K. M. Yu, W. Walukiewicz, E. E. Haller, M. C. Martin*, et al.*, "Dependence of the fundamental band gap of $Al_xGa_{1-x}N$ on alloy composition and pressure," *Journal Of Applied Physics,* vol. 85, pp. 8505-8507, 1999.

[57] M. A. Prelas, "Micro-scale power source, United States Patent 8552616," USA Patent, 2013.

[58] F. Y.-H. Tsang, T. D. Juergens, Y. D. Harker, K. S. Kwok, N. Newman, and S. A. Ploger, "Nuclear voltaic cell," ed: Google Patents, 2012.

[59] T. Wacharasindhu, K. Jae Wan, D. E. Meier, and J. D. Robertson, "Liquid-semiconductor-based micro power source using radioisotope energy conversion," in *Solid-State Sensors, Actuators and Microsystems Conference, 2009. TRANSDUCERS 2009. International*, 2009, pp. 656-659.

[60] J. U. Patel, J.-P. Fleurial, and G. J. Snyder, "Alpha-Voltaic Sources Using Liquid Ga as Conversion Medium," ed. NASA: NASA Tech Briefs, 2006.

[61] S. M. Sze and K. K. Ng, *Physics of Semiconductor Devices*: Wiley, 2006.

[62] A. Latreche and Z. Ouennoughi, "Modified Airy function method modelling of tunnelling current for Schottky barrier diodes on silicon carbide," *Semiconductor Science and Technology,* vol. 28, p. 105003, 2013.

[63] L. Östlund, "Fabrication and Characterization of Micro and Nano Scale SiC UV Photodetectors," in *Student Thesis, Masters of Science*, Royal_Institute_of_Technology, Ed., ed. Stockholm, 2011, p. 74.

[64] C. J. Eiting, V. Krishnamoorthy, S. Rodgers, T. George, J. D. Robertson, and J. Brockman, "Demonstration of a radiation resistant, high efficiency SiC betavoltaic," *Applied Physics Letters,* vol. 88, pp. 064101-064101-3, 2006.

[65] M. Prelas and E. Charlson, "Synergism in inertial confinement fusion: a total direct energy conversion package," *Lasers and Particle Beams,* vol. 7, pp. 449-466, 1989.

[66] R. J. Schott, C. L. Weaver, M. A. Prelas, K. Oh, J. B. Rothenberger, R. V. Tompson*, et al.*, "Photon Intermediate Direct Energy Conversion Using a 90Sr Beta Source," *Nuclear Technology,* vol. 181, p. 5, February 2013.

[67] C. L. Weaver, "PIDECα: photon intermediate direct energy conversion using the alpha emitter polonium-210," Ph.D. Ph.D., Nuclear Science and Engineering Institute, University of Missouri, http://hdl.handle.net/10355/15908, 2012.

[68] A. Syed, "Modeling the Energy Deposition of Alpha Particles Emitted from Po-210 source on Silicon Carbide for possible Nuclear Battery and Laser Pump Applications," M.Sc., Nuclear Science & Engineering Institute, University of Missouri -- Columbia, Columbia, MO, 2012.

[69] P. Ashburn and D. V. Morgan, "The role of radiation damage on the current-voltage characteristics of pn junctions," *Solid-State Electronics,* vol. 17, pp. 689-698, 1974.

[70] G. Rybicki, C. Vargas-Aburto, and R. Uribe, "Silicon carbide alphavoltaic battery," 1996, pp. 93-96.

[71] V. Andreev, A. Kevetsky, V. Kaiinovsky, V. Khvostikov, V. Larionov, V. Rumyantsev*, et al.*, "Tritium-powered betacells based on $Al_xGa_{1-x}As$," in *Photovoltaic Specialists Conference, 2000. Conference Record of the Twenty-Eighth IEEE*, 2000, pp. 1253-1256.

[72] M. Lu, G.-g. Zhang, K. Fu, G.-h. Yu, D. Su, and J.-f. Hu, "Gallium Nitride Schottky betavoltaic nuclear batteries," *Energy Conversion and Management,* vol. 52, pp. 1955-1958, 4// 2011.

[73] H. Flicker, J. Loferski, and T. Elleman, "Construction of a promethium-147 atomic battery," *Electron Devices, IEEE Transactions on,* vol. 11, pp. 2-8, 1964.

[74] X.-Y. Li, Y. Ren, X.-J. Chen, D.-Y. Qiao, and W.-Z. Yuan, "63Ni schottky barrier nuclear battery of 4H-SiC," *Journal of Radioanalytical and Nuclear Chemistry,* vol. 287, pp. 173-176, 2011.

[75] J. Clarkson, W. Sun, K. Hirschman, L. Gadeken, and P. Fauchet, "Betavoltaic and photovoltaic energy conversion in three-dimensional macroporous silicon diodes," *Physica status solidi (a),* vol. 204, pp. 1536-1540, 2007.

[76] C. Zaijun, S. Haisheng, L. Yanfei, and C. Xuyuan, "The design optimization for GaN-based betavoltaic microbattery," in *Nano/Micro Engineered and Molecular Systems (NEMS), 2010 5th IEEE International Conference on*, 2010, pp. 582-586.

[77] Z. Cheng, H. San, Y. Li, and X. Chen, "The design optimization for GaN-based betavoltaic microbattery," in *Nano/Micro Engineered and Molecular Systems (NEMS), 2010 5th IEEE International Conference on*, 2010, pp. 582-586.

[78] G. Hang and A. Lal, "Nanopower betavoltaic microbatteries," in *Transducers, Solid-State Sensors, Actuators and Microsystems, 12th International Conference on, 2003*, 2003, pp. 36-39 vol.1.

[79] C. D. Cress, B. Landi, R. P. Raffaelle, and D. M. Wilt, "InGaP alpha voltaic batteries: Synthesis, modeling, and radiation tolerance," *Journal of Applied Physics,* vol. 100, pp. 114519-114519-5, 2006.

[80] A. Kavetskiy, G. Yakubova, S. M. Yousaf, K. Bower, J. D. Robertson, and A. Garnov, "Efficiency of Pm-147 direct charge radioisotope battery," *Applied Radiation and Isotopes,* vol. 69, pp. 744-748, 2011.

[81] A. K. Galina Yakubova, *Nuclear Batteries with Tritium and Promethium-147 Radioactive Sources: Design, Efficiency, Application of Tritium and Pm-147 Direct Charge Batteries, Tritium Battery with Solid Dielectric*: LAP Lambert Academic Publishing 2012.

[82] M. Sychov, A. Kavetsky, G. Yakubova, G. Walter, S. Yousaf, Q. Lin*, et al.*, "Alpha indirect conversion radioisotope power source," *Applied Radiation and Isotopes,* vol. 66, pp. 173-177, 2// 2008.

[83] D. Y. Qiao, X. J. Chen, Y. Ren, and W. Z. Yuan, "A micro nuclear battery based on Sic schottky barrier diode," *Journal of Microelectromechanical Systems,* vol. 20, pp. 685-690, // 2011.

[84] M. Prelas, G. Popovici, S. Khasawinah, and J. Sung, "Wide band-gap photovoltaics," in *Wide Band Gap Electronic Materials*, ed: Springer, 1995, pp. 463-474.

[85] M. Prelas, E. Charlson, E. Charlson, J. Meese, G. Popovici, and T. Stacy, "Diamond Photovoltaic Energy Conversion," *Second International Conference on the Application of Diamond Films and*

Related Materials, Editors M. Yoshikawa, M. Murakawa, Y. Tzeng and WA Yarbrough, MY Tokyo, pp. 5-12, 1993.

[86] M. Wolverton, "Stirling in Deep Space," *Scientific American,* vol. 298, p. 22, 2008.

[87] G. H. Miley, *Direct conversion of nuclear radiation energy*: American Nuclear Society, 1970.

[88] G. Miley, "Fusion Energy Conversion," ed: American Nuclear Society, 1976.